

# **Design, Analysis, and Evaluation of a Novel Propulsive Wing Concept**

**LEARN Phase I**

**Final Report**

**Contract Number NNX15AE39A**

**June 30th, 2016**

**Brian Kramer  
Rolling Hills Research Corporation**

**Phillip Ansell, Steve D'Urso, Gavin Ananda, Aaron Perry  
The University of Illinois at Urbana-Champaign**

*Contracting Officer's Technical Representative:*

**Hyun Dae Kim  
NASA Armstrong Research Center  
PO Box 273  
Edwards, CA 93523-0273**

**ROLLING HILLS RESEARCH CORPORATION**

**420 N. Nash Street, El Segundo, CA 90245-2822  
(310) 640-8781 [aero@RollingHillsResearch.com](mailto:aero@RollingHillsResearch.com)**

## Table of Contents

<b>1</b>	<b>INTRODUCTION.....</b>	<b>3</b>
1.1	BACKGROUND AND PROGRAM OBJECTIVES .....	3
1.1.1	<i>State-of-the-Art in Efficient Aircraft Concepts</i> .....	3
1.2	IDENTIFICATION AND SIGNIFICANCE OF INNOVATION .....	4
1.2.1	<i>Technical Background of Griffith/Goldschmied Airfoil Concept</i> .....	4
1.2.2	<i>Propulsive Wing Concept</i> .....	5
1.3	SUMMARY OF CONCEPT AND GOALS .....	6
<b>2</b>	<b>KICK-OFF BRIEFING.....</b>	<b>6</b>
<b>3</b>	<b>TRANSONIC GRIFFITH/GOLDSCHMIED SECTION DEVELOPMENT ....</b>	<b>7</b>
3.1	AIRFOIL DESIGN CONDITIONS.....	8
3.2	GOLDSCHMIED SPANLOADER ANALYSIS.....	8
3.3	OPTIMIZATION SET-UP .....	15
3.4	AIRFOIL PARAMETRIC REPRESENTATION.....	16
3.5	INITIAL OPTIMIZER RESULTS .....	17
3.6	PARAMETRIC INVESTIGATIONS .....	25
3.7	INVERSE AIRFOIL DESIGN APPROACH.....	29
3.8	SYMMETRIC AIRFOIL STUDY TO UNDERSTAND CONTRIBUTIONS TO PRESSURE THRUST.....	31
3.9	FINAL AIRFOIL DESIGN.....	37
<b>4</b>	<b>LOW-SPEED WIND TUNNEL VALIDATION OF AIRFOIL DESIGN.....</b>	<b>41</b>
4.1	WIND TUNNEL MODEL DESIGN .....	41
4.2	WIND TUNNEL TEST APPROACH .....	45
4.3	EXPERIMENTAL RESULTS.....	47
<b>5</b>	<b>EXPERIMENTAL CROSS-FLOW FAN TESTING AND DEVELOPMENT</b>	<b>51</b>
5.1	CFF EXPERIMENTAL SETUP.....	51
5.2	CFF TEST RESULTS .....	55
5.2.1	<i>Expansion surface pressure measurements</i> .....	55
5.2.2	<i>Duct surveys</i> .....	56
5.2.3	<i>Fan power measurements</i> .....	60
<b>6</b>	<b>SYSTEMS AND ENERGY BALANCE.....</b>	<b>64</b>
6.1	AIRCRAFT BASELINE MATCHING .....	64
6.1.1	<i>Geometry</i> .....	65
6.1.2	<i>Mission Trajectory</i> .....	66
6.1.3	<i>Aerodynamics</i> .....	66
6.1.4	<i>Propulsion</i> .....	69
6.1.5	<i>Weights</i> .....	69
6.1.6	<i>Matching Results</i> .....	71
6.1	TRADE STUDIES / SENSITIVITY ANALYSIS.....	72
6.2	WING STRUCTURAL MODELING.....	74

6.3	ENERGY BALANCE SUMMARY .....	75
7	PHASE I SUMMARY .....	75
8	REFERENCES.....	76

## 1 **Introduction**

### 1.1 **Background and Program Objectives**

In order to meet future goals for aircraft efficiency and performance, the next generation of aircraft will have to employ new technologies in aerodynamics, propulsion, and structures. The NASA Subsonic Fixed Wing (SFW) project has identified ambitious goals for the next three generations of aircraft, N+1, N+2, and N+3. For the N+3 generation (2025 timeframe), these include a -52 dB noise reduction relative to a stage 4 noise limit, a -80% reduction in NOx emissions, and a -60% reduction in total mission energy consumption.<sup>1</sup> For a current, state-of-the-art Boeing 777-200LR baseline, this represents a -70% reduction in fuel burn.<sup>2</sup> In order to achieve these large reductions, exploration into new, radical and revolutionary aircraft configurations and propulsion technologies will be required. The need for more efficient, sustainable, and environmentally responsible aircraft is at the heart of the SFW project. The forecasted growth in air travel within the United States by over 90% across the next two decades,<sup>3</sup> coupled with the long-term, continued rise in fuel-based operating costs for airlines<sup>4</sup> make the goals of the SFW project more than simply altruistic, they are goals the aviation industry need to achieve to remain profitable in an increasingly stringent and regulated environment.

#### 1.1.1 **State-of-the-Art in Efficient Aircraft Concepts**

Several recent studies into alternative aircraft configurations and propulsion technologies have shown significant promise. These include the Hybrid Blended Wing Body (HBWB) and MIT's double bubble D8. The HBWB uses a high-efficiency flying wing planform to provide a high cruise L/D and upper surface mounted engines to provide noise shielding. With pylon mounted ultra-high bypass ratio (UHB) engines, the HBWB provides a predicted 52% fuel burn reduction.<sup>2</sup> The fuel burn can be further reduced by replacing the pylon mounted UHB engines with a turbo-electric distributed propulsion system (TeDP) employing boundary-layer ingestion (BLI) for improved engine performance and wake filling. The revolutionary TeDP propulsion concept uses electric motor driven fans to provide propulsive thrust, with gas turbine generators providing electric power for the system. Such a concept provides flexibility in engine placement for propulsion airframe integration and introduces capabilities for spanwise distribution of thrust that are not feasible with conventional podded engines.

MIT's double bubble D8 configuration uses a wider, double tube, lifting fuselage, allowing a smaller wing to be used. The D8 also uses embedded, rear mounted upper surface engines and boundary-layer ingestion, and it also promises efficiencies similar to the HBWB.<sup>5,6</sup> Both BLI systems and axial power plants, however, must overcome inlet

distortion issues as a result of ingesting the boundary-layer. Figure 1 shows a representation of the HBWB and D8 concepts. Both concepts show a high degree of synergistic aero/propulsion integration.

Outboard of the fuselage or main body of the aircraft, both configurations utilize a conventional wing surface. It is believed that further increases in efficiency can be achieved by combining the respective configuration's merits with an advanced concept airfoil section on the main wing. The proposed study seeks to develop an advanced propulsive wing concept by introducing a transonic Griffith/Goldschmied airfoil as a method for introducing large, realizable runs of laminar flow on the wing surfaces, coupled with a significantly reduced pressure drag, with the additional benefit of wake filling. This synergistic laminar flow, pressure thrust, wake filled section can be applied to a wide array of conventional and concept aircraft configurations, including the HBWB or D8, allowing the performance and efficiency improvements of the airfoil concept to be realized across a wide array of aircraft.

HBWB<sup>7</sup>D8 Double Bubble<sup>8</sup>

*Figure 1: Advanced concept configurations designed to meet SFW N+3 performance goals.*

## 1.2 Identification and Significance of Innovation

### 1.2.1 Technical Background of Griffith/Goldschmied Airfoil Concept

The basic Griffith airfoil concept, originally developed in the 1940's, utilizes a thick ( $t/c \geq 30\%$ ) airfoil section, where the boundary layer experiences a very favorable pressure gradient across the entire chord of the airfoil, except near the trailing-edge. This very favorable pressure gradient dampens the instabilities leading to transition, producing long runs of laminar flow.<sup>9,10</sup> In a modern application, the magnitude of the favorable gradient can be tailored so as to provide laminar flow at higher, flight Reynolds numbers for a transport-class aircraft.<sup>11</sup> For the original Griffith concept, pressure recovery at the trailing-edge is associated with a discontinuous increase in pressure. A suction slot is used at the location of this sudden pressure rise to maintain boundary-layer attachment and laminar flow. An example of the airfoil profile and inviscid velocity profile behind the development of the Griffith airfoil is presented in Figure 2, after Richards et al.<sup>12</sup>

Subsequent development of this concept was performed by Fabio Goldschmied, who employed the concept on airship development, and also proposed it for a thick-wing

general aviation aircraft.<sup>13-15</sup> Results of wind-tunnel testing on the Goldschmied airship identified unprecedented increases in aerodynamic efficiency of the vehicle design, resulting in a total power reduction on the order of 40%-50% when compared to other designs of the time.

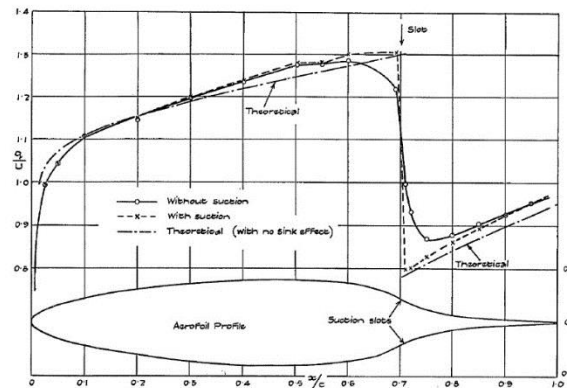


Figure 2: Symmetric Griffith airfoil profile with inviscid and experimental velocity distribution, after Richards et al.<sup>12</sup>

### 1.2.2 Propulsive Wing Concept

While the potential benefits of using a combined Griffith/Goldschmied airfoil concept in wing design are clear, there are several significant challenges that have prevented it from being actively utilized. Thus far, the Griffith/Goldschmied airfoil concept has only been applied to thick airfoils, giving it a low critical Mach number. For example, the Goldschmied thick-wing spanloader concept had a critical Mach number of 0.45.<sup>15</sup> If the concept were to be used on a modern, transport class configuration, it would have to have a critical Mach number characteristic of a conventional transonic airfoil design. The other significant challenge associated with the Griffith/Goldschmied airfoil concept is the choice of an efficient method to provide suction to the airfoil sections. In Goldschmied's original thick-wing spanloader concept,<sup>15</sup> propulsion was to be provided using podded engines. A much more synergistic approach is envisioned for the current application with an embedded suction system ejecting through the airfoil trailing-edge.

For the proposed propulsion airframe integration scheme, the cross-flow fan has several advantages over traditional axial fan configurations. Since cross-flow fans are more effective at handling high back pressure than axial fans, they are more suitable for providing propulsion-driven suction through ducts, slots, and pores. Electric cross-flow fans are also capable of achieving adiabatic compression efficiencies on the order of 80%.<sup>16</sup> Additionally, while the effects of inlet distortion on the efficiency of cross-flow fans has not been evaluated experimentally, high-fidelity simulations of Kummer and Dang<sup>17</sup> suggest that cross-flow fans are effectively insensitive to inlet distortion.<sup>18</sup> A schematic of the proposed transonic Griffith/Goldschmied airfoil is shown in Figure 3.

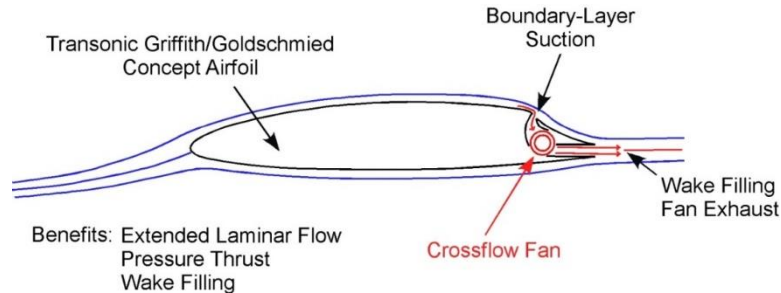


Figure 3: Proposed transonic Griffith/Goldschmied airfoil concept.

### 1.3 Summary of Concept and Goals

The Phase I study developed a propulsive wing concept by designing a set of transonic laminar flow Griffith/Goldschmied airfoils, while also exploring possibilities of developing static pressure thrust. Cross-flow fans were integrated into this airfoil design, which will supply the necessary boundary-layer suction for the proposed airfoil concept. Exhaust from the cross-flow fan based suction system was then routed out the airfoil trailing-edge, providing additional thrust for sectional wake filling. Since these fans are typically electrically powered, it is beneficial to also incorporate them into a hybrid-electric aircraft architecture.

The ultimate goal of the Phase I study was to develop a propulsive, transonic airfoil section using a suction-driven pressure recovery, similar to the design philosophy of a Griffith/Goldschmied section. The resulting airfoil was designed to provide extended runs of natural laminar flow, static pressure thrust, and a wake filling effect for a design Mach of 0.70. A series of experiments were conducted on cross-flow fans in transonic flow conditions in order to evaluate their suitability for the suction system requirements of this concept. Finally, a systems and energy balance was performed to determine if the drag savings produced by the airfoil section were large enough to overcome the electrical costs to power the suction system. The final airfoil design was then tested in a low-speed wind tunnel to verify the discrete pressure increase through suction and static pressure thrust produced by the design.

A Phase II study was proposed that would have taken the next logical step and validate the Griffith/Goldschmied airfoil concept in a large-scale transonic wind tunnel. The proposed plan was to design a new airfoil section for a design  $M = 0.8$ , and test it in the NASA Ames 12-Foot Transonic Unitary Wind Tunnel. However, this Phase II study was not funded and no immediate developments in the development of the transonic Griffith/Goldschmied airfoil concept are anticipated.

## 2 Kick-Off Briefing

In order to establish an understanding of the goals, objectives, and direction for the Phase I study, personnel from Rolling Hills Research Corporation and the University of Illinois visited NASA Armstrong for a kickoff meeting on March 23rd, 2015. Holding this



meeting ensured that the research goals of RHRC, Illinois, and NASA could be pursued synergistically throughout the Phase I effort. During this meeting, the concept background and overall approach towards the development of the new concept were discussed. The need for a detailed systems and energy balance of the concept and its implementation and the proposed cross-flow fan testing were also discussed. Finally, the choice of a baseline configuration for comparison of the new section for the systems and energy balance was also deliberated.

In order to perform an accurate assessment of the benefits produced with the implementation of the new proposed transonic Griffith/Goldschmied section, a baseline aircraft configuration to compare against was chosen. It was decided that the baseline configuration should be based on advanced technology so as not to provide an overly-optimistic assessment of the new section benefits. Also, since Griffith/Goldschmied sections are traditionally very thick sections ( $t/c \approx 0.30$ ), the Phase I effort was limited to a design Mach number of 0.70, with Phase II exploring higher traditional cruise Mach numbers for commercial transport-class aircraft. Other studies have identified a reduced Mach number of 0.70 as an advantageous cruise Mach for increased efficiency.

After discussion with NASA personnel, the aircraft configurations produced by Boeing as a part of the Subsonic Ultra Green Aircraft Research (SUGAR)<sup>19</sup> were identified as providing a series of advanced-concept aircraft configurations within the application and design space of the new Griffith/Goldschmied section. Additionally, several reports on the configurations are publicly available, which provide some level of detail for the configurations development and performance<sup>20</sup>. The SUGAR series of configurations are a 737 type single-aisle class of aircraft. As a result, the Boeing “SUGAR Refined” configuration was chosen as the baseline configuration for comparison.

### **3 Transonic Griffith/Goldschmied Section Development**

During the Phase I study, several key challenges were identified towards developing a transonic Griffith/Goldschmied airfoil concept. In previous work, the Griffith/Goldschmied airfoil concept had only been applied to thick airfoils, giving it a low critical Mach number. For example, the Goldschmied spanloader concept airfoil had a thickness of 31.5% and a critical Mach number of 0.45.<sup>15</sup> In order for a new section to be viable for a commercial transport, it must operate at a Mach number of at least 0.70. In order to reduce the critical Mach number of the newly-designed airfoil, the  $t/c$  of the section must be reduced to thickness ratios more characteristic of transonic airfoils, which typically have thickness ratios within the range from 9% to 12%. One of the key questions to be answered during the Phase I investigation: is can a section be designed with a thickness ratio of 15% or less to achieve a reasonable critical Mach number, yet still be able to employ the Griffith/Goldschmied suction concept for pressure drag reduction or elimination? Additionally, can the section pressure distribution be contoured to achieve long runs of natural laminar flow on both the upper and lower surface?

The section was designed to achieve three major goals, which include extended natural laminar flow, a suction-based trailing-edge recovery region designed to produce static pressure thrust, and wake filling resulting from the routing of the suction based mass flow through a trailing-edge ejector system. The section was designed using high fidelity, state-of-the-art CFD simulations. The OVERFLOW CFD program was used for the analysis of the new section. OVERFLOW<sup>21</sup> is a NASA developed Reynolds averaged Navier-Stokes fluid dynamic simulation program for structured grid systems. OVERFLOW can use single block grids or Chimera overset (structured) grid systems, allowing accurate assessment of complex aerodynamic geometries. OVERFLOW has been used extensively in the design and analysis of transonic airfoils and wings. OVERFLOW also contains an implementation of the Langtry-Menter  $\gamma$ - $Re_\theta$  transition prediction model.<sup>22,23</sup> The Langtry-Menter model is based on two transport equations, one for intermittency and one for a transition onset criterion in terms of momentum thickness Reynolds number. While the model is unable to predict swept wing crossflow based transition, it worked very well for the Phase I 2D study.

Since the performance of the new design is a very closely coupled system between the airfoil contour and the suction recovery, an attempted use of multidisciplinary optimization (MDO) was conducted during the design process to help guide the effort. The MDO program chosen for use during the program was OpenMDAO<sup>24</sup>. OpenMDAO is an open source multidisciplinary design analysis and optimization framework written in Python in a development led by NASA Glenn Research center.

### 3.1 Airfoil Design Conditions

The design conditions for the airfoil were chosen to match the cruise conditions for the baseline comparison aircraft. As discussed in Section 2, the baseline comparison aircraft was the Boeing “SUGAR Refined” configuration. Based on the analysis discussed in Section 6.1, the sectional cruise characteristics for the SUGAR Refined are a free-stream Mach number of 0.70, with a lift coefficient of approximately 0.60 at  $\alpha \approx 0^\circ$ ,  $h=40$  kFt. The mean aerodynamic chord of the configuration is 144.7 inches. All airfoil design and analysis are targeted to these conditions.

### 3.2 Goldschmied Spanloader Analysis

As a first step in the new design process, the original Goldschmied spanloader concept was studied. The spanloader concept was a thick-airfoil design concept for a cargo aircraft.<sup>13</sup> A schematic of the cross section and layout for the spanloader airfoil is shown in Figure 4. The airfoil has a rather large chord of 420 inches and routes the suction mass flow out the trailing-edge for additional performance. As previously stated, the spanloader section has a thickness ratio of 31.5%, giving it a rather low critical Mach number of 0.45.



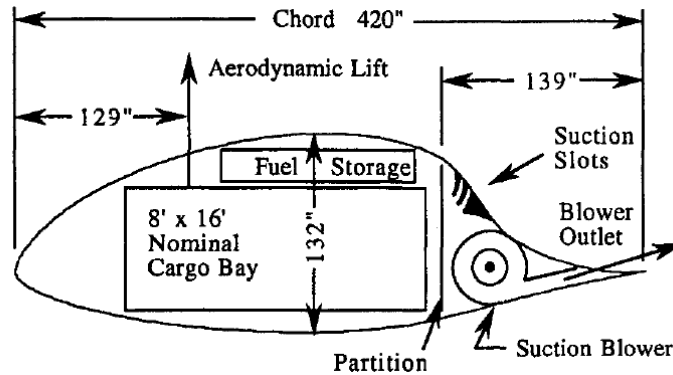


Figure 4: Goldschmied spanloader airfoil cross section.<sup>13</sup>

For the current analysis, the spanloader section coordinates were obtained from Goldschmied.<sup>13</sup> The Goldschmied section was run at the prescribed spanloader flight conditions of  $M_\infty=0.236$ ,  $h = 10$  kFt, for a chord-based Reynolds number of  $60 \times 10^6$ . Suction was applied from 67% to 69% chord on the upper surface. The suction velocity was  $0.10V_\infty$ . The suction conditions were chosen to match those reported by Goldschmied for the aircraft.<sup>13</sup> The case was run fully turbulent using the Spallart-Allmaras 1-equation turbulence model. Contours of Mach number and streamlines for the Goldschmied spanloader section at  $\alpha=0^\circ$  are shown in Figure 5. The suction location is also depicted in Figure 5.

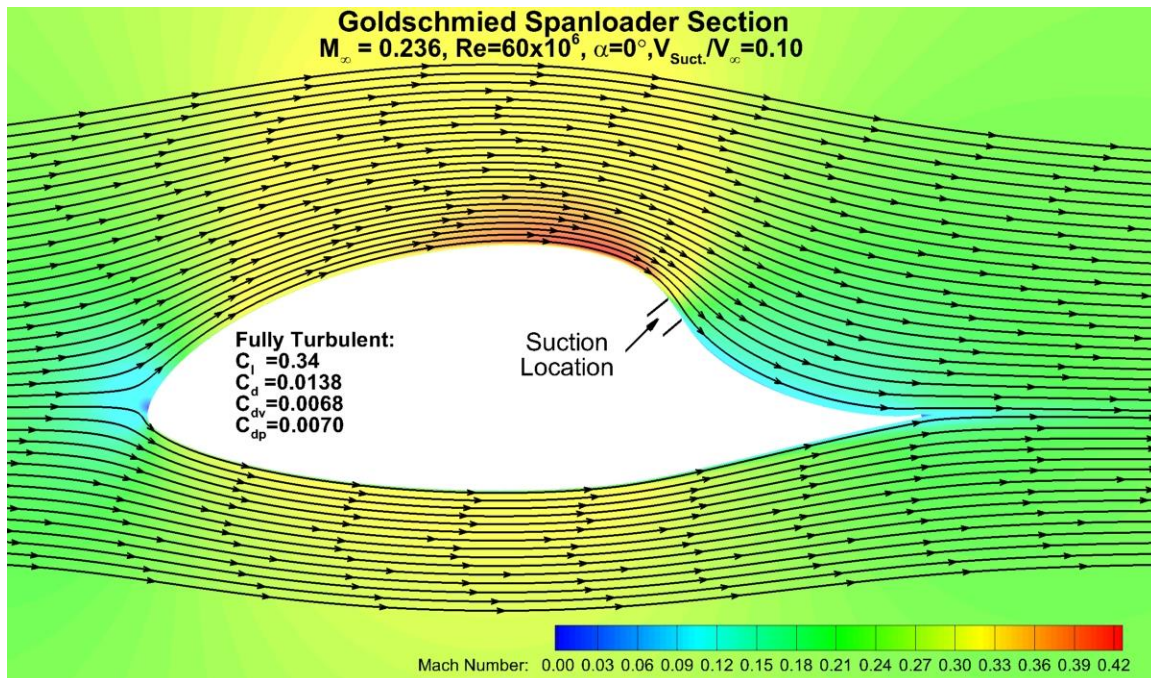


Figure 5: OVERFLOW predicted Mach contours for the Goldschmied spanloader airfoil at  $M_\infty=0.236$ ,  $Re=60 \times 10^6$ ,  $\alpha=0^\circ$ , with a suction velocity of  $0.10V_\infty$ .

From Figure 5, for the Goldschmied prescribed suction level of  $V_s/V_\infty=0.10$ , the flowfield appears fully attached with no separation across the steep aft recovery. The lift coefficient for the  $\alpha=0^\circ$  case is  $C_l=0.34$ , with a total drag of  $C_d=0.0138$ . The pressure drag for the section is  $C_{dp}=0.0070$  with a viscous drag of  $C_{dv}=0.0068$ . While fully attached, the pressure drag for this case is approximately half of the total drag, not the negative or zero pressure drag purported by Goldschmied. It should be noted that the spanloader section described by Goldschmied<sup>13</sup> is a prediction, based on previous subscale wind tunnel investigations. The chord of the spanloader section is 35 ft, producing a significantly higher Reynolds number than any previously tested Goldschmied section. In order to reduce the pressure drag, higher suction levels might be required at the higher Reynolds numbers. Surface pressures for the Goldschmied section are shown in Figure 6.

From Figure 6, the upper surface pressures exhibit the classic Griffith/Goldschmied distribution with a very favorable pressure gradient up to the point of recovery, followed by a very steep adverse gradient enabled by the presence of the active suction. For a transition-free case, one would expect transition to occur around  $x/c \approx 0.60$ . The lower surface transition location would most likely be significantly more forward for this high Reynolds number.

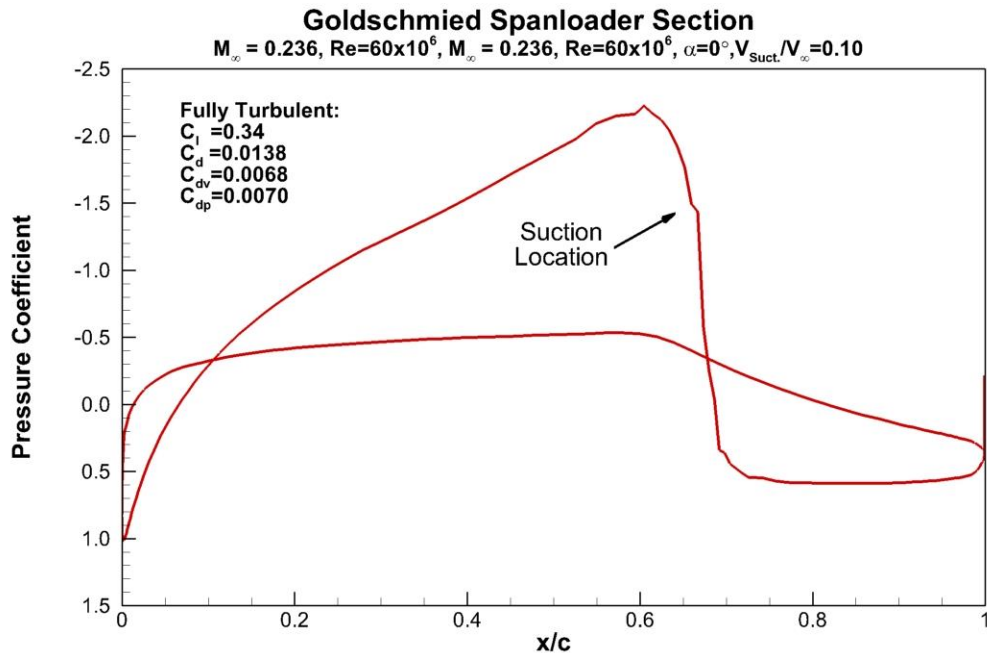


Figure 6: OVERFLOW predicted surface pressures for the Goldschmied spanloader airfoil at  $M_\infty=0.236$ ,  $Re=60 \times 10^6$ ,  $\alpha=0^\circ$ , with a suction velocity of  $0.10V_\infty$ .

In order to obtain an improved understanding of the performance of the Goldschmied spanloader section at the SUGAR refined conditions, the Goldschmied spanloader section was scaled to the SUGAR Refined chord length of 144.7 inches. The SUGAR refined chord Goldschmied section was then run at a free-stream Mach number of  $M_\infty=0.245$ ,  $h =$

10 kFt, for a chord based Reynolds number of  $15.8 \times 10^6$ . Suction was applied for the same chordwise extent as for the full scale section, from 67% to 69% chord on the upper surface. A wide range of suction levels from  $V_s/V_\infty = 0.0$  to 0.20 were run. Additionally, the cases were run transition free using the Langtry-Menter transition model coupled with the two-equation SST turbulence model. Prior to running the transition free spanloader cases, the Langtry-Menter transition model in OVERFLOW was benchmarked using a low Reynolds number S809 section test case provided with OVERFLOW. For the test case, the SST turbulence/Langtry-Menter transition models were able to correctly predict both transition location and the presence of laminar separation bubbles. Contours of Mach number and streamlines as a function of suction level at  $\alpha = 0^\circ$  are shown in Figure 7.

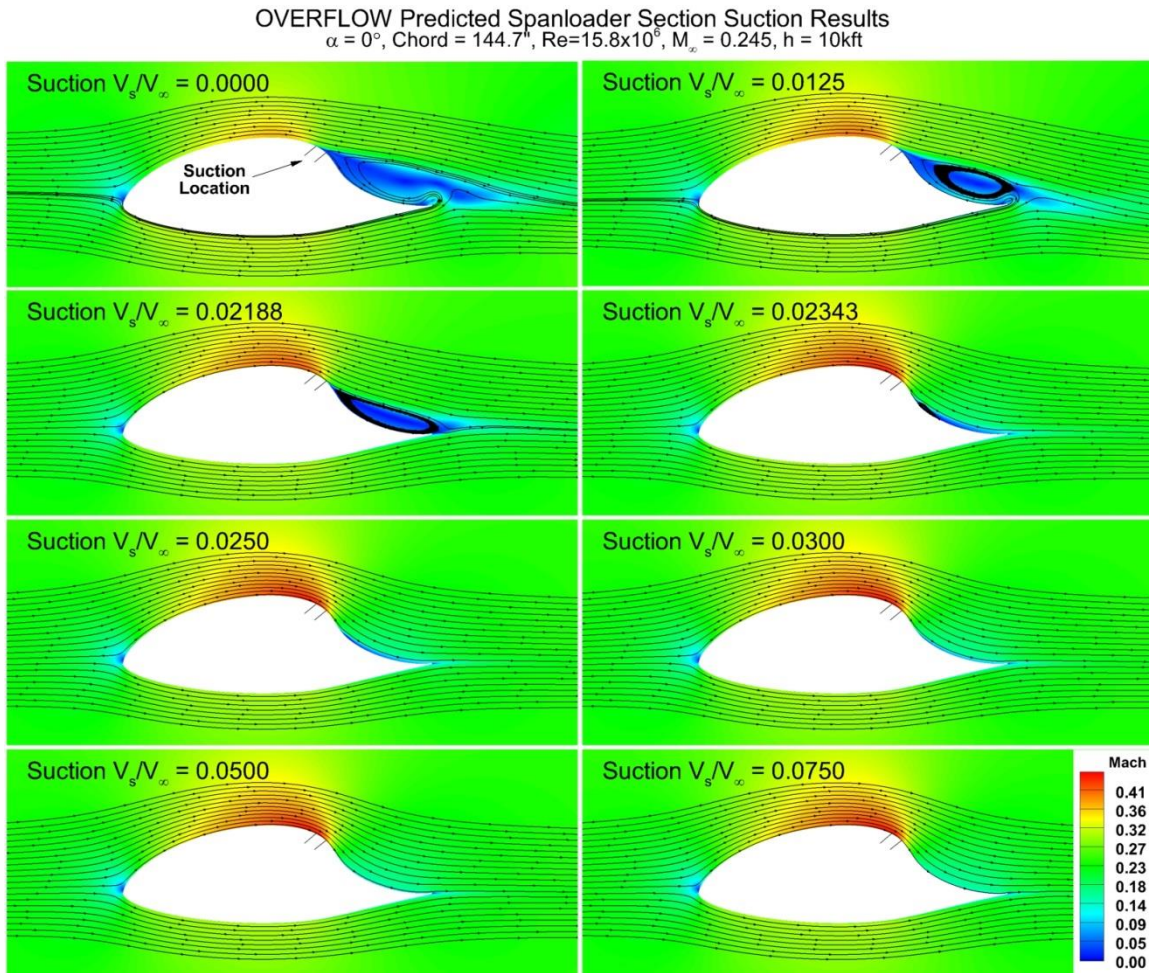


Figure 7: OVERFLOW predicted Mach contours for the Goldschmied spanloader section as a function of suction velocity,  $M_\infty = 0.245$ ,  $Re = 15.8 \times 10^6$ ,  $\alpha = 0^\circ$ .

From Figure 7, for the no suction case up through a suction level of  $V_s/V_\infty = 0.02188$ , a large separated region exists at the onset of the pressure recovery region. A slight increase in suction level, however, to  $V_s/V_\infty = 0.02343$ , significantly reduces the size of the separated region. Above a suction level of  $V_s/V_\infty = 0.025$ , the flow is attached across



the extent of the recovery region. The size of the separated region is very sensitive to the suction level around  $V_s/V_\infty \approx 0.022$ . The suction level required for attached flow for the reduced chord/Reynolds number of the SUGAR Refined spanloader is significantly lower than the level run for the full-scale Goldschmied spanloader concept shown in Figure 5. Again, the levels reported by Goldschmied<sup>13</sup> were predictions based on previous wind tunnel results for a similar configuration. The full size spanloader section may also exhibit attached flow at lower suction levels. Surface pressures for the Mach contours shown in Figure 7 are given in Figure 8.

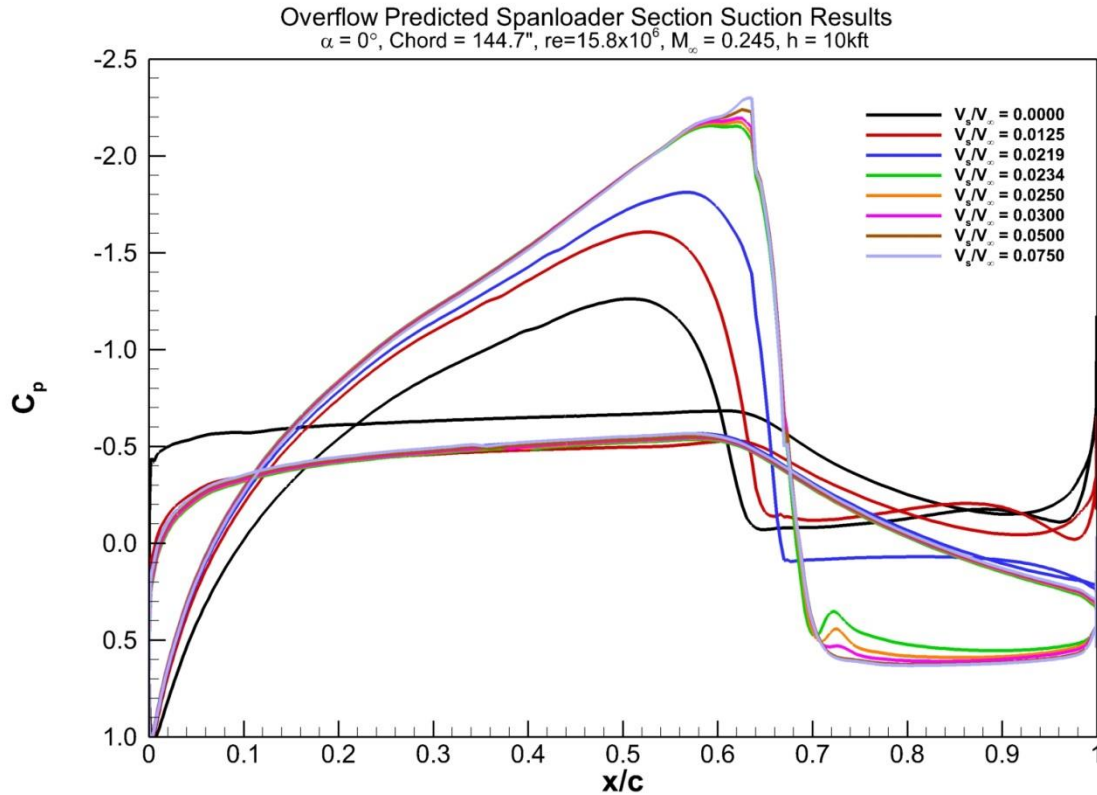


Figure 8: OVERFLOW predicted surface pressures for the Goldschmied spanloader section as a function of suction velocity,  $M_\infty = 0.245$ ,  $Re = 15.8 \times 10^6$ ,  $\alpha = 0^\circ$ .

From Figure 8, at suction levels below  $V_s/V_\infty = 0.02343$ , a large separated region downstream of  $x/c \approx 0.65$  is evident, along with reduced upper-surface suction levels. The upper-surface suction levels increase with increasing suction through the slot, and the amount of separation across the trailing-edge region is reduced. At  $V_s/V_\infty = 0.02343$ , the upper-surface pressures reach a rather constant level that does not change significantly with increasing suction level through the slot. Recall from the surface streamlines in Figure 7 that a small separation bubble still exists at  $V_s/V_\infty = 0.02343$ , with fully attached flow above  $V_s/V_\infty = 0.0250$ . Above  $V_s/V_\infty = 0.0250$ , small increases in the peak pressures at the onset of the pressure recovery are observed with increasing suction level through the slot, as are a slightly more positive pressures aft of  $x/c \approx 0.70$ . Again, the upper surface pressure distributions for the attached suction levels show the classic

Griffith/Goldschmied favorable gradient followed by an abrupt pressure recovery. A plot showing the upper and lower surface transition location as a function of suction velocity is given in Figure 9.

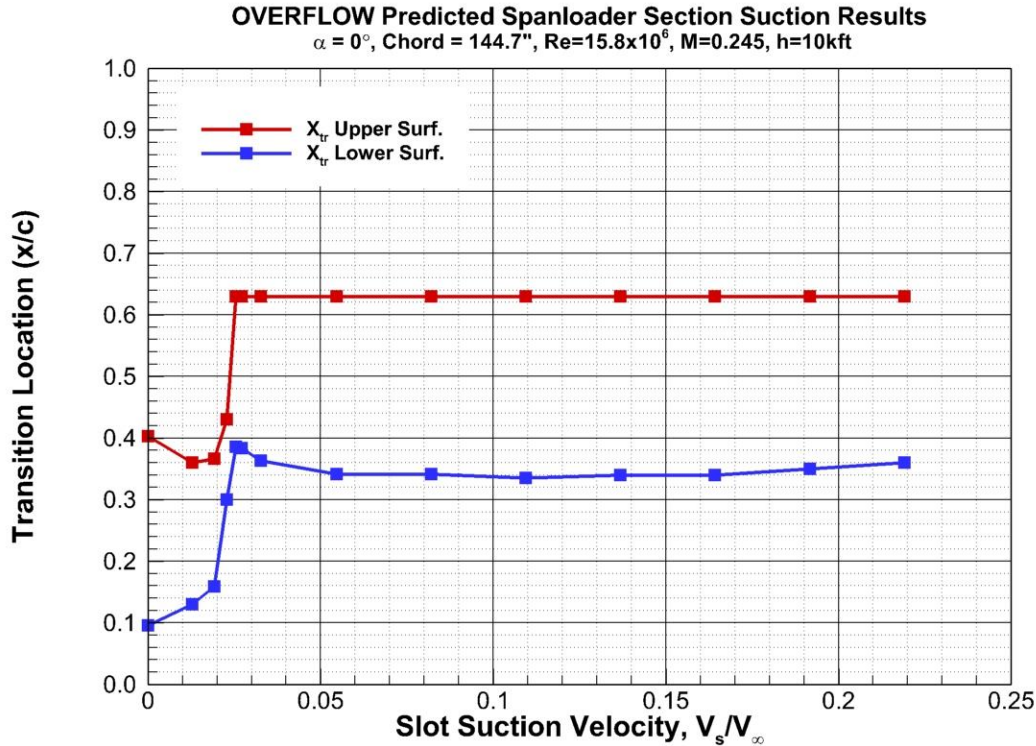


Figure 9: OVERFLOW predicted transition location for the Goldschmied spanloader section as a function of suction velocity using the Langtry-Menter transition model and the SST two-equation turbulence model,  $M_\infty=0.245$ ,  $Re=15.8 \times 10^6$ ,  $\alpha=0^\circ$ .

From Figure 9, for suction velocities below the level required for attached flow ( $V_s/V_\infty=0.0250$ ) the transition location on the upper and surface varies from  $x_{tr}=0.40$  at  $V_s/V_\infty=0.0$  to  $x_{tr}=0.63$  at  $V_s/V_\infty=0.025$  as the flow becomes attached. Above  $V_s/V_\infty=0.025$ , the transition location remains fixed at  $x_{tr}=0.63$ . The transition location is moved this far aft on the airfoil as a result of the very favorable pressure gradient preceding the steep recovery. For the lower surface, which has a much shallower favorable gradient, the transition location varies from  $x_{tr}=0.10$  at  $V_s/V_\infty=0.0$ , moving aft to  $x_{tr}=0.38$  at  $V_s/V_\infty=0.025$ . Increasing the suction level above  $V_s/V_\infty=0.025$  moves the lower transition location slightly forward to  $x_{tr}=0.34$  at  $V_s/V_\infty=0.050$ , where it remains relatively constant with further increases in suction level. The results shown in Figure 9 for the transition location as a function of suction level appear consistent with the pressure distributions shown in Figure 8. Drag predictions for the SUGAR Refined chord spanloader section as a function of suction velocity are shown in Figure 10. Included in Figure 10 are the total drag and both the viscous and pressure drag.

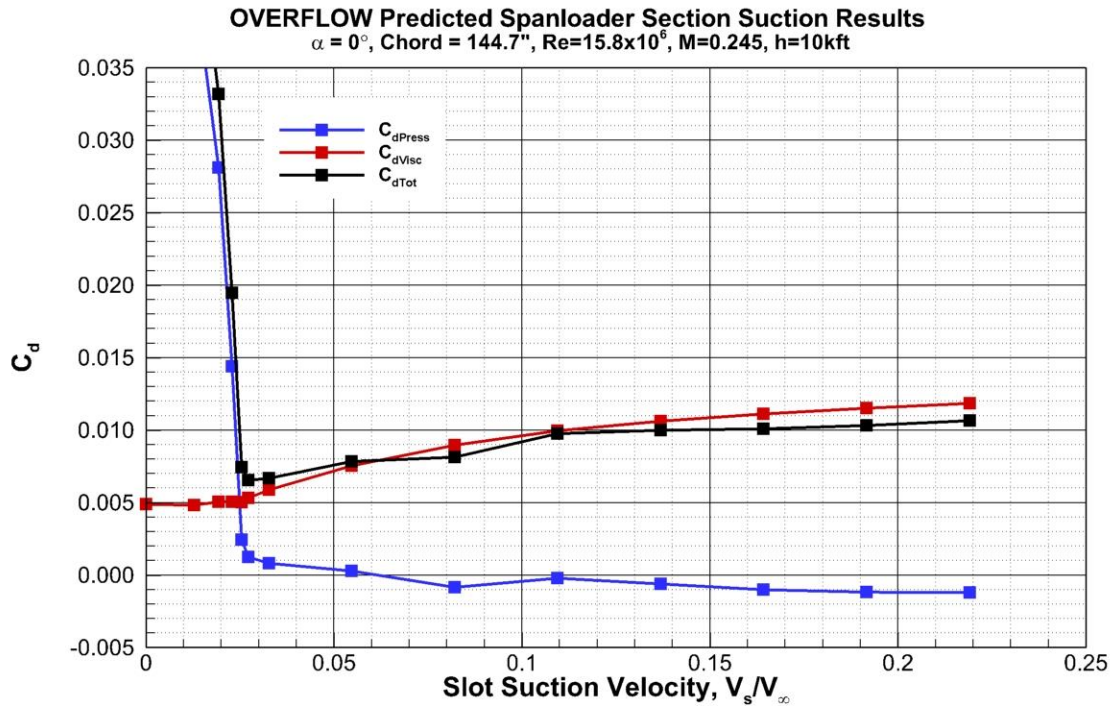


Figure 10: OVERFLOW predicted drag for the Goldschmied spanloader section as a function of suction velocity using the Langtry-Menter transition model and the SST two-equation turbulence model,  $M_\infty = 0.245$ ,  $Re = 15.8 \times 10^6$ ,  $\alpha = 0^\circ$ .

From Figure 10, several interesting trends are apparent. First, the minimum drag occurs at the suction velocity where the separation has just been eliminated,  $V_s/V_\infty = 0.025$ . The pressure drag at  $V_s/V_\infty = 0.025$  is slightly positive at  $C_{dp} = 0.0012$ . Below this suction velocity, the pressure drag rises very quickly as the separation in the recovery region grows rapidly with decreasing suction level. At the low suction levels, with the large separated region, the viscous drag is at a minimum,  $C_{dv} = 0.0053$ . Above the suction velocity required to maintain an attached boundary-layer, increasing the suction level decreases the pressure drag, but increases the viscous drag. Above  $V_s/V_\infty = 0.050$ , the pressure drag becomes negative, but has a very shallow slope with increasing suction level. The minimum pressure drag,  $C_{dp} = -0.0012$  is found at the maximum suction level run,  $V_s/V_\infty = 0.23$ . The skin friction drag, however, increases at a rate faster than the pressure drag decreases with increasing suction level, leading to a higher overall drag with increasing suction. As the suction level increases, the thickness of the turbulent boundary-layer downstream of the suction location decreases, thereby increasing the slope of the velocity gradient at the wall and increasing shear stress at the wall, and therefore skin friction. This result was not intuitively obvious before examining the results, however after further examination the trend makes sense. Since the drag is a combination of both pressure and viscous terms, the minimum drag will occur at a point which simultaneously minimizes both quantities. While higher suction values can reduce the pressure drag, and even provide pressure thrust, they can also increase the skin friction and viscous drag, eliminating the advantages of the reduced pressure drag.



### 3.3 Optimization Set-Up

The optimizer chosen for the Phase I effort was OpenMDAO<sup>24</sup>. OpenMDAO is an open source multidisciplinary design, analysis, and optimization framework written in Python. The development work on OpenMDAO is being led by NASA Glenn Research center. OpenMDAO provides a library of solvers and optimizers in a Python scripting environment. The environment allows quick and easy changes between different solvers and optimizers, allowing fast and efficient exploration of different optimization schemes. OpenMDAO works with both gradient-free and gradient-based optimization methods. The OpenMDAO framework also allows different analysis tools external to the Python environment to be used in the optimization process. For the current study, OVERFLOW is called from within OpenMDAO, as part of an iteration of the optimization process. After a new airfoil shape has been prescribed by the optimizer, a new OVERFLOW input file is generated along with a new grid of the new airfoil shape. OVERFLOW is then run with the force and moment output fed into the objective function. Results from the objective function are then fed back into the optimizer in order to generate a new airfoil shape. The optimization loop continues until the objective function reaches a minimum. The airfoil optimization flow chart is shown in Figure 11.

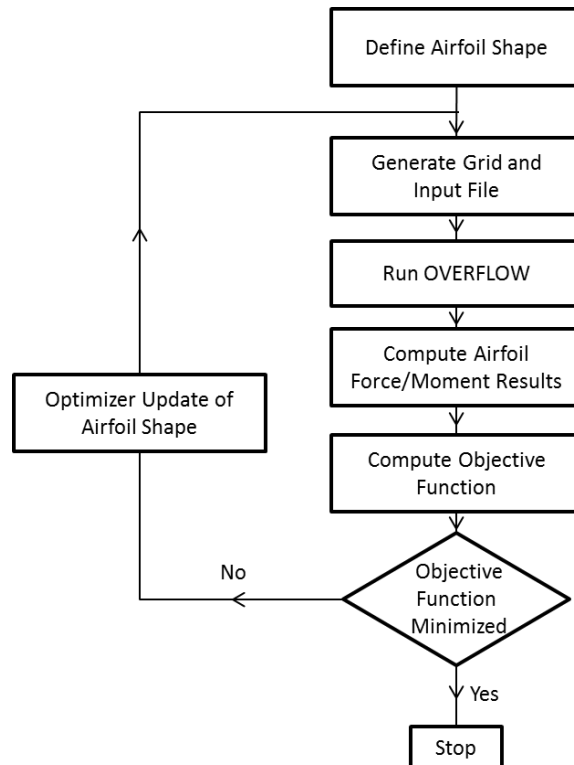


Figure 11: Airfoil optimization flowchart.

### 3.4 Airfoil Parametric Representation

In order to reduce the number of design variables, the airfoil shape generation is parameterized. Using the actual airfoil coordinates for the optimization process would lead to an overly large design space. As a result, the airfoil shape is usually parameterized in an optimization scheme. Several different airfoil parameterizations have been proposed for airfoil optimization, including B-Spline representation<sup>25</sup>, Class/Shape Transformation (CST) methodologies,<sup>26</sup> Bezier curves<sup>27</sup>, the PARSEC method<sup>28</sup>, and several others<sup>29</sup>. While each of these methods has its advantages and disadvantages, a simple Bezier curve representation was chosen for the current project. The Bezier curve representation was chosen for its simplicity and ability to represent arbitrary bodies with a moderate number of control points.

Initially, the Bezier parameterization routine was written using 6 control points to define the airfoil lower surface and a total of 10 control points used to define the upper surface. The upper surface was broken into two segments. The first segment defined the leading-edge region up to the beginning of the steep pressure recovery using 6 control points, with a second region defining the pressure recovery to the trailing-edge using 4 control points. At the intersection of the two upper surface segments, a non-continuous slope was allowed. The non-continuous slope was allowed to account for a sharp change in airfoil contour at the beginning of the pressure recovery as is present in the classic Griffith/Glas II<sup>30</sup> suction-based section. Both x and y coordinates were allowed to vary at the control points. Additionally, a specified trailing-edge thickness was also prescribed. This set-up produced a section with a total of 21 design variables. The parametric Bezier routine was coded into a stand-alone FORTRAN routine that was called from within the OpenMDAO framework.

In order to begin an optimization, an initial seed airfoil is required. Prior to the optimization, the Bezier-based representation of the seed airfoil was generated by using OpenMDAO to minimize the difference between the seed airfoil and the Bezier parameterized section. The results of such an optimization using a low Reynolds number Eppler 550 section as the seed airfoil are shown in Figure 12. From Figure 12, the Bezier curve representation of the baseline Eppler 550 section is very good. The variation of the control points for the upper and lower surface is also apparent. The aft recover region of the airfoil maintains a fairly constant slope, which is reflected in the significantly reduced control point variation over the trailing-edge region.

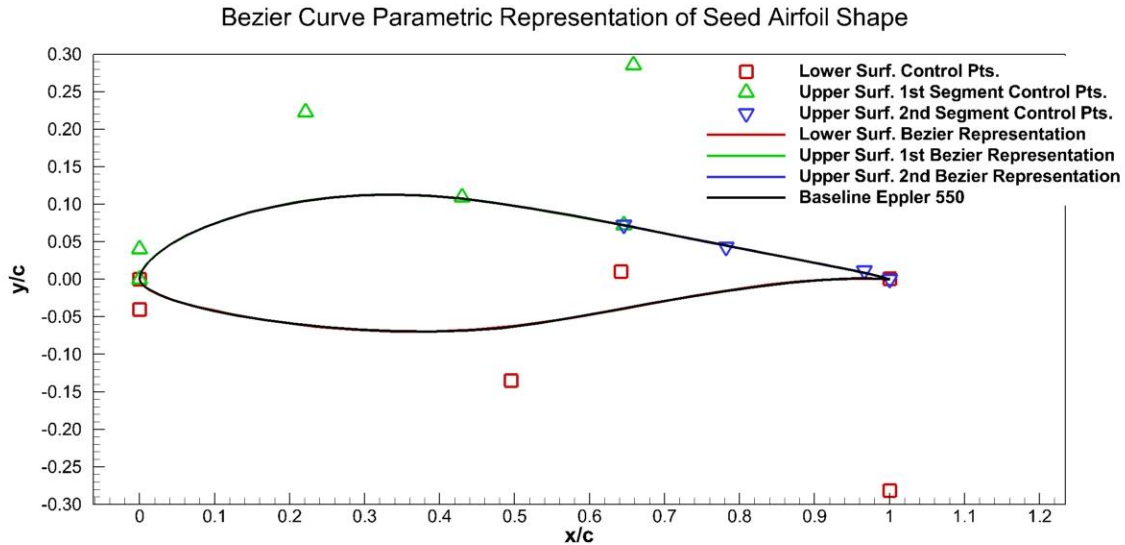


Figure 12: Comparison of baseline seed airfoil and Bezier curve parameterization.

### 3.5 Initial Optimizer Results

Prior to running the OpenMDAO optimization routine on the Griffith/Goldschmied section at transonic conditions using OVERFLOW, the XFOIL<sup>31</sup> airfoil design and analysis code was used to debug the optimization/analysis scripts and to explore the different optimizers present in OpenMDAO. The low Reynolds number Eppler 550 section shown in Figure 12 was used as the optimization starting point. The Eppler 550 section is a good test of the optimizer as it has significant runs of laminar flow on the upper and lower surface. Since the designed transonic Griffith/Goldschmied section will also have significant laminar runs, the optimizer was tested to see if it can maintain or increase the laminar runs during the optimization process in order to lower the overall drag of the section. The baseline Eppler 550 section has a thickness of 18.2%. At  $\alpha=0^\circ$  and a Reynolds number of  $1.0 \times 10^6$ , the XFOIL predicted lift and drag of the Eppler 550 section are  $C_l=0.330$ ,  $C_d=0.00762$ . The upper surface transition location for the baseline section at these conditions is  $x/c_{tr}=0.49$ , with the lower surface transition location at  $x/c_{tr}=0.60$ .

OpenMDAO contains several different optimizers. These include both gradient and non-gradient based optimizers. The available optimizers are shown in Table 4.1. Only the SLSQP optimizer allows equality constraints. All other optimizers allow inequality constraints except the genetic optimizer, which does not allow either equality or inequality constraints. The use of equality or inequality constraints allows a parameter, or parameters, to be driven towards a given value during the optimization. Use of an equality constraint, for example, would allow the optimization to be driven to an exact lift coefficient. An inequality constraint, on the other hand, can be used to keep the airfoil thickness above a given value,  $t/c > 15\%$ , for example.

Optimizer	Gradients	Constraints		Algorithm
		Inequality	Equality	
COBYLA	No	Yes	No	Constrained Optimization by Linear Approximation of the Objective and Constraint Functions Via Linear Interpolation
CONMIN	Yes	Yes	No	Constrained Function Minimization. Implements the Method of Feasible Directions to Solve the Problem
Genetic	No	No	No	Genetic Algorithm
NEWSUMT	Yes	Yes	No	Newton's Method Sequence of Unconstrained Minimizations
SLSQP	Yes	Yes	Yes	Sequential Least Squares

Table 4.1: Optimizers available in OpenMDAO.

All available optimizers were tested using the XFOIL set-up. However, it was identified that none of the optimizers available in OpenMDAO are particularly well-suited for airfoil optimization. The two optimizers which seemed to perform the best were the COBYLA and the NEWSUMT optimizers.

For the first optimization problem, the Eppler 550 section was optimized at  $\alpha=0^\circ$  and a Reynolds number of  $1.0 \times 10^6$ . Inequality constraints were set for the lift coefficient and the thickness,  $C_l \geq 0.34$  and  $t/c \geq 0.18$ , respectively. In addition to the inequality constraints, the lift and thickness were included in the optimizer objective function. The objective function for the optimization was defined as:

$$F(obj) = \left(1 - \frac{C_l}{C_{l,o}}\right)^2 + \frac{C_d}{C_{d,s}} + \left(1 - \frac{t/c}{t/c_o}\right)^2$$

Equation 4.1

Where  $C_{l,o}$  and  $t/c_o$  are desired final lift and thickness, and  $C_{d,s}$  is the seed airfoil baseline drag. Optimization results for the COBYLA optimizer are shown in Figure 13. From Figure 13, the optimization reduced the drag of the section from 0.0076 to 0.0062, an 18% reduction. This reduction was primarily obtained by increasing the upper surface laminar run from  $x/c=0.49$  to  $x/c=0.74$ . The optimizer was able to satisfy both the lift and thickness constraint, reaching the minimum drag after approximately 100 iterations.

The drag value versus iteration in Figure 13 show some drag values below the final minimum drag value. These lower than the final drag value cases represent iterations where either the lift or thickness constraints were not met, resulting in a higher overall objective function. The discontinuity in the airfoil upper surface shape at  $x/c=0.80$  is a

result of the two different Bezier segments used to make up the section upper surface, as the slope was allowed to be discontinuous at this intersection to permit steep initial pressure recoveries across this region.

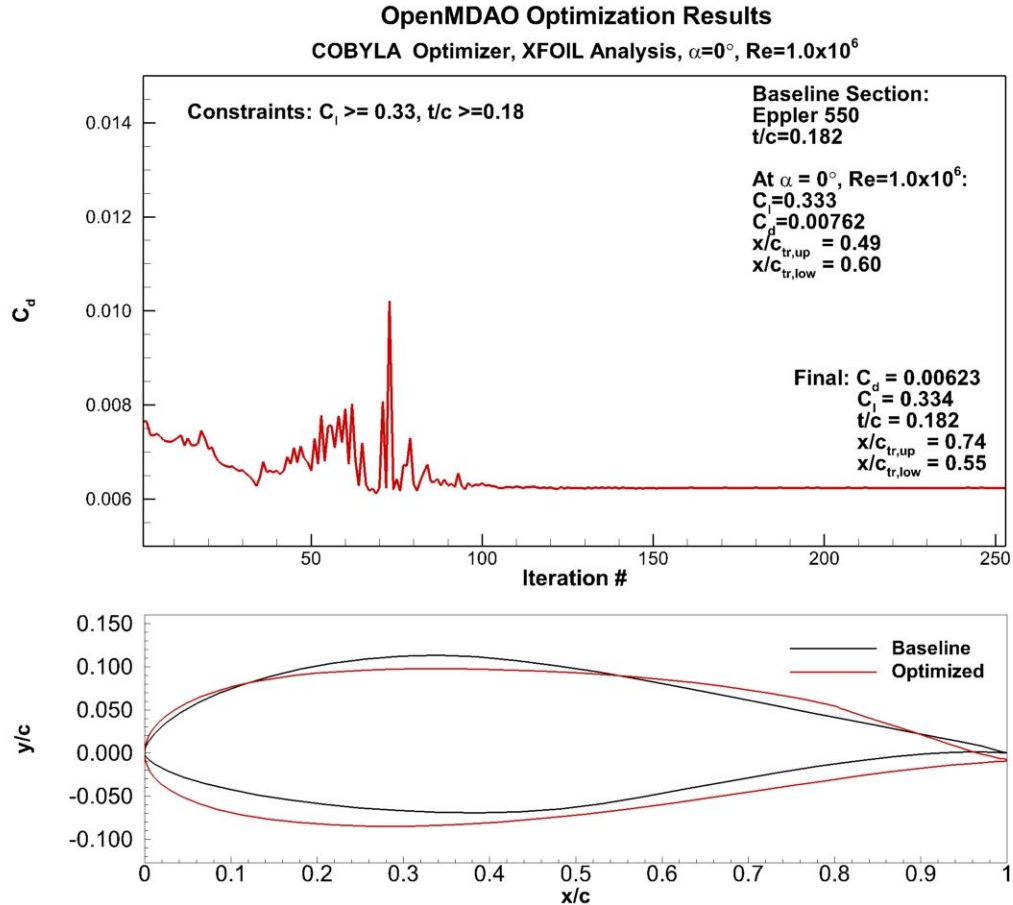


Figure 13: Eppler 550 optimization results using the COBYLA algorithm with a lift and thickness constraint of  $C_l=0.33$  and  $t/c=0.18$ .

Results for the NEWTON optimizer using the same constraints as the COBYLA case shown in Figure 13 are given in Figure 14. From Figure 14, the NEWTON optimizer produces a similar drag to the COBYLA results, but does not hold the thickness constraint as well as the COBYLA case. The NEWTON case has a slightly shorter upper surface laminar run, but a longer lower surface laminar run than the COBYLA case. Of greater importance, however, is the fact that the NEWTON case requires a significantly larger number of iterations. While the COBYLA case converged after approximately 100 iterations, the NEWTON optimizer required over 800. The interesting upper surface trailing-edge shape for the NEWTON case is a result of the single point  $C_l$  optimization. If a multi-point optimization were performed that included different angles-of-attack, the upper surface trailing-edge contour would most likely assume a more traditionally contoured airfoil surface.

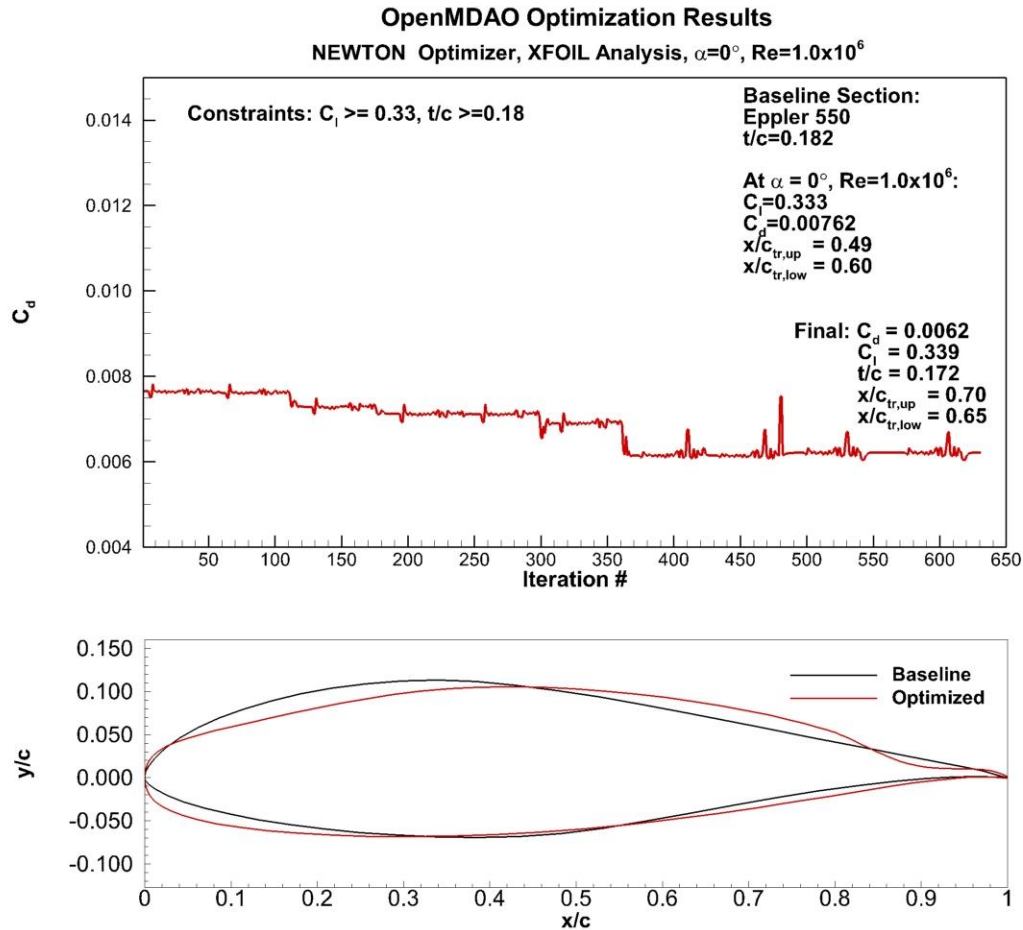


Figure 14: Eppler 550 optimization results using the NEWTON algorithm with a lift and thickness constraint of  $C_l=0.33$  and  $t/c=0.18$ .

Both the COBYLA and NEWTON optimizers were run for a case where the thickness was allowed to drop from 18% to 12%. Results for the 12% COBYLA optimization are shown in Figure 15. From Figure 15, allowing the thickness of the section to drop from 18% to 12% reduces the drag from  $C_d=0.0062$  to  $C_d=0.0056$ , or another 8% reduction in drag, 26% total reduction as compared to the baseline Eppler 550. For this thinner section, transition moved further aft on the upper surface to  $x/c_{tr}=0.79$ , and to  $x/c_{tr}=0.58$  on the lower surface. Unlike the 18% thickness case, however, the 12% COBYLA final thickness was above the prescribed constraint, at  $t/c=0.137$ . Since the constraint is not an equality constraint, but an inequality constraint, the higher than desired thickness is permissible by the optimizer. The lower drag is balanced by the higher thickness in the objective function. Results for the NEWTON optimizer show similar trends to that observed between the COBYLA and NEWTON optimizers for the 18% thickness case.



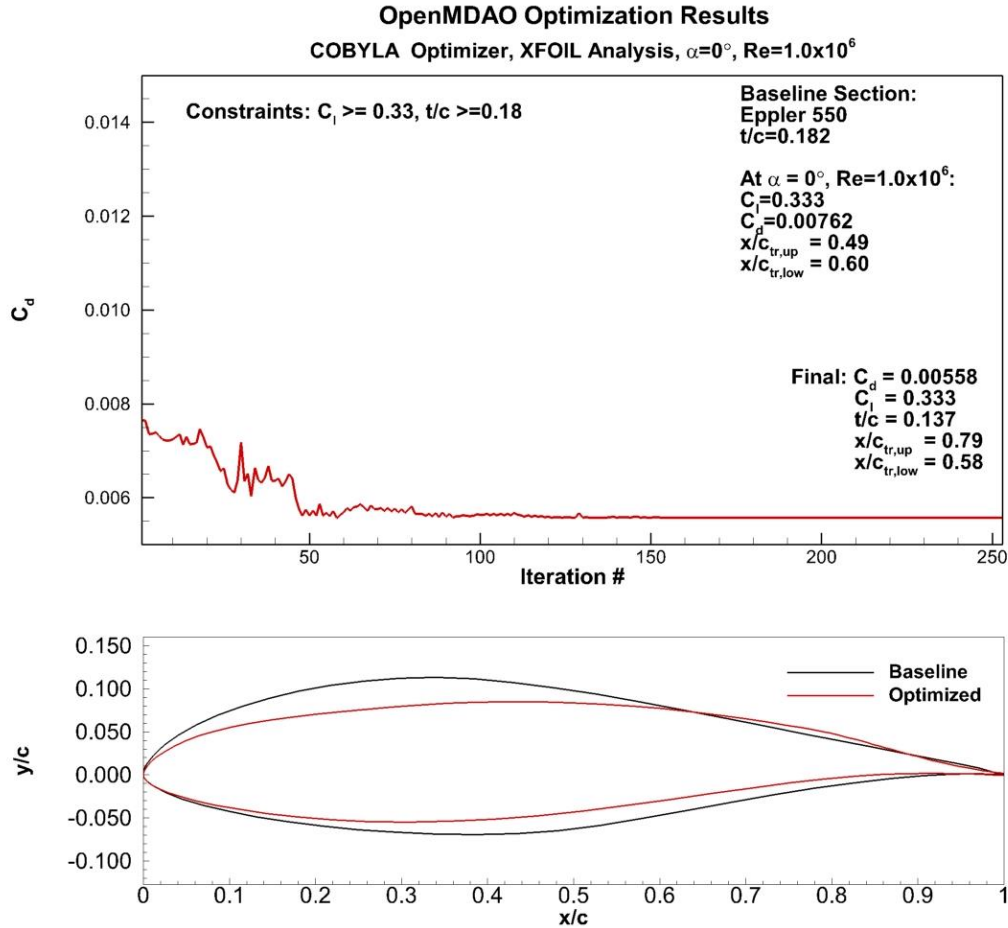


Figure 15: Eppler 550 optimization results using the NEWTON algorithm with a lift and thickness constraint of  $C_l=0.33$  and  $t/c=0.12$ .

For the XFOIL-based initial testing of the OpenMDAO optimizer, the COBYLA optimizer appears to be the most efficient. The COBYLA and NEWTON optimizers were able to generally hold the inequality constraints posed while increasing the laminar run of the section, reducing drag. It should be noted that none of the optimizers present in the basic OpenMDAO package guarantees a global minimum.

After the set-up and debugging of the optimizer system using XFOIL, initial optimization of the Griffith/Goldshmied section was performed using OVERFLOW. Initial optimizations were performed with the simulations assumed fully turbulent. For the OVERFLOW optimizations, in order to reduce run time of the optimization, the airfoil parameterization was modified to fix the x locations of the control points and to make the upper surface one segment where the derivatives are continuous across the entire upper surface. A total of 6 lower surface fixed x locations and 12 upper surface x locations were used for the new parameterization. The y locations of the control points became the design variables for the parameterization. The new system used a total of 17 y locations for design variables. The first optimizations using OVERFLOW also added the suction location and suction chordwise extent as a design variable. The baseline seed airfoil for

the optimization was the section developed and shown in the LEARN Phase I proposal. The airfoil was modeled after Liebeck's high Reynolds number natural laminar flow LF101.<sup>32</sup> Results for the proposal section at  $M=0.60$  are shown in Figure 16. At  $M_\infty=0.60$ , the baseline seed airfoil produces a negative pressure drag of  $C_{dp} = -0.0018$ .

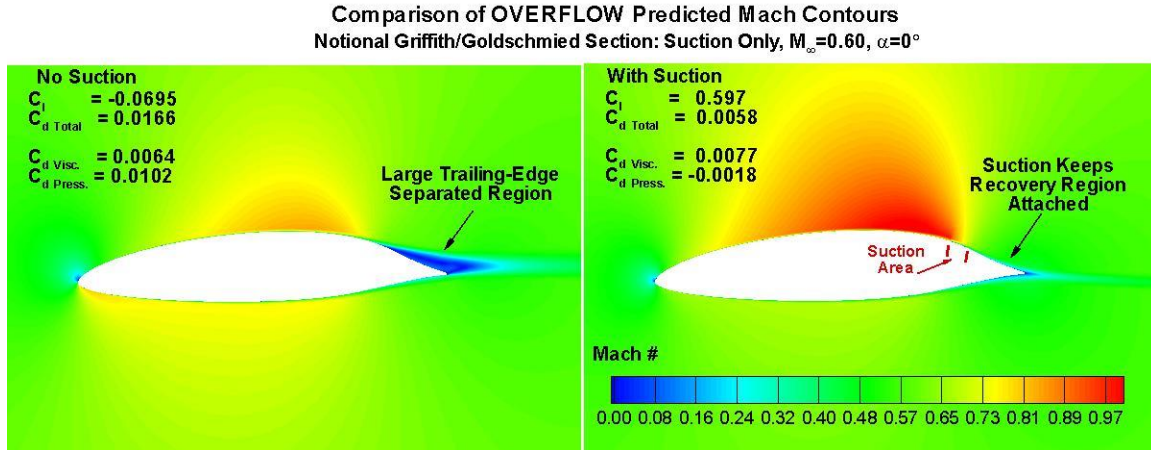


Figure 16: OVERFLOW predicted performance of the baseline seed airfoil based on a Liebeck<sup>32</sup> high Reynolds number natural laminar flow section.

The first optimization was run at  $M_\infty=0.70$  using the COBYLA algorithm. The baseline seed airfoil suction location was set at  $x/c=0.80$  to  $0.85$  with a suction velocity  $V_s/V_\infty=0.065$ . The baseline section thickness was  $t/c=0.188$  with a lift coefficient at  $\alpha=0^\circ$  of  $C_l=0.385$ ,  $Re=24 \times 10^6$ . Since the design lift coefficient for SUGAR Refined section is  $C_l=0.60$ , the optimization constraint was set to  $C_l=0.60$  while allowing the thickness of the section to be reduced to  $t/c=0.15$ . The first optimization attempt posed several significant issues. The primary difficulty was produced since, although limits on the optimizer variables can be set, these limits are not strictly enforced by the optimizer. As a result, the suction location and extent were allowed to vary to unrealistic locations on the airfoil, resulting in significant separation for the majority of the cases generated by the optimizer. Unfortunately the lack of optimizer fidelity to the posed parameter limits is a known issue within OpenMDAO. In order to circumvent this issue, the suction location and extent were fixed for the next optimizer iteration. The new suction extent was reduced from 5% chord beginning at  $x/c_s=0.80$  for the baseline section to 3.5% chord at  $x/c_s=0.82$  to  $0.855$ . The suction velocity was held constant between the two sections at  $V_s/V_\infty=0.065$ . The optimizer performed significantly better using the fixed suction location and velocity. Mach contours and streamlines for the baseline airfoil and the optimized section are shown in Figure 17.

OpenMDAO Single Point Optimization Results  
COBYLA Optimizer,  $M_\infty = 0.70$ ,  $Re=24 \times 10^6$

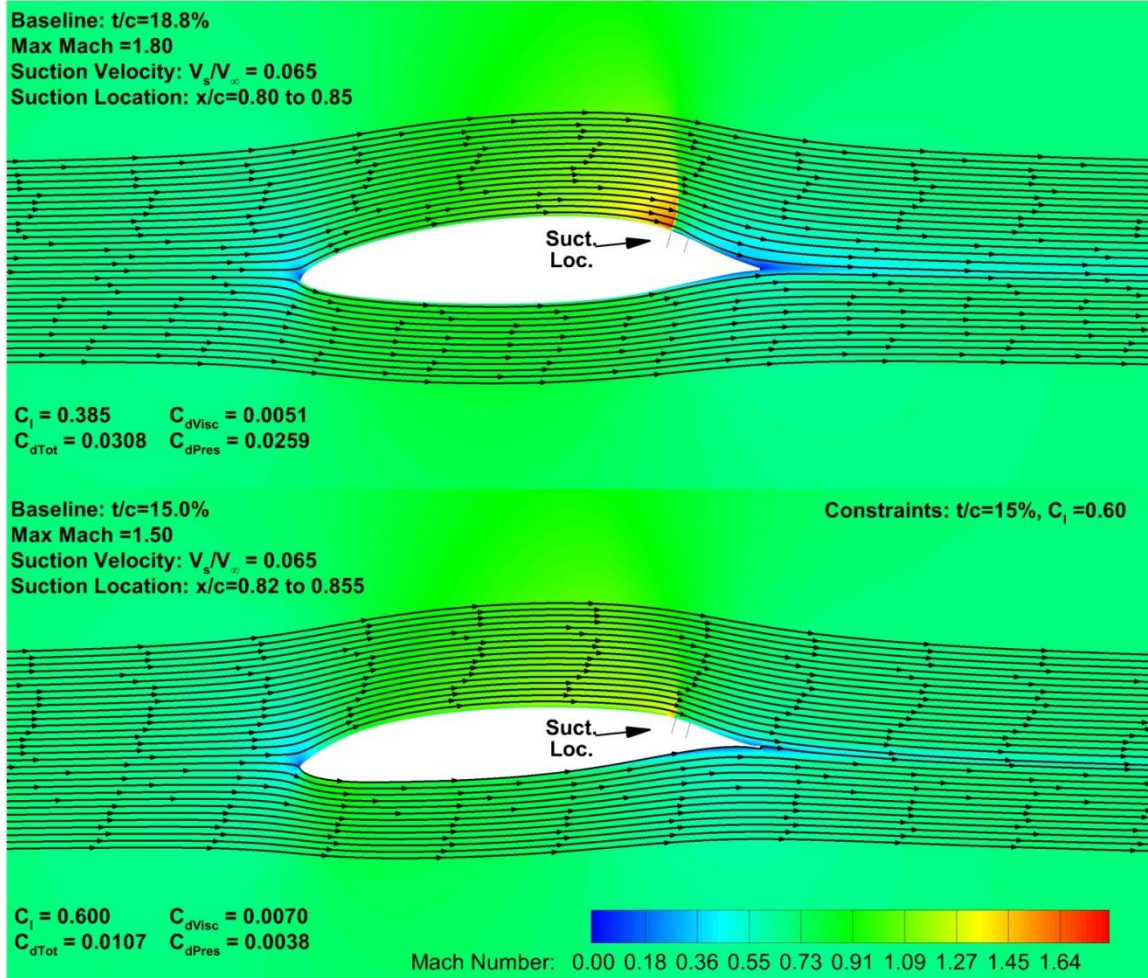


Figure 17: OpenMDAO optimization results for the Griffith/Goldschmied section at  $M_\infty=0.70$ , for a set  $C_l=0.60$  and  $t/c=0.15$ ,  $\alpha=0^\circ$ ,  $Re=24 \times 10^6$ .

From Figure 17, increasing the Mach number for the baseline section from  $M_\infty=0.60$  in Figure 16 to  $M_\infty=0.70$  produced a significant increase in drag for the baseline section. For the  $M_\infty=0.60$  case,  $C_d=0.0058$ . Increasing the free-stream Mach number to  $M_\infty=0.70$ , increases the drag by a factor of five, to  $C_d=0.0308$ . The large drag increase is primarily produced by an increase in pressure drag due to the presence of a strong shock on the upper surface at the initial recovery region. The optimized, reduced thickness section, however, reduces the drag to  $C_d=0.0107$ , a 65% reduction. The maximum Mach number in the baseline section flowfield was 1.8, which was reduced to 1.5 for the optimized section. This significant reduction in drag is impressive noting the increase in lift coefficient from  $C_l=0.385$  to  $C_l=0.60$ . The optimizer effectively reached both the target lift coefficient and thickness. The pressure drag for the optimized section was  $C_{dp}=0.0038$ . While significantly lower than the baseline section at  $C_{dp}=0.0259$ , 38 counts presented a pressure drag significantly higher than that desired for the transonic Griffith/Goldschmied section. The high local Mach number of 1.5 for the optimized case

was most likely the primary reason for the high pressure drag value. A plot showing the drag versus optimization iteration history is given in Figure 18.

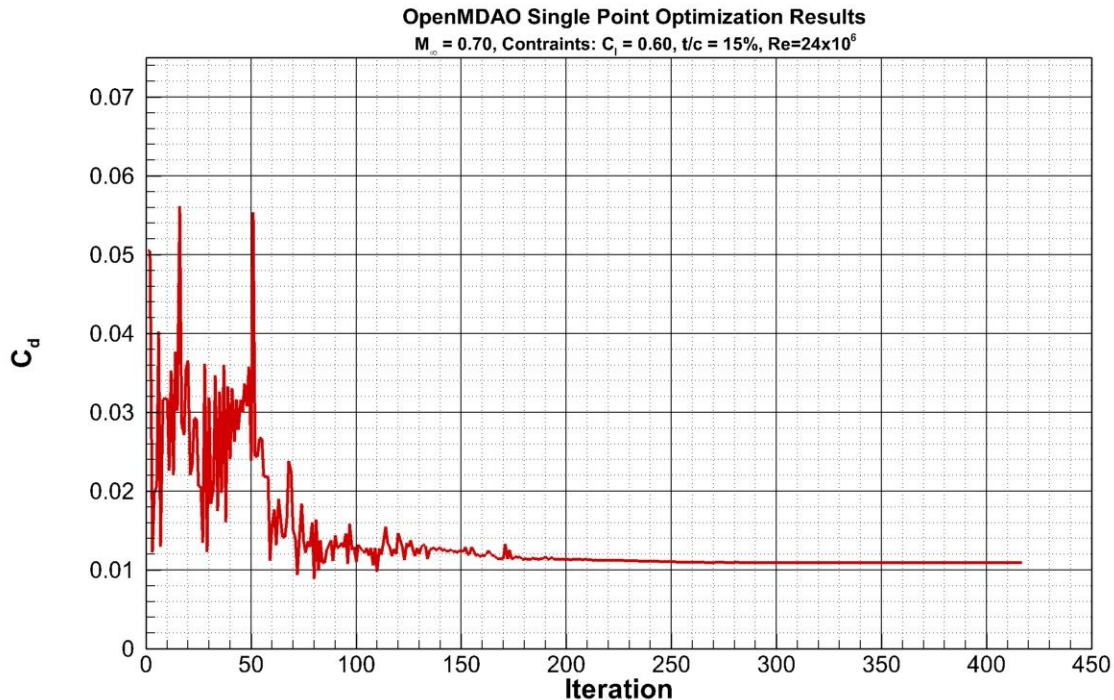


Figure 18: OpenMDAO optimization drag iteration history for the Griffith/Goldschmied section at  $M_\infty=0.70$ , for a set  $C_l=0.60$  and  $t/c=0.15$ ,  $\alpha=0^\circ$ ,  $Re=24 \times 10^6$ .

From Figure 18, the drag reaches a fairly stable minimum at approximately 250 iterations. Large excursions in the drag can be observed early in the optimization cycle. These large excursions were observed to be produced as a result of the section separating as the airfoil contour changes. Overall, the initial optimization attempt appeared very successful for the transonic Griffith/Goldschmied section. Subsequent optimizations, however, did not substantially improve upon the results shown in Figure 17 and Figure 18. Different section thicknesses and starting points were investigated. Several optimizations appeared to become trapped in local minimums. The NEWTON scheme was also revisited.

The Griffith/Goldschmied section was deemed to be a difficult problem for the optimizer. The section is separation dominated, resulting in large variations in the performance of the section for relatively small changes in airfoil contour. This nonlinear behavior is difficult for the optimizer to handle. Another difficulty associated with use of the optimizer was the “black box” nature of the optimizer. While the airfoil produced by the optimizer may have increased performance, the underlying drivers for reduced pressure or viscous drag were masked from the user. It is believed that if a better seed airfoil were provided to the optimizer, more consistent results could be obtained. As a result, it was



decided to utilize a more traditional inverse airfoil design approach over further design attempts with the optimizer.

The traditional inverse airfoil design approach specifies a pressure distribution and then determines the airfoil contour required to achieve the desired pressure distribution. It was envisioned that by performing a more traditional inverse design, a significantly better understanding the driving factors on reducing the pressure drag of the suction based section could be obtained. This increased understanding of the underlying physics behind pressure drag, or pressure thrust, would allow for a significantly better baseline airfoil to be passed to the optimizer, reducing the chances of becoming trapped in a local minimum, and producing more consistent results from the optimizer.

### 3.6 Parametric Investigations

In addition to the OpenMDAO optimization, a more traditional inverse airfoil approach was also explored in order to attempt to gain a better understanding of the driving factors behind reduced pressure drag for the suction based Griffith/Goldsmith section. By developing an inverse design approach, systematic changes in the pressure distribution were explored to determine their effect upon the performance of the section. The systematic changes allowed for a parametric investigation to be undertaken which provided a much clearer understanding of the underlying factors affecting the pressure drag and performance of the section. Prior to the inverse airfoil design study, a few basic parametric investigations were performed.

In support of the parametric study, a new baseline, symmetric airfoil was developed based on a modified Liebeck section. The thickness of the symmetric section was varied from  $t/c=0.25$  to  $t/c=0.12$  to determine the effect of sectional thickness on the pressure drag. Since larger thicknesses were investigated, the Mach number was reduced from  $M_\infty=0.70$  to  $M_\infty=0.60$  to avoid large shock losses. At  $M_\infty=0.60$ , for the SUGAR Refined chord length at  $h=40$  kFt, the Reynolds number for the section was  $Re=13.8 \times 10^6$ . A rather large suction region from  $x/c=0.72$  to  $0.85$  was used. The suction level was set to the same value for all of the varying thickness cases at  $V_s/V_\infty=0.060$ . The cases were run fully turbulent to isolate the thickness effect. The airfoil contours and OVERFLOW-predicted pressure drag and surface pressure distributions for the various thicknesses investigated are shown in Figure 19. Since the airfoils are symmetric and run at  $\alpha=0^\circ$ , only the upper surface pressure distributions are shown.

From Figure 19, the largest pressure drag reduction was obtained with the thickest section,  $t/c=0.25$  at  $C_{dp} = -0.0060$ . The magnitude of the pressure thrust was observed to decrease with decreasing section thickness. At  $t/c=0.12$ ,  $C_{dp} = -0.0034$ , a 43% reduction in the pressure thrust benefit. Decreasing the section thickness reduced the magnitude of the favorable gradient upstream of the recovery point, but also reduced the severity of the adverse gradient in the recovery region. Decreasing the thickness also reduced the absolute level of the pressures, producing less negative pressures on the upper surface. From Figure 19 it is unclear which has a larger effect upon the generation of pressure

thrust, the magnitude of the favorable gradient, or the absolute level of the pressures. It is also possible that the combination of the magnitude of the favorable gradient coupled with the pressure levels was the principal factor that drove the level of pressure thrust generation.

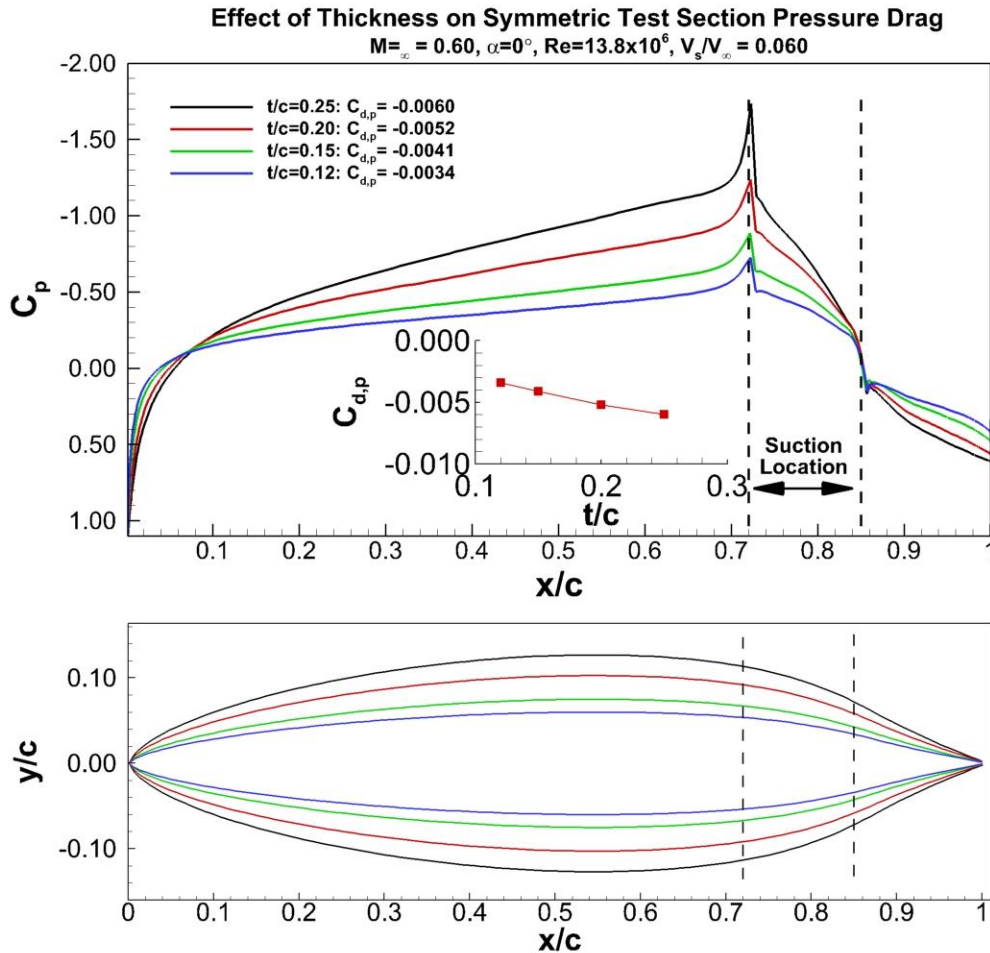


Figure 19: Effect of thickness on symmetric test airfoil pressure drag and surface pressures,  $M_\infty=0.60$ ,  $\alpha=0^\circ$ ,  $Re=13.8 \times 10^6$ ,  $V_s/V_\infty=0.060$ .

After examining the effect of the section thickness, angle-of-attack and transition effects were examined for one of the thicknesses at  $M_\infty=0.70$ . Since increasing the free-stream Mach number to  $M_\infty=0.70$ , would produce large shocks for the 25% and 20% thicknesses, the 15% thickness section was used to study the effect of  $\alpha$  and transition. The suction level was also slightly increased from  $V_s/V_\infty=0.060$  to  $V_s/V_\infty=0.075$ . Angles-of-attack of  $0^\circ$ ,  $1^\circ$ ,  $2^\circ$ , and  $3^\circ$  were run at  $M_\infty=0.70$  for the SUGAR Refined chord length, at a Reynolds number of  $16 \times 10^6$ . Surface pressures for the four angle-of-attack cases are shown in Figure 20.

From Figure 20, as the angle-of-attack increases, the magnitude of the favorable gradient on the upper surface upstream of the recovery region decreases. As a result, transition was observed to move forward on the upper surface with increasing  $\alpha$ , from  $x/c_{tr}=0.72$  at



$\alpha=0^\circ$ , to  $x/c_{tr}=0.15$  at  $\alpha=3^\circ$ . A shock was also present at the onset of the recovery region. As the angle-of-attack was increased, the strength of the upper surface shock increased, while the lower surface shock became weaker. The maximum flowfield Mach number for the  $\alpha=3^\circ$  case was 1.32. Downstream of the shock, the surface pressure across recovery region was roughly equivalent for the different angles-of-attack. Lift and drag results for the 15% thick section as a function of angle-of-attack are shown in Figure 21.

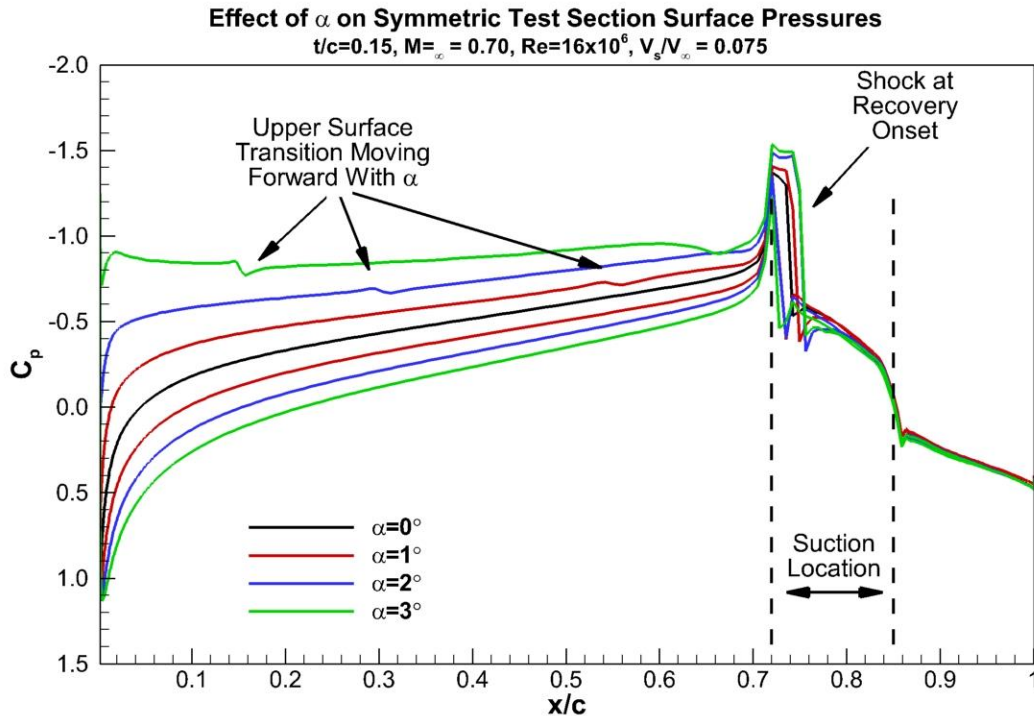


Figure 20: Effect of angle-of-attack on the 15% thick symmetric test airfoil surface pressures and transition location,  $M_\infty=0.70$ ,  $\alpha=0^\circ$ ,  $Re=16 \times 10^6$ ,  $V_s/V_\infty=0.075$ .

From Figure 21, the lift coefficient was observed to increase linearly with increasing  $\alpha$ , as would be expected. The section was also observed to produce a pressure thrust from  $C_{dp} = -0.0045$  at  $\alpha=0^\circ$ , reducing in magnitude to  $C_{dp} = -0.0023$  at  $\alpha=3^\circ$ . Since transition on the upper surface moved forward with increasing angle-of-attack, the viscous drag also increased with increasing  $\alpha$ . The total drag of the section varied from  $C_d = 0.0005$  at  $\alpha=0^\circ$  to  $C_d = 0.0035$ . Although the airfoil used quite a large amount of suction, a total drag of 35 counts for a lift coefficient near 0.60 at  $M_\infty=0.70$  was deemed to be a promising result. Reducing the shock strength and tailoring the pressure gradient to move the upper surface transition point aft should further increase performance. Also of significant note is the fact that although shock is present, a respectable 35 drag count section was still produced, lending support to the development of a Griffith/Goldschmied section for a higher free-stream Mach number.

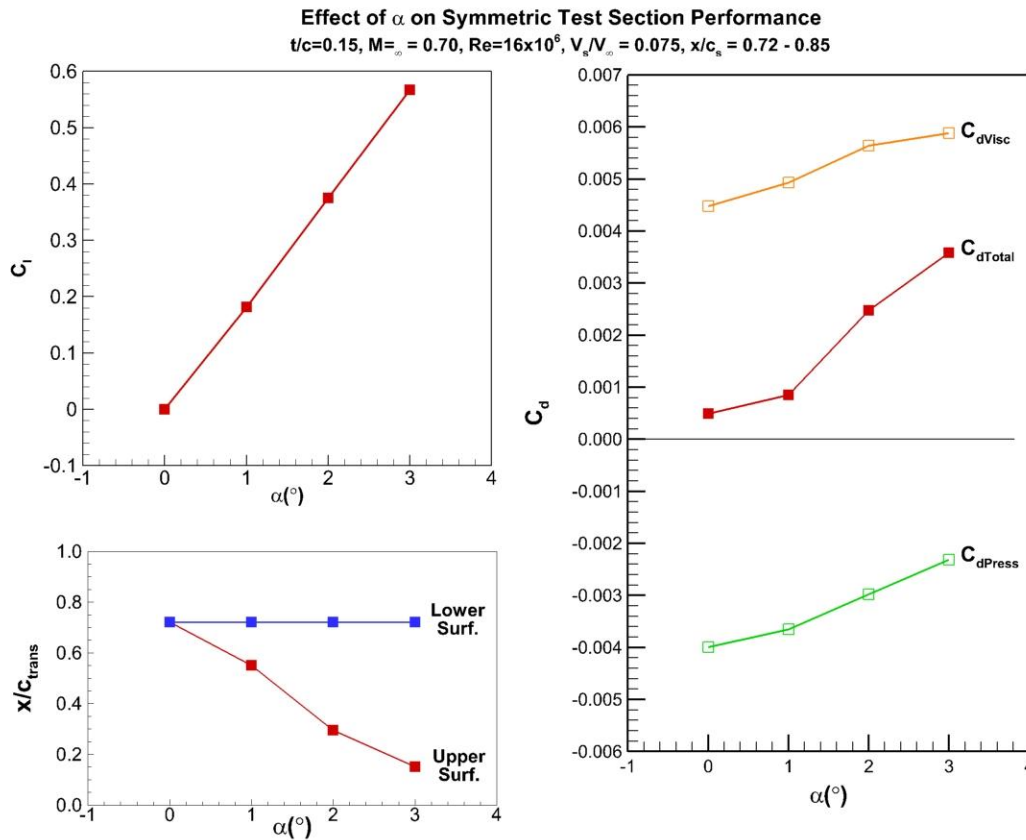


Figure 21: Effect of angle-of-attack on the 15% thick symmetric test airfoil performance and transition location,  $M_\infty=0.70$ ,  $Re=16 \times 10^6$ ,  $V_s/V_\infty=0.075$ .

The effect of suction extent was also investigated using the 15% thick symmetric airfoil section. The chordwise extent of the suction was varied from 5% to 13% chord. The aft location of the suction slot was held constant at  $x/c_s=0.85$ , while changing the suction start location for the different suction extents across the surface. The 13% suction extent, for example had a suction location of  $x/c_s=0.72-0.85$ , whereas the 5% suction extent had a suction location of  $x/c_s=0.80-0.85$ . The suction extent cases were run at  $\alpha=3^\circ$ ,  $M_\infty=0.70$ ,  $Re=16 \times 10^6$ ,  $V_s/V_\infty=0.075$ . Drag performance as a function of suction extent for the symmetric test airfoil is shown in Figure 22.

From Figure 22, decreasing the suction extent reduces the magnitude of the pressure thrust, but also reduces the viscous drag. While increasing the suction level can reduce the pressure drag, the reduced thickness of the boundary layer, downstream of the suction location, was observed to increase skin friction. For the suction extent results shown in Figure 22, the increase in pressure drag with decreasing suction extent, however, was greater than the reduction in viscous drag. Reducing the suction extent from 13% to 5% increased the total drag from  $C_d=0.0036$  to  $C_d=0.0053$ . While 53 counts is still an overall low drag value, it represents a 47% increase from the 13% suction extent. The reduction in suction extent, however, represents a substantial 61% reduction in the required suction

volumetric flow rate. This observation provided clear evidence of a trade-off between the overall drag of the section and the suction extent, which would be considered for the design of the transonic Griffith/Goldschmied airfoil section. While reduced overall drag values could be obtained by increasing the suction extent, the large mass flow requirements resulting from increased suction effect were considered to be detrimental from an overall systems and energy balance standpoint.

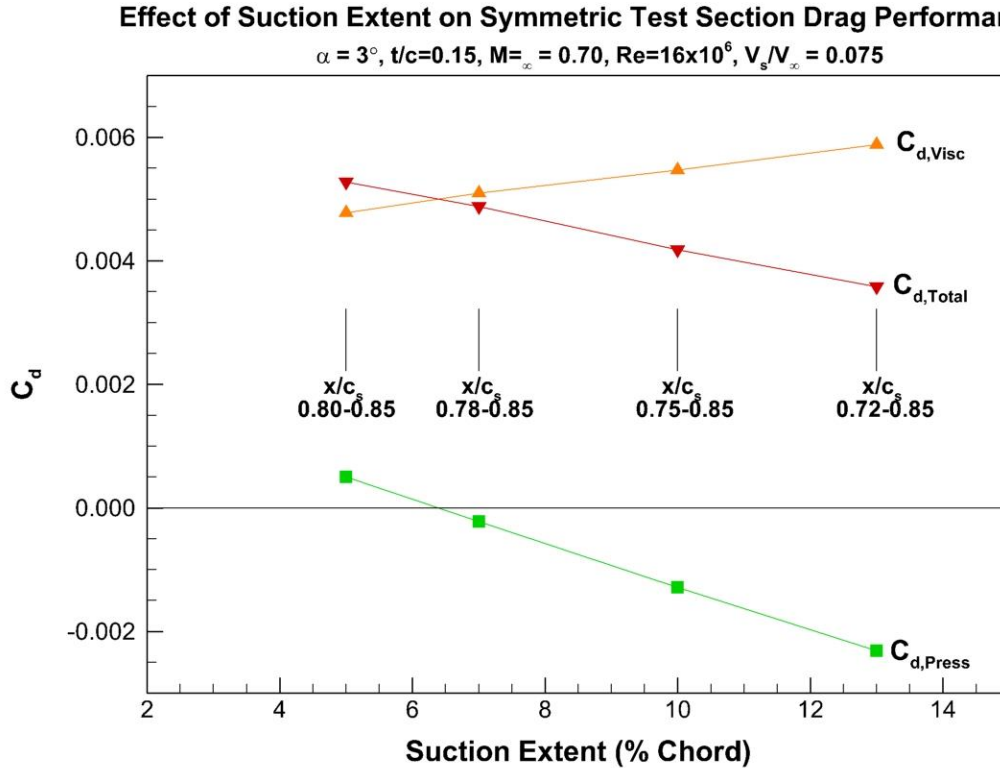


Figure 22: Effect of suction extent on the 15% thick symmetric test airfoil drag performance,  $M_\infty=0.70$ ,  $\alpha=3^\circ$ ,  $Re=16 \times 10^6$ ,  $V_s/V_\infty=0.075$ .

### 3.7 Inverse Airfoil Design Approach

The inverse airfoil design code Profoil<sup>33</sup> is an inviscid Euler code, developed by Michael Selig of the University of Illinois, which allows the user to specify the desired pressure distribution, and will calculate the airfoil shape that will provide it. The shape produced through Profoil was then analyzed using the OVERFLOW CFD program. By controlling the shape of the pressure distribution, the designer can maintain laminar flow over an extended chord length, while balancing the requirements of a Goldschmied section to obtain the most pressure thrust possible.

The pressure drag coefficient on an airfoil at  $\alpha = 0^\circ$  is defined by:

$$C_{d,p} = \int_0^c (C_{P,Upper} - C_{P,Lower}) dy$$

Anywhere along the chord where the quantity  $C_p dy$  is positive, a pressure drag contribution is produced. However, if the quantity  $C_p dy$  is negative, a pressure thrust contribution is produced. This can be visualized by considering the airfoil shape shown in Figure 23. Any change in the airfoil surface that moves away from the chord line is considered to be a positive  $dy$ , while a slope toward the chord line is a negative  $dy$ . If a positive pressure exists on a negative  $dy$  segment, a pressure thrust is created. Likewise, a negative pressure on a positive  $dy$  will also create a pressure thrust. Pressure thrust contributions across the airfoil surface are shown in Figure 23 as green, while pressure drag areas are shown in red.

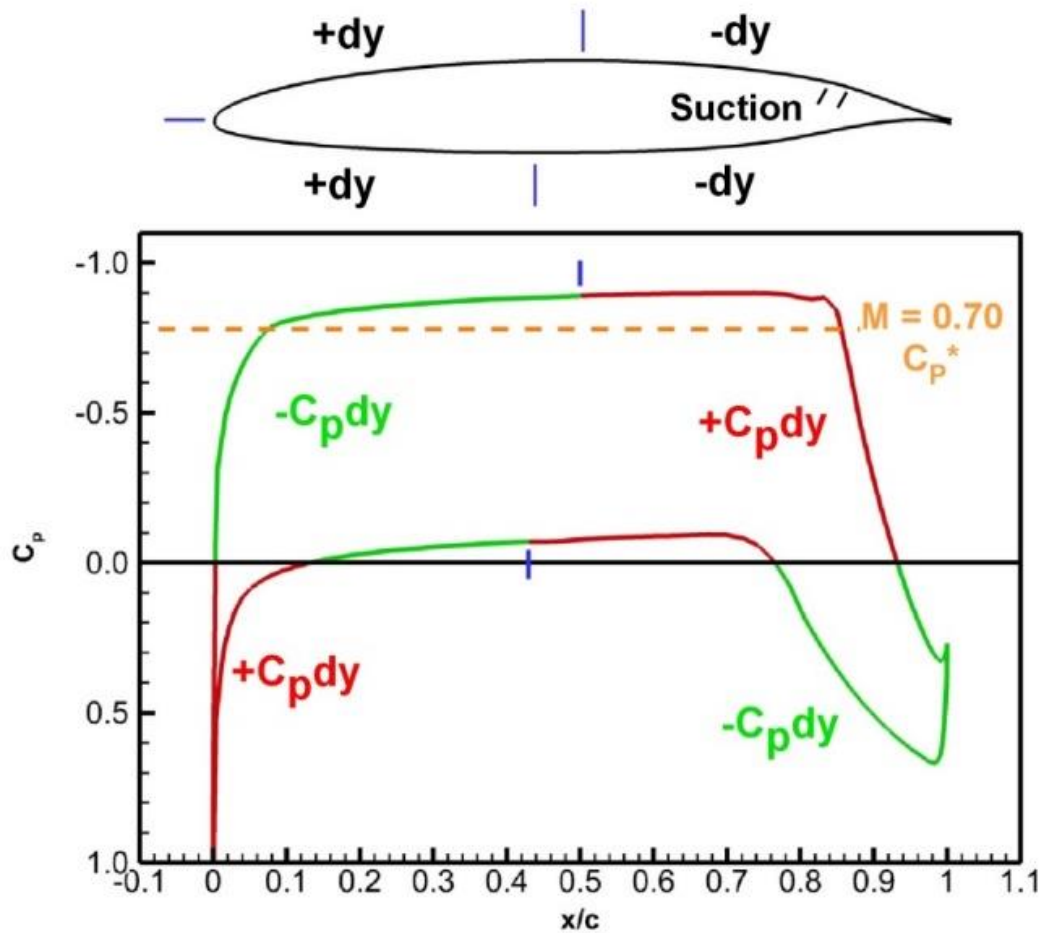


Figure 23: Regions on the airfoil that contribute to pressure thrust and drag



### 3.8 Symmetric Airfoil Study to Understand Contributions to Pressure Thrust

In order to better understand the airfoil design tradeoffs that would allow a high performance transonic Goldschmied section to obtain maximal pressure thrust, the simplified case of a symmetric section was studied.

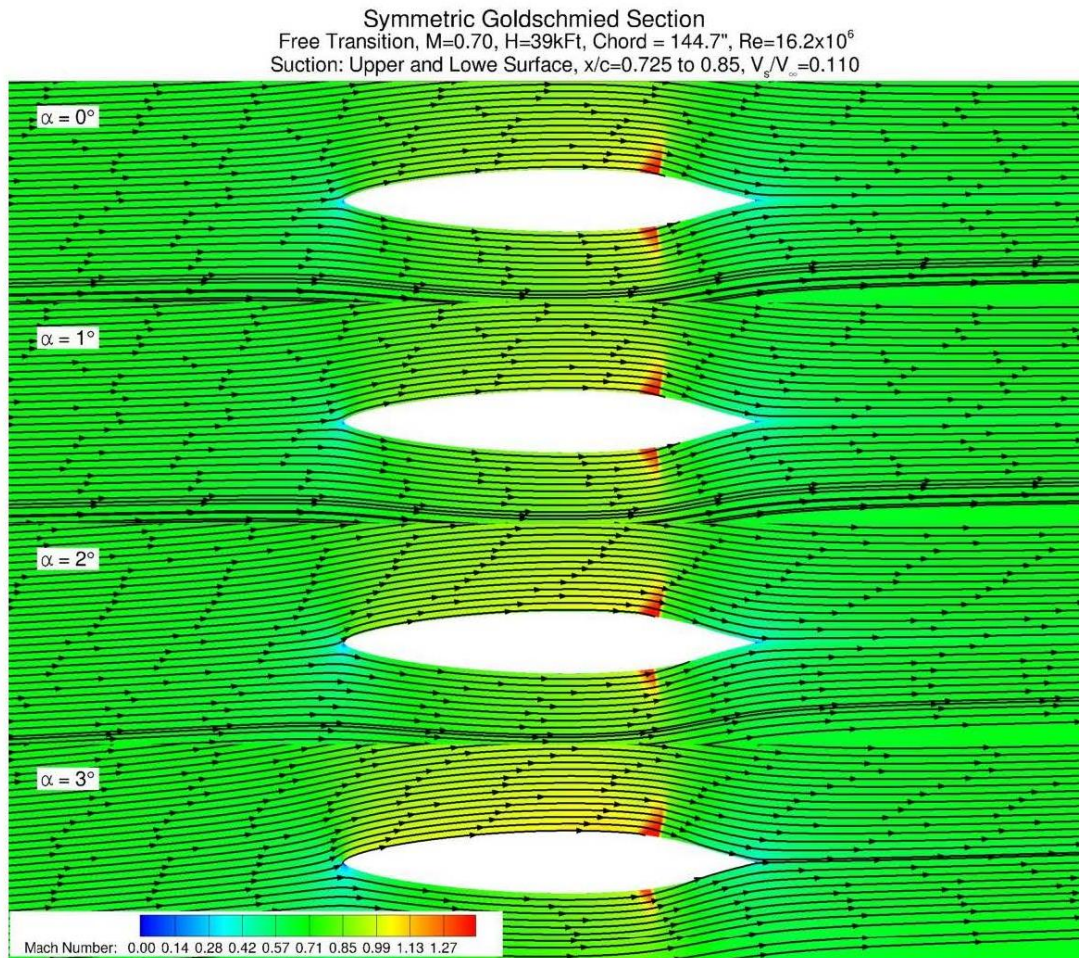


Figure 24: Mach Contours around a Symmetric Goldschmied Section

Figure 24 shows the Mach contours around a symmetric Goldschmied section that was scaled to the SUGAR-Refined with a chord length of 144.7". At  $M=0.70$  and an altitude of  $H=39k$ , this resulted in a  $Re=16.2 \times 10^6$ . Suction was applied between  $x/c=72.5\%$  and  $85\%$  at a  $V_s/V_\infty=0.110$  on both the upper and lower surfaces. This demonstration proved that even with a relatively thick section, it was possible to maintain attached flow using suction.

Figure 25 shows a comparison of airfoil performance produced between a fixed turbulent flow and a predicted natural transition at the prescribed design flight conditions.

Although the total drag was similar in both cases, it can be seen that the transitional case has higher viscous drag but also a nearly offsetting amount of pressure thrust.

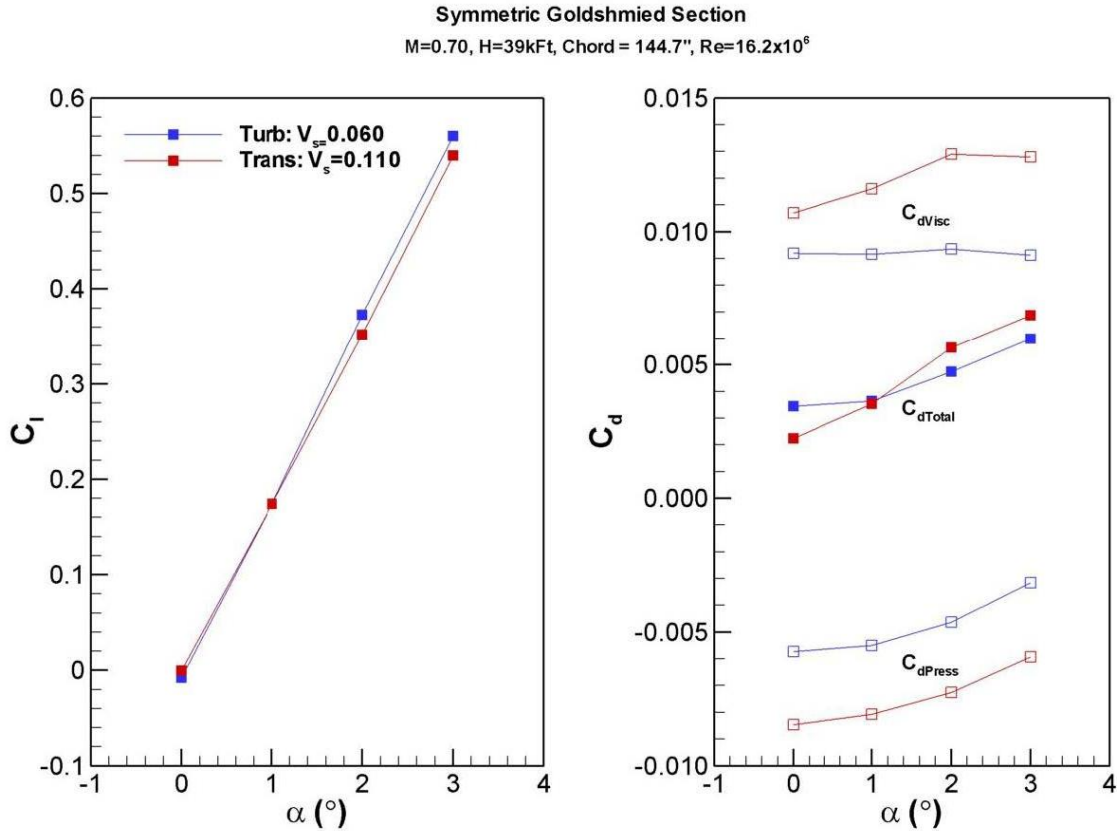


Figure 25: Effect of Fully Turbulent versus Transitional Flow Constraint

Figure 26 shows the effect of angle-of-attack on the upper surface pressure distributions. At  $0^\circ$ , the overall contribution of the upper surface to pressure drag was -0.00199, resulting in a net thrust. It can be seen that the thrusting component was produced entirely from the pressure acting on the  $dy \cos(\alpha)$  segments. The thrust was observed to decrease as AOA increases, and by  $\alpha=3^\circ$  it becomes a drag force.

Figure 27 shows the effect of angle-of-attack on the lower surface pressure distributions. Again at  $0^\circ$ , the  $dy \cos(\alpha)$  contribution of the lower surface to pressure drag was -0.00199, which results in a thrusting contribution. However, as AOA increases the  $dx \sin(\alpha)$  contribution becomes negative.



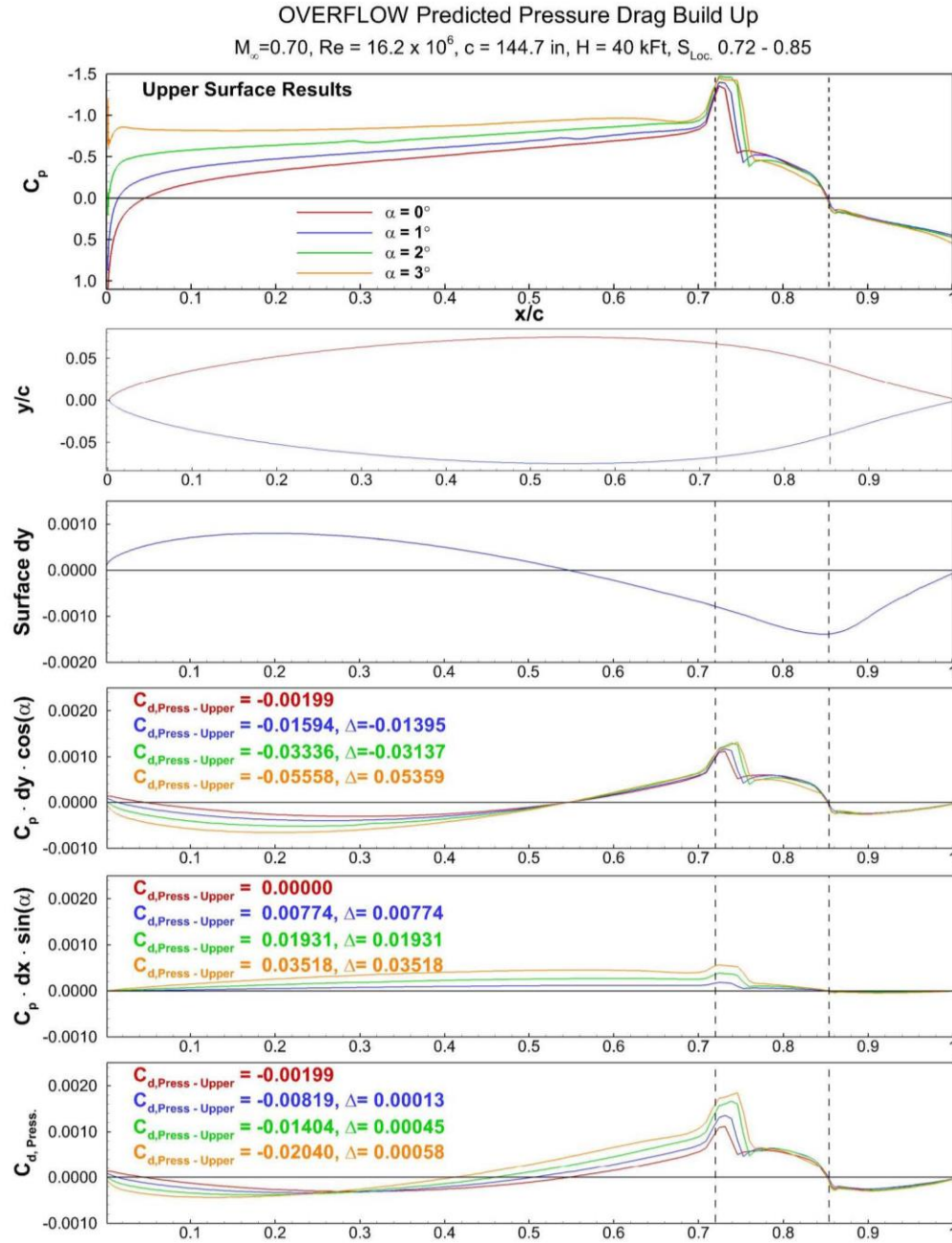


Figure 26: Effect of Angle-of-Attack on Pressure Drag Contribution – Upper Surface

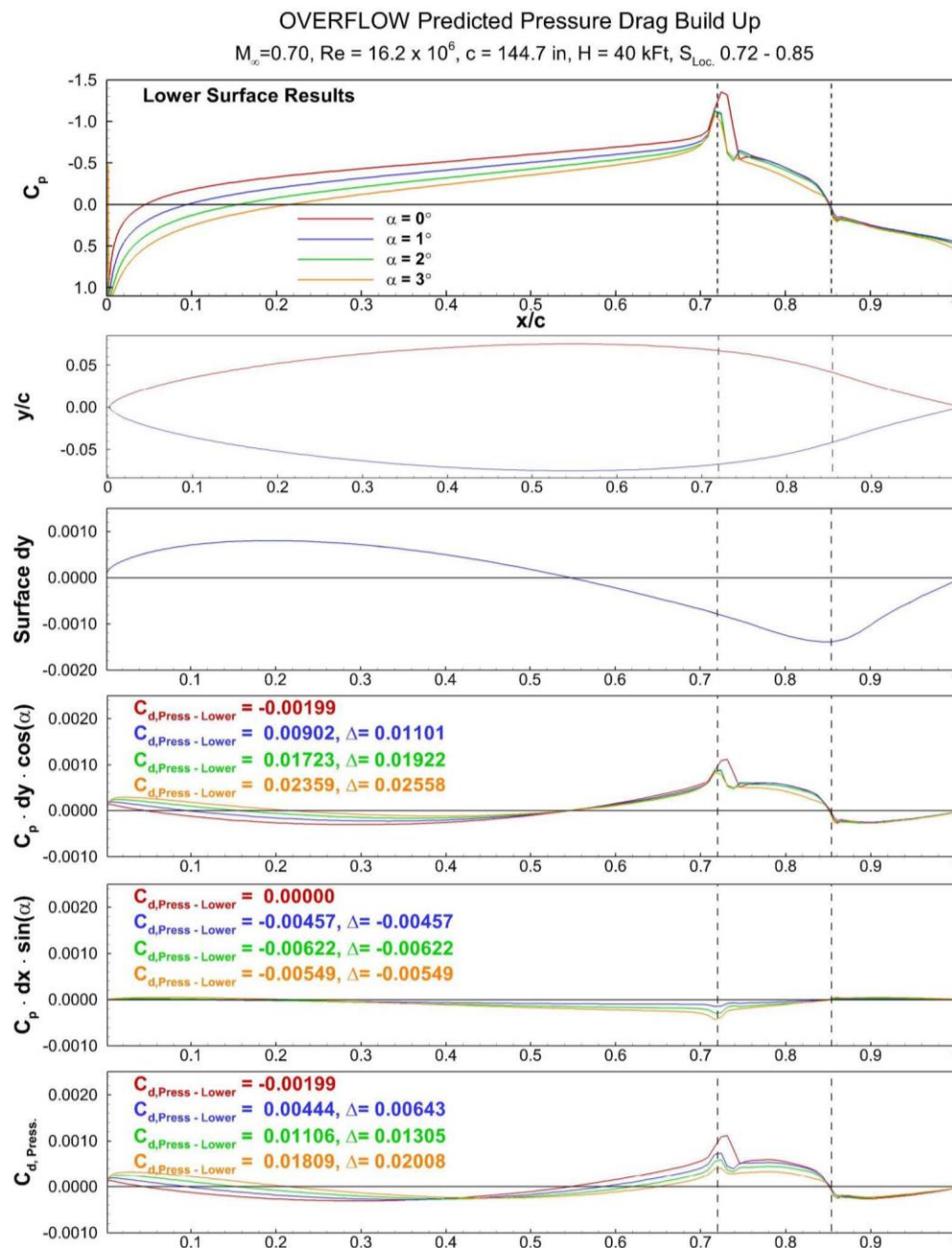


Figure 27: Effect of Angle-of-Attack on Pressure Drag Contribution – Lower Surface

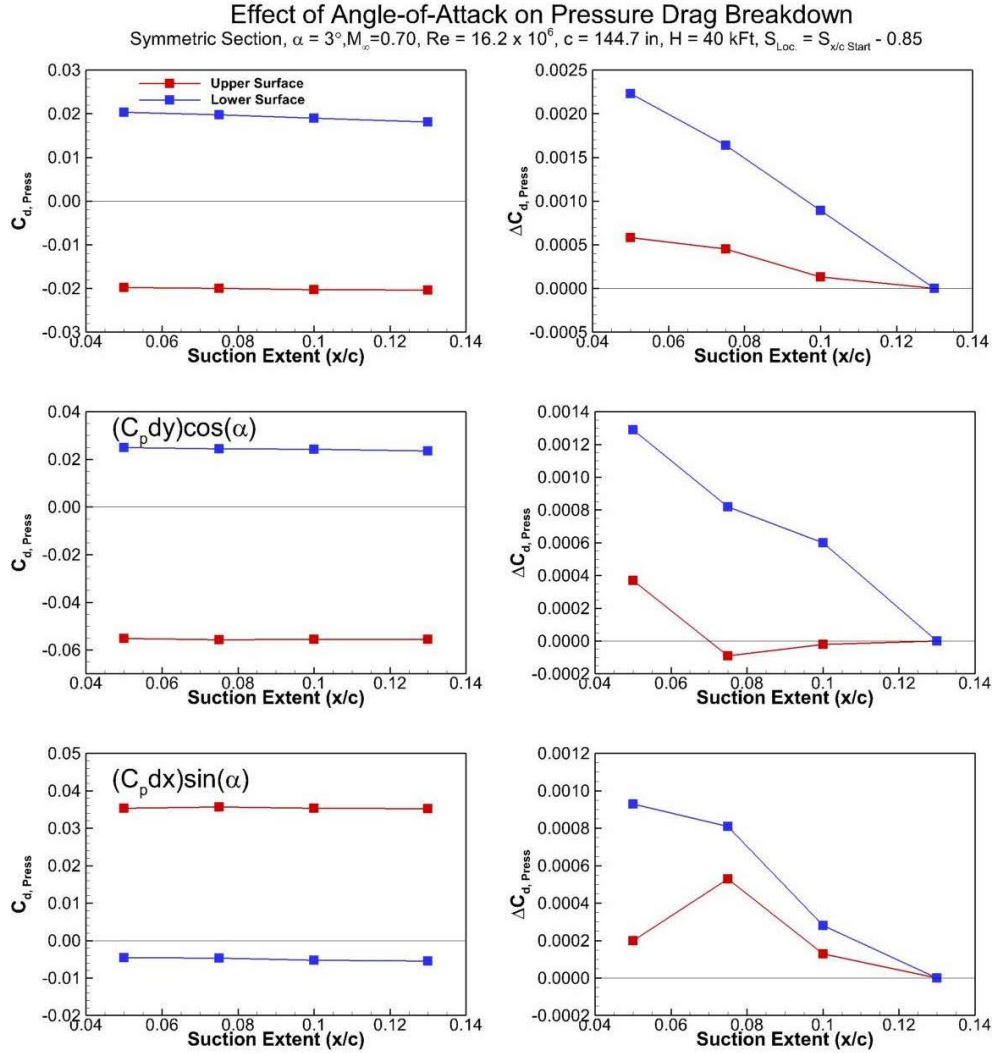


Figure 28: Effect of Suction Extent on Pressure Drag Breakdown

Figure 28 shows the effect of suction slot length on the pressure drag at  $\alpha=3^\circ$ . The suction slot length was varied from 5% to 13%, with each terminating at 85% chord. Overall, there was an almost linear relationship between slot length and pressure drag up until 13% where it reached zero. The effect of varying the slot length on the upper surface pressure distribution is shown in Figure 29, and the lower surface is shown in Figure 30.

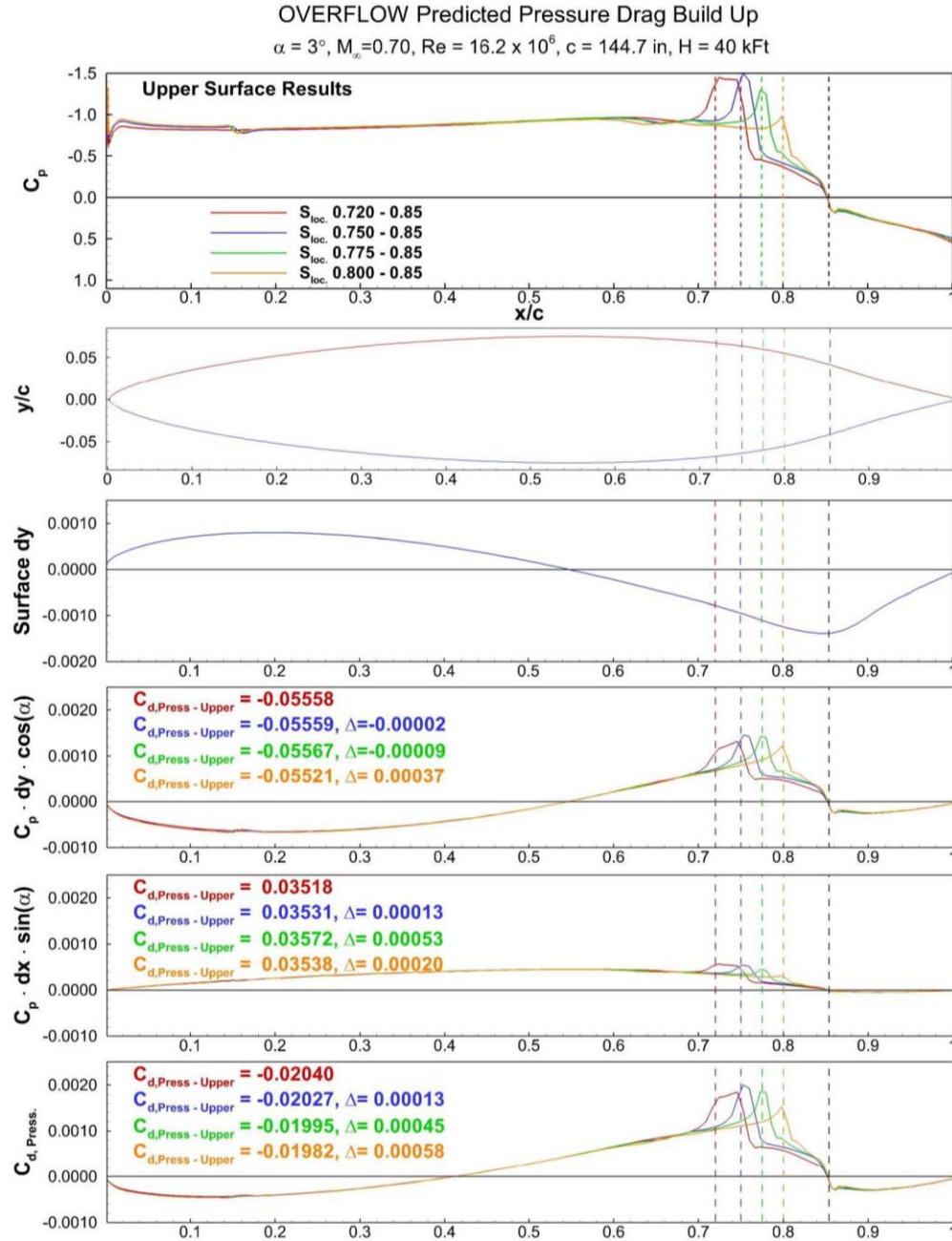


Figure 29: Effect of Suction Extent on Pressure Drag Contribution – Upper Surface

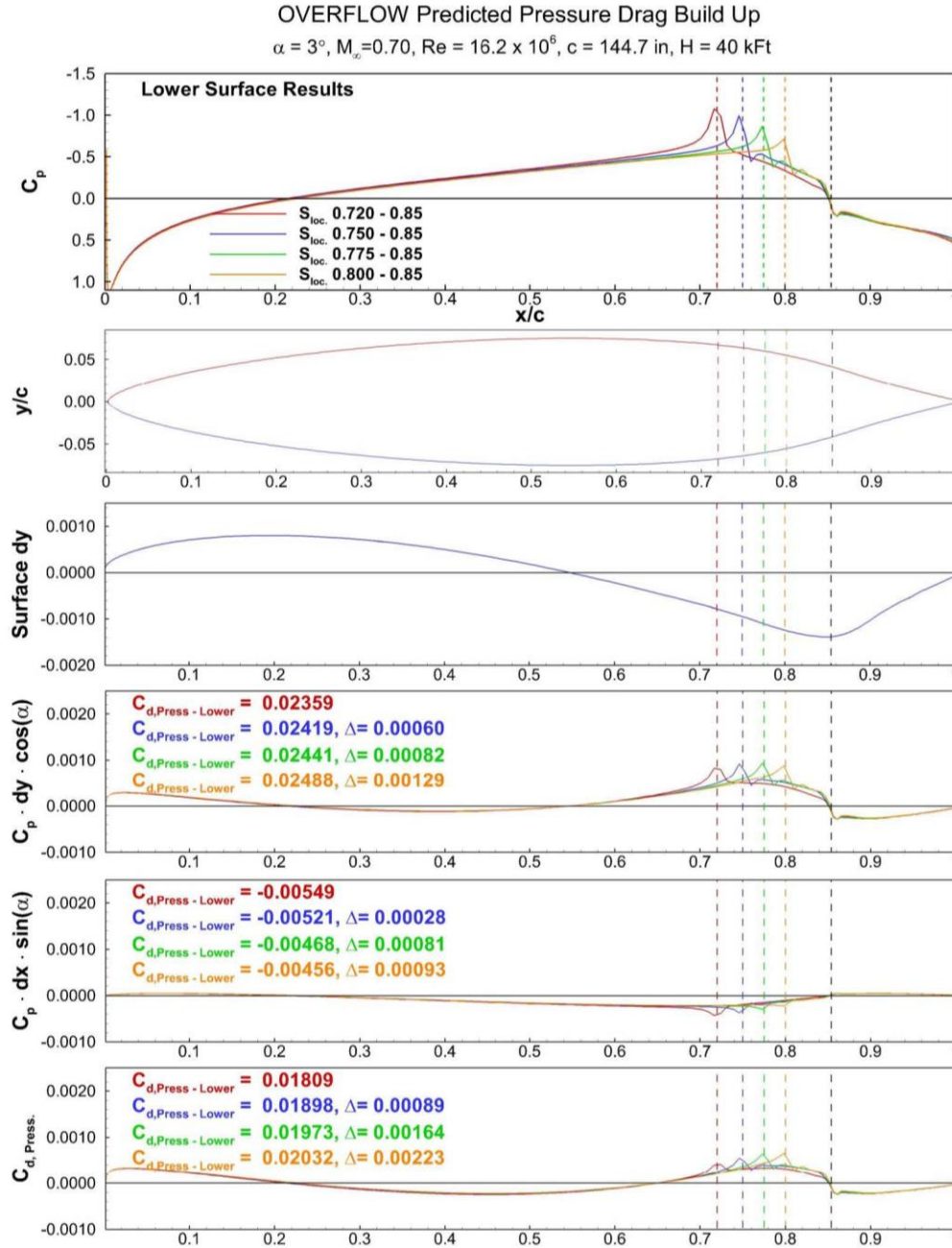


Figure 30: Effect of Suction Extent on Pressure Drag Contribution – Lower Surface

### 3.9 Final Airfoil Design

After numerous design iterations, an airfoil configuration was converged on that shows excellent potential. The final airfoil is 12.48% thick, and generates a  $C_l = 0.86$  for  $\alpha = 0^\circ$  at the SUGAR Refined flight conditions of  $M = 0.7$  and  $h = 40,000$  ft. The upper surface of the airfoil maintains laminar flow back to 57% chord, while the lower surface



transitions at 45%, as shown in Figure 31. The suction slot for this airfoil is located from 82.5% chord to 87.5%, with suction  $V_s/V_\infty = 6.5\%$  or a  $C_\mu = 0.00014$ . Figure 31 also compares the drag of the SUGAR Refined airfoil to the drag produced by the new airfoil section with suction, and with the fan exhaust ported out the trailing edge for wake filling. At the design  $C_l = 0.86$ , the SUGAR Refined airfoil has a  $C_d = 0.0137$ , while the Goldschmied section with suction has a  $C_d = 0.0052$  (62% reduction), which is then reduced to  $C_d = -0.0004$  (100% reduction) with the wake filling activated.

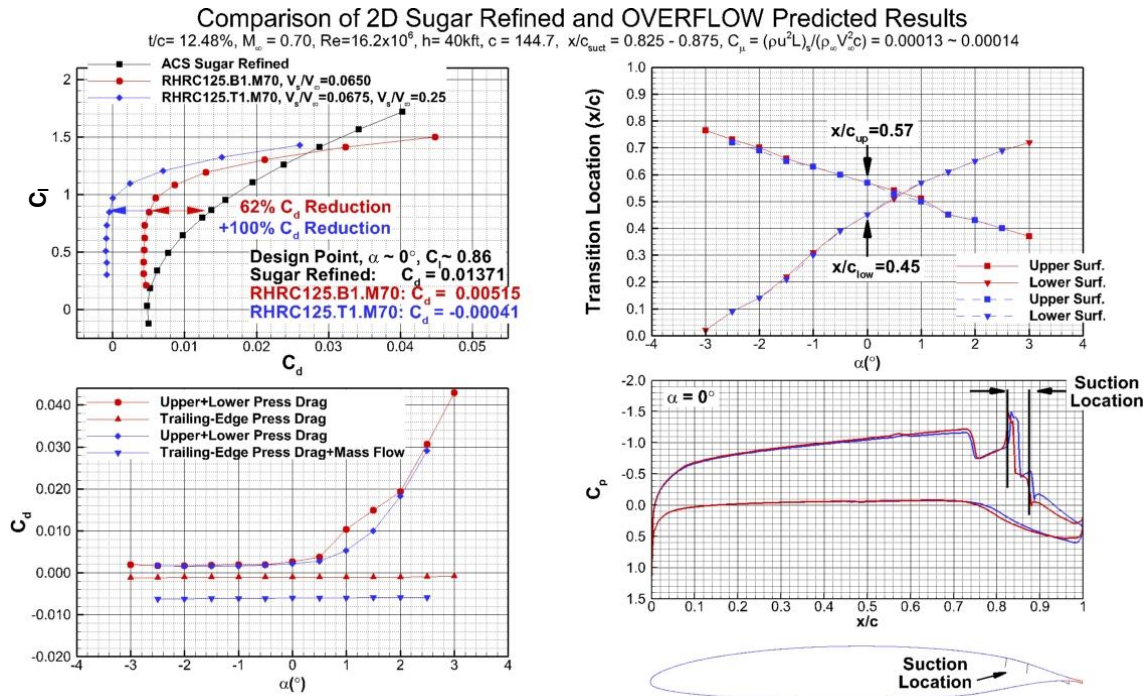


Figure 31: Final airfoil results compared to SUGAR Refined baseline

A more complete plot of the pressure distribution as a function of angle-of-attack is shown in Figure 32. The effect of varying the trailing edge blowing at  $\alpha=0^\circ$  is shown in Figure 33. Blowing from the trailing edge has a fairly large effect on the total  $C_l$  of the airfoil. To provide the best comparison,  $C_l$  should be held constant at the design value of 0.861, which has been done in Figure 34. Both of these figures show that as  $V_j/V_\infty$  is varied from 0 to 0.30, there is a large effect on  $C_d$ . Closer investigation reveals that most of the change in drag is produced through the pressure effect on the trailing edge itself. This observation is an intriguing result that could be further improved or optimized in subsequent studies. There is also a smaller contribution of the acceleration of the mass flow through the trailing edge in the jet.

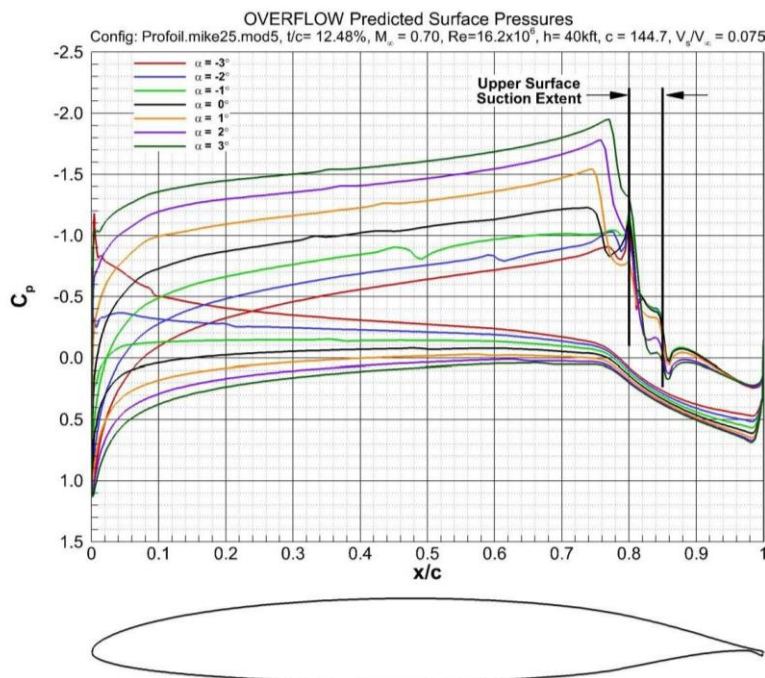


Figure 32: Predicted Surface Pressures

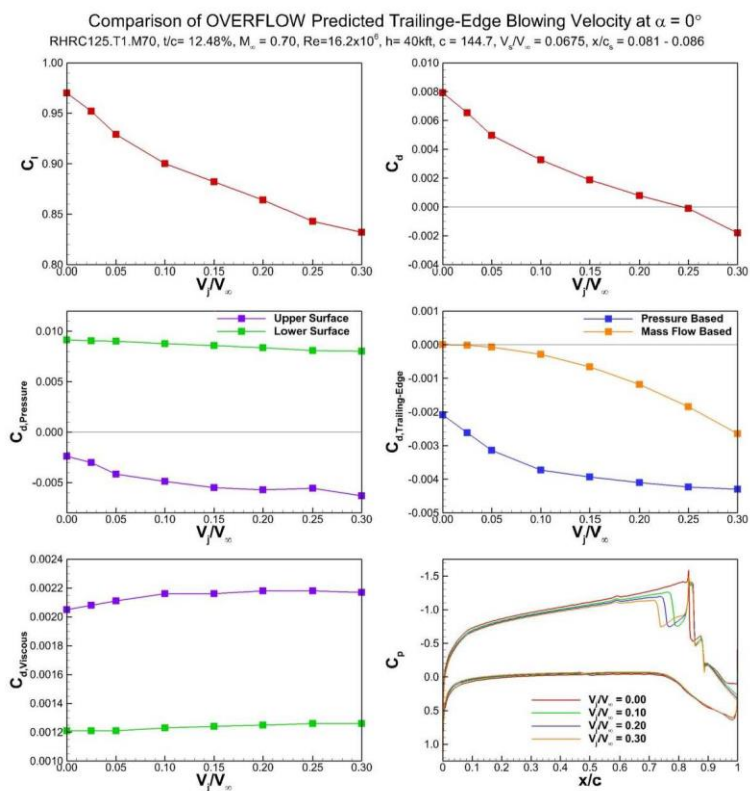


Figure 33: Effect of Trailing Edge Blowing at  $\alpha = 0^\circ$

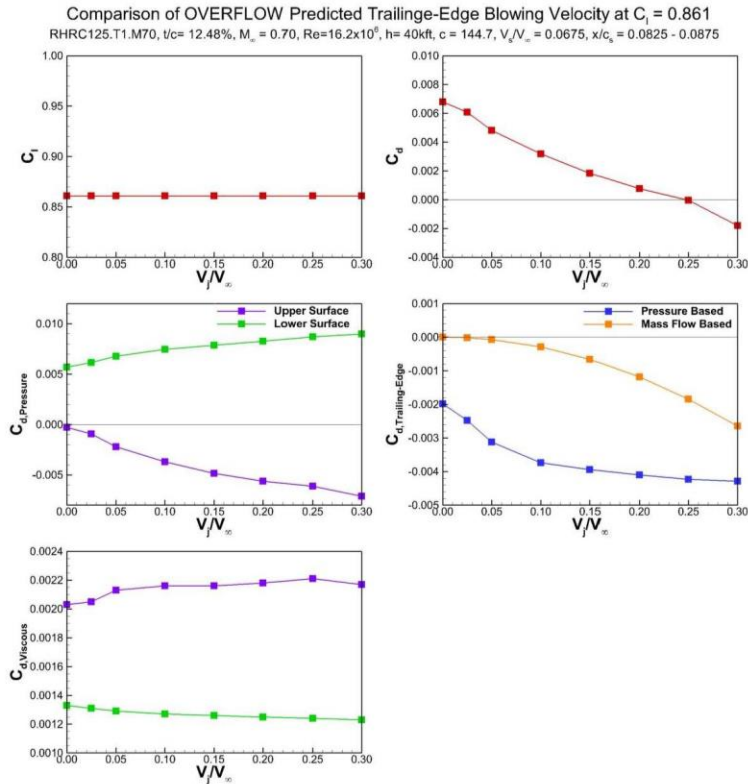


Figure 34: Effect of Trailing Edge Blowing at  $C_l=0.861$

Finally, the result of zero suction is shown in Figure 35. When suction is applied, the flow remains entirely attached. This results in Mach numbers and lower pressures over the upper surface of the airfoil. When suction is turned off, a large region of separation is seen aft of the suction slot, along with a clear breakdown of the designed suction profile and a decambering of the airfoil.

### Comparison of OVERFLOW Predicted Suction Effect

RHRC125.B1.M70,  $t/c=12.48\%$ ,  $\alpha = 0^\circ$ ,  $M_\infty=0.70$ ,  $Re=16.2 \times 10^5$ ,  $h = 40$  kft,  $c=144.7''$ ,  $V_g/V_\infty = 0.065$ ,  $x/c_s = 0.825-0.875$

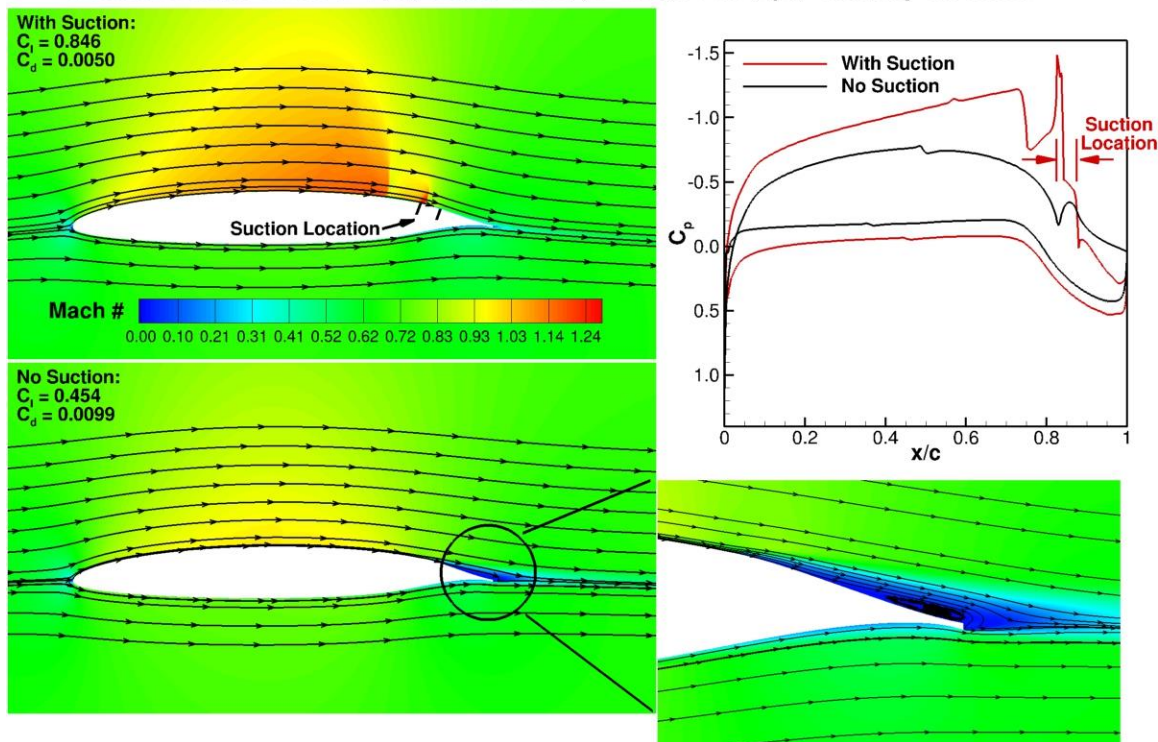


Figure 35: Prediction of Suction OFF Effect

## 4 Low-Speed Wind Tunnel Validation of Airfoil Design

### 4.1 Wind Tunnel Model Design

A wind tunnel model of the final transonic Goldschmied airfoil section was designed to be tested in the University of Illinois 3'x4' subsonic wind tunnel. Although an ideal validation of the design would have been conducted through a transonic wind-tunnel testing campaign, the budget of the Phase I program did not allow such a test to be conducted. However, such an effort would be a natural follow-on for a Phase II program.

The wind-tunnel model was designed with a stainless steel support structure to carry the loads of the airfoil, which consisted of two hollow spars and three ribs. The external airfoil shape was created with stereo-lithography plastic, which was secured to the spars with screws. The airfoil consisted of three main parts: an upper surface that wrapped around the leading edge to eliminate seams, a removable lower surface cover, and a trailing-edge section, as shown in Figure 36. The center section of the airfoil was hollow to allow the routing of pressure tubing. There were a total of 64 pressure taps on the airfoil surface. Two trailing edges were designed, one matching the plain trailing edge shape with suction on the upper surface, and a modified trailing edge with suction on the upper surface and blowing along the aft end. The internal routing of the pressure tap lines and blowing and suction paths are shown in the wireframe drawing in Figure 37.

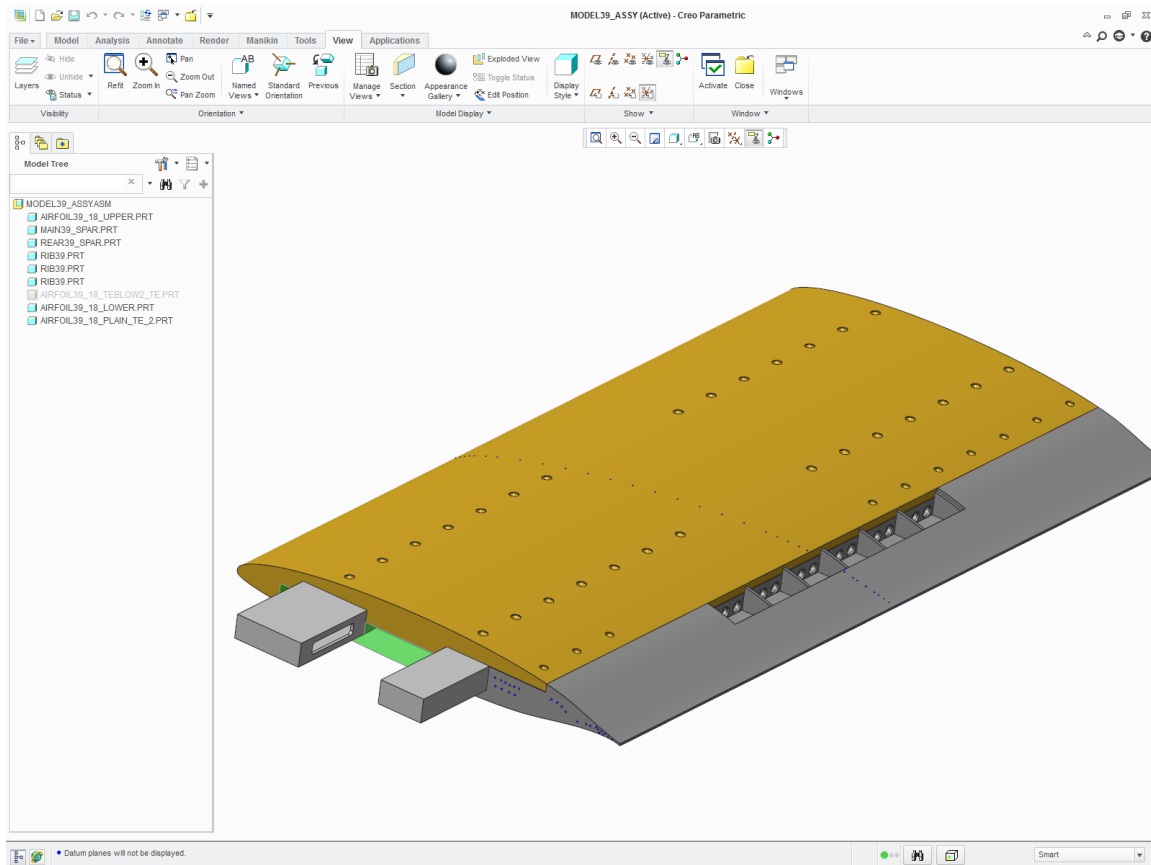


*Figure 36: External View of Assembled Model*



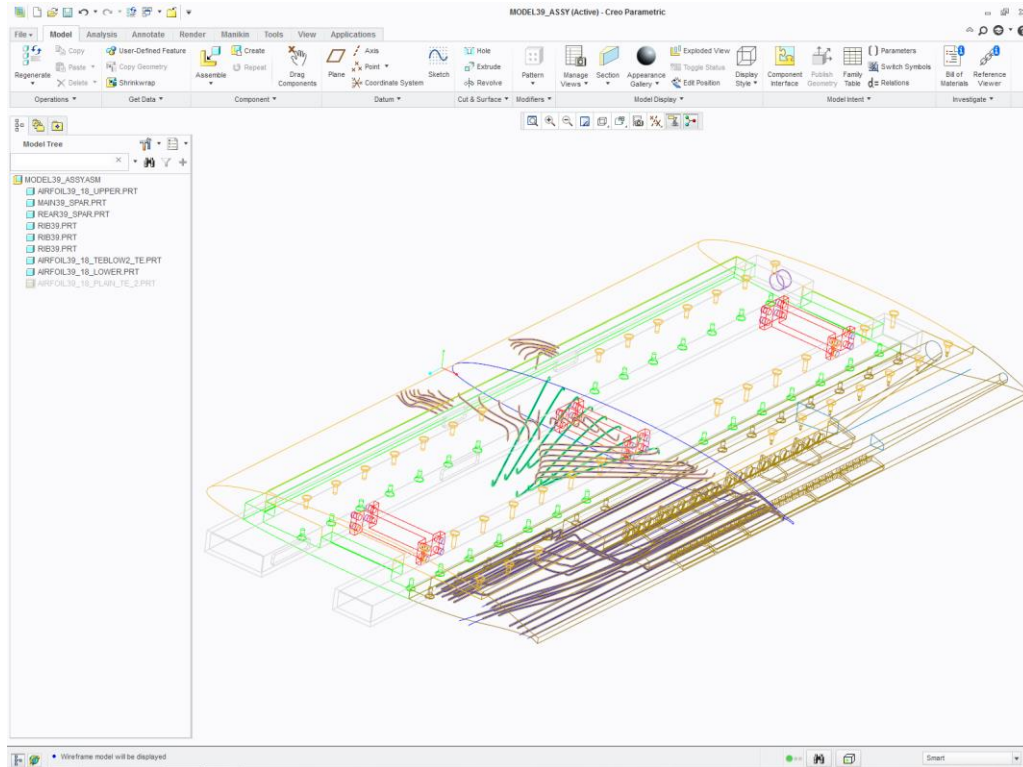


Figure 37: Wireframe View of Model Showing Internal Pressure Routing

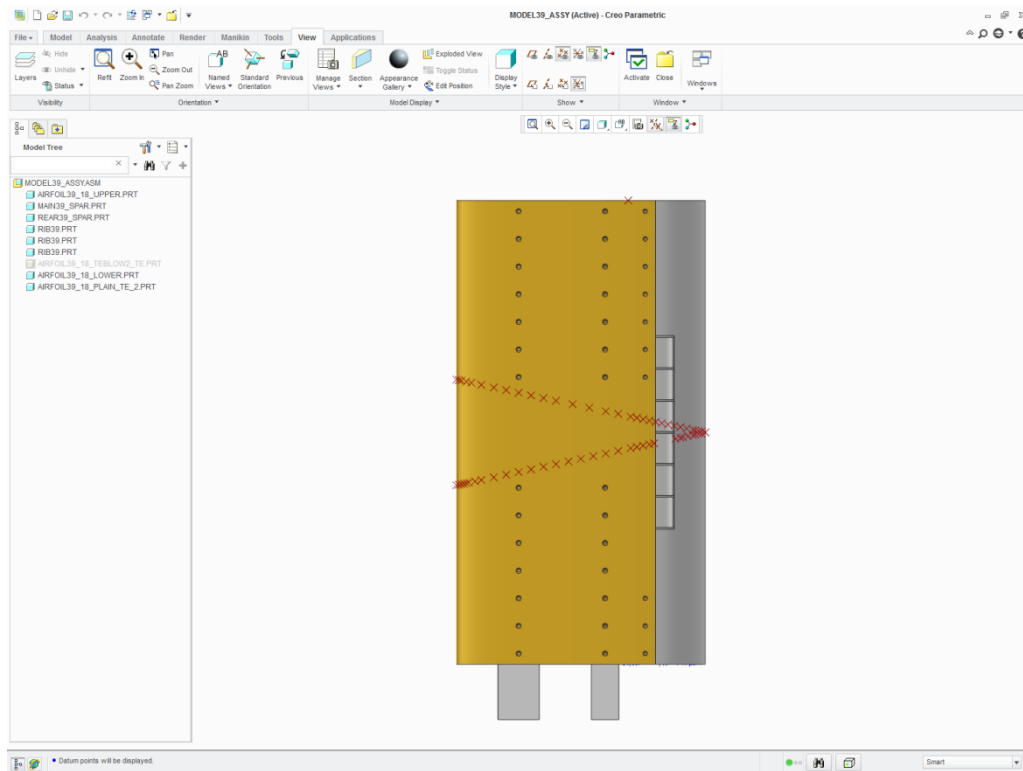


Figure 38: Inverted "V" Layout of Pressure Taps

An unusual surface pressure tap arrangement was used to ensure laminar flow across all pressure taps and the wake-survey plane, while also allowing the trailing pressure rake to be centered on the suction and blowing plenums. Figure 38 show the pressure taps are swept  $12^\circ$  to prevent taps upstream from transitioning the flow measured downstream. Unlike typical laminar flow models, the taps were arranged so they swept to a point at the trailing edge, instead of beginning a point on the leading edge and then sweeping in opposite directions on the upper and lower surfaces. This configuration allowed the momentum deficit rake behind the model to measure the undisturbed profile across the center-span region while being centered between the suction and blowing plenums.

External blowing and suction pressure sources were routed into six discrete plenums in an attempt to produce uniform suction and blowing patterns. In addition, each of the suction plenums was fed through 3 individual circular ducts into the suction manifold, which can be seen in Figure 39. The suction plenum ran from 80% chord to 87.5%, but vertical supports were provided so covers could be applied to the slot to reduce its size while providing support. Likewise, the blowing plenums exhausted through 5 discharge ducts shown in Figure 40. Unfortunately, the experimental results demonstrated that a more sophisticated design is necessary to provide even blowing patterns across the trailing edge.

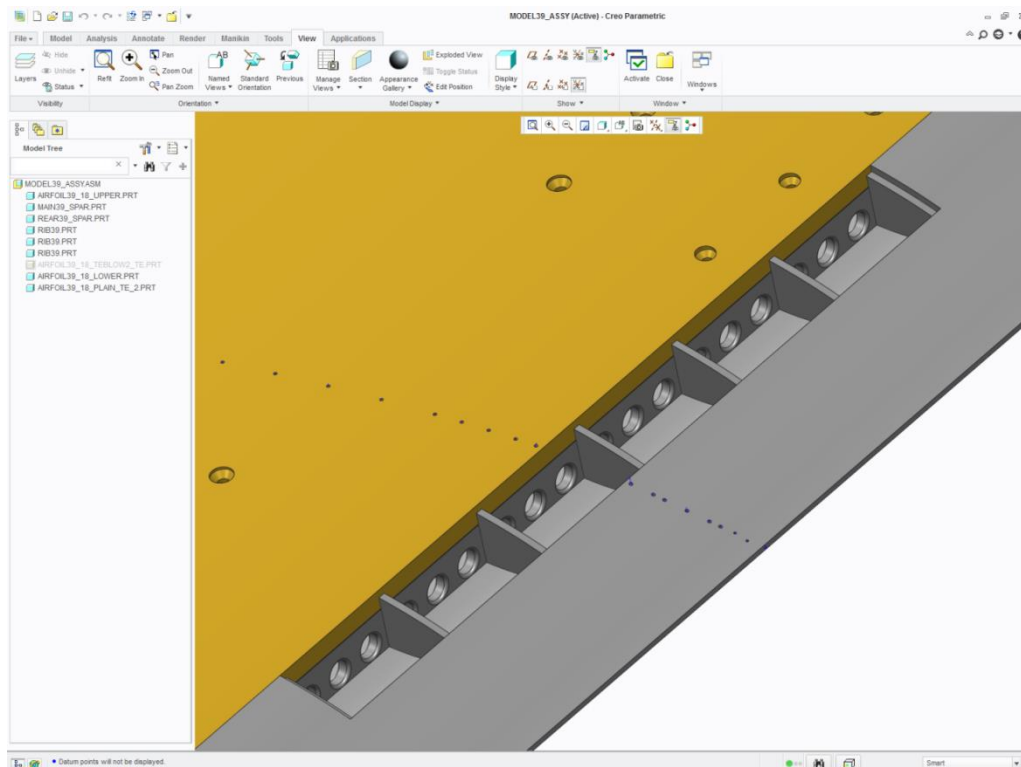


Figure 39: Plain Trailing Edge with Upper Surface Suction

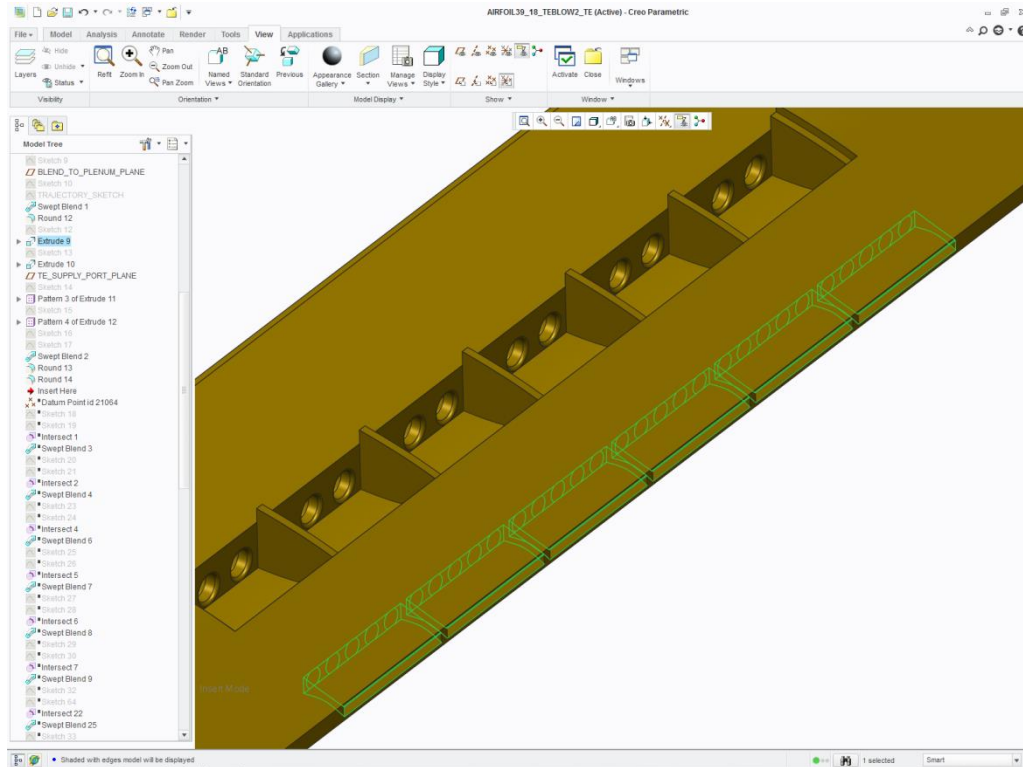


Figure 40: Blowing Trailing Edge

## 4.2 Wind Tunnel Test Approach

In order to validate the natural laminar flow qualities of the suction-enabled airfoil section, a series of experiments were performed on the designed airfoil in a low-turbulence, low-speed wind tunnel. While it is immediately apparent the free-stream Mach number at which these experiments were performed was well under the design Mach number for the airfoil, access to a large, transonic facility was limited during the initial Phase I study. However, the measurements acquired in the subsonic facility were still useful, as they reinforced the fidelity of the simulation environment in which the airfoil was designed and the general suction-enabled pressure recovery design methodology of the airfoil. The experiments were conducted in the Illinois 3-ft  $\times$  4-ft subsonic wind tunnel. Experiments were conducted on an 18-inch chord airfoil model, discussed in Section 4.1. In order to simplify the design of the subsonic wind tunnel model, the suction effects of the cross-flow fan system were simulated using a centrifugal blower system, which was connected to the suction plenum described previously. A photograph of the airfoil model installed in the wind tunnel is presented in Figure 41. All experiments were conducted at a chord-based Reynolds number of  $1.8 \times 10^6$ , and  $M_\infty = 0.18$ .

Due to the limited size of the experimental model, it was only possible to test the airfoil with boundary-layer suction across the upper surface. While experiments were attempted with the blower output attached to the blowing plenum, the pressure drop induced by

decreasing the flow area to interface with the blowing plenum was significant enough to damage the blower system. Since the blowing plenum was located farther downstream than the suction plenum, the small thickness of the trailing-edge region limited the port size which could be incorporated into the model design. Later attempts at providing an external blowing source also revealed a high degree of non-uniformity in the trailing-edge blowing produced. A significantly higher blowing was produced across the discharge duct at the root, farthest from the blowing source outside of the tunnel, with no perceivable blowing produced through the discharge duct at the tip, closest to the blowing source outside of the tunnel. As a result, no blowing component across the trailing edge was provided in these experimental results.

In future attempts at performing experiments on the suction/blowing airfoil configuration, it would be more beneficial to either utilize an actual cross-flow fan. If a simulation of the suction and blowing effects are still desired without the experimental complexity of running a cross-flow fan during testing, the blowing plenum should be able to be produced by routing multiple pressurized lines through the model to the individual ducts to produce a uniform blowing. Alternatively, a larger blowing plenum could also be manufactured into the main cavity of the airfoil, where the pressurization would have a greater volume to equalize. Such a configuration would also allow a blower output to be routed to a substantially larger plenum port on the side of the model, which would prevent the large pressure drop and off-design operation observed in the initial experiments performed during this study.



*Figure 41: Airfoil model mounted vertically in the Illinois 3-ft  $\times$  4-ft wind tunnel.*

Surface pressure measurements were acquired using an electronically-scanned pressure system, which was also used to compute the airfoil lift and quarter-chord pitching moment coefficients ( $C_l$  and  $C_m$ , respectively). Wake pressure measurements were acquired using a traversable wake rake situated 1.17 chord lengths downstream of the trailing edge of the airfoil model, which were used to calculate the drag coefficient  $C_d$  of the airfoil. Visualization of the airfoil surface flowfield was accomplished using a fluorescent oil surface flow visualization technique. Use of this technique allowed for the identification of key features in the time-averaged flowfield, including regions of separated flow and boundary-layer transition.

### 4.3 Experimental Results

The resulting performance produced by the airfoil is shown in Figure 42, which includes the performance predictions of the simulations at  $M_\infty = 0.70$  and  $M_\infty = 0.18$ , as well as the experimental measurements at  $M_\infty = 0.18$  with and without suction across the suction slot. From Figure 42, it can be observed that the airfoil performance exhibits a suitable agreement between the simulations conducted at  $M_\infty = 0.18$  and the experiments with



suction applied. Most importantly, excellent agreement is observed in the airfoil  $C_l$  and  $C_d$ , particularly near the subsonic design point at  $\alpha = 0$  deg and  $C_l = 0.485$ . While some discrepancy can be observed in  $C_m$  between the simulations and experiment, this difference is predominantly attributed to the limited number of pressure taps that could be outfitted on the airfoil model, particularly across the trailing-edge region.

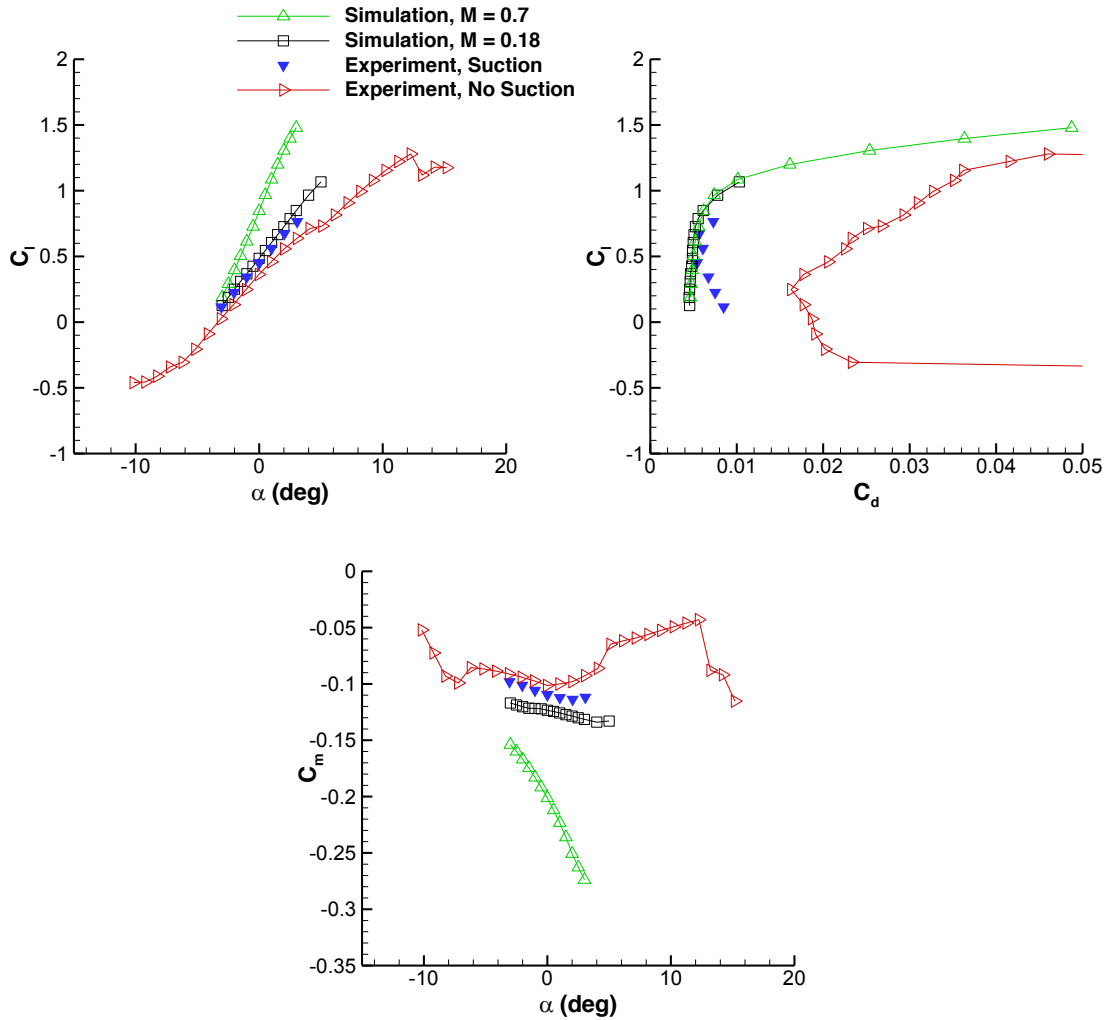


Figure 42: Performance of suction-enabled natural laminar flow transonic airfoil predicted from computational simulations at  $M_\infty = 0.7$  and  $M_\infty = 0.18$ , along with experimental measurements with and without suction.

A distinct difference in the airfoil lift-curve slope can also be observed between the simulation results at  $M_\infty = 0.7$  and  $M_\infty = 0.18$ . Such a difference is to be expected due to compressibility effects, representative of the Prandtl-Glauert compressibility correction. Comparing the experimental results provided with and without suction, it can be observed that removing the suction from the airfoil introduces a decrease in lift coefficient ( $\Delta C_l = 0.0881$ ) at the design angle of attack of  $\alpha = 0^\circ$ . While this decrease in lift is significant, it does not decrease the airfoil performance to an extent where an

aircraft utilizing this section would become inoperable with a failure of the suction system. There is also a far more substantial increase in drag with the removal of the suction system ( $\Delta C_d = 0.0152$ ), though it would be unlikely that this increase in drag would render the aircraft unsafe. Furthermore, the proposed use of the airfoil designed in the Phase I study is envisaged to be used across inboard sections of the wing, with traditional airfoil sections across outboard sections with aileron surfaces. This configuration would allow the roll control of the aircraft to be maintained in a failure of the suction system.

The comparison of the airfoil  $C_p$  distributions between the simulation results at  $M_\infty = 0.18$  and the experimental data is also provided in Figure 43. From Figure 43, excellent agreement between the simulations and experimental data is again exhibited. While the experimental data exhibits a slight offset in pressure relative to the simulations (on the order of  $\Delta C_p = 0.03\text{--}0.05$ ), these offsets are of little consequence, as the pressure differences between the upper and lower surfaces ( $C_{p,lower} - C_{p,upper}$ ) are highly consistent between the experiments and simulations. The change in  $C_p$  across the suction slot is also highly consistent between the experiments and simulations, indicating that the effect of the suction on the airfoil pressure distributions in the simulations is indeed being modeled effectively. It is also worth noting that the simulations were performed prior to obtaining any experimental data, and as such zero fine tuning of the computational grid or turbulence model was performed in response to the experimental measurements.

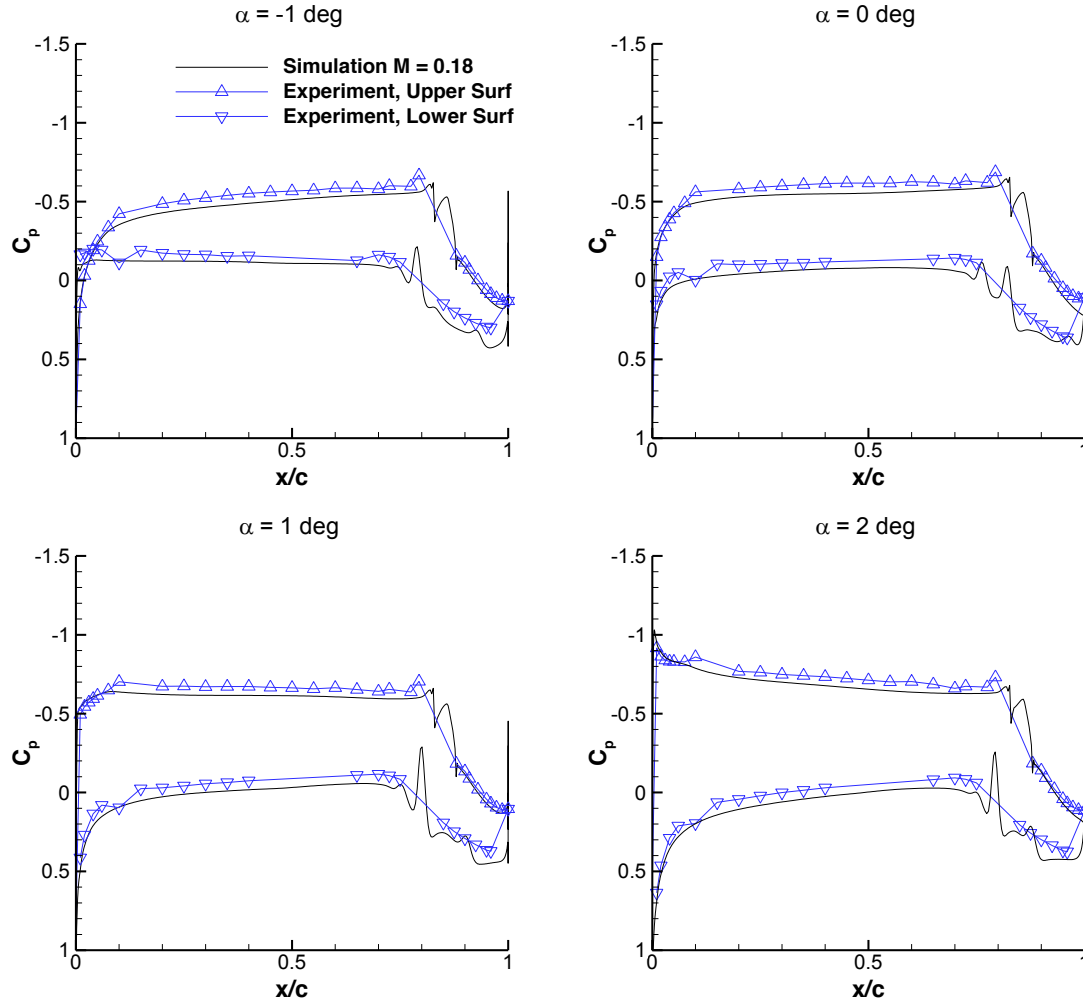


Figure 43: Airfoil  $C_p$  distributions predicted from computational simulations at  $M_\infty = 0.18$  and experimental measurements.

The results from performing surface-oil flow visualization on the airfoil model at the design angle-of-attack is shown in Figure 44. From Figure 44, the flow remains laminar across the entire airfoil upper surface until the suction slot. After the suction slot, the flow transitions, such that the aft 12.5% of the airfoil chord is turbulent. This observation from the surface-oil flow visualization is consistent with the simulations performed at  $M_\infty = 0.18$ . In these simulations, the Langtry-Menter transition model predicted a boundary-layer transition location at  $x/c = 0.825$  for the design case of  $\alpha = 0$  deg.

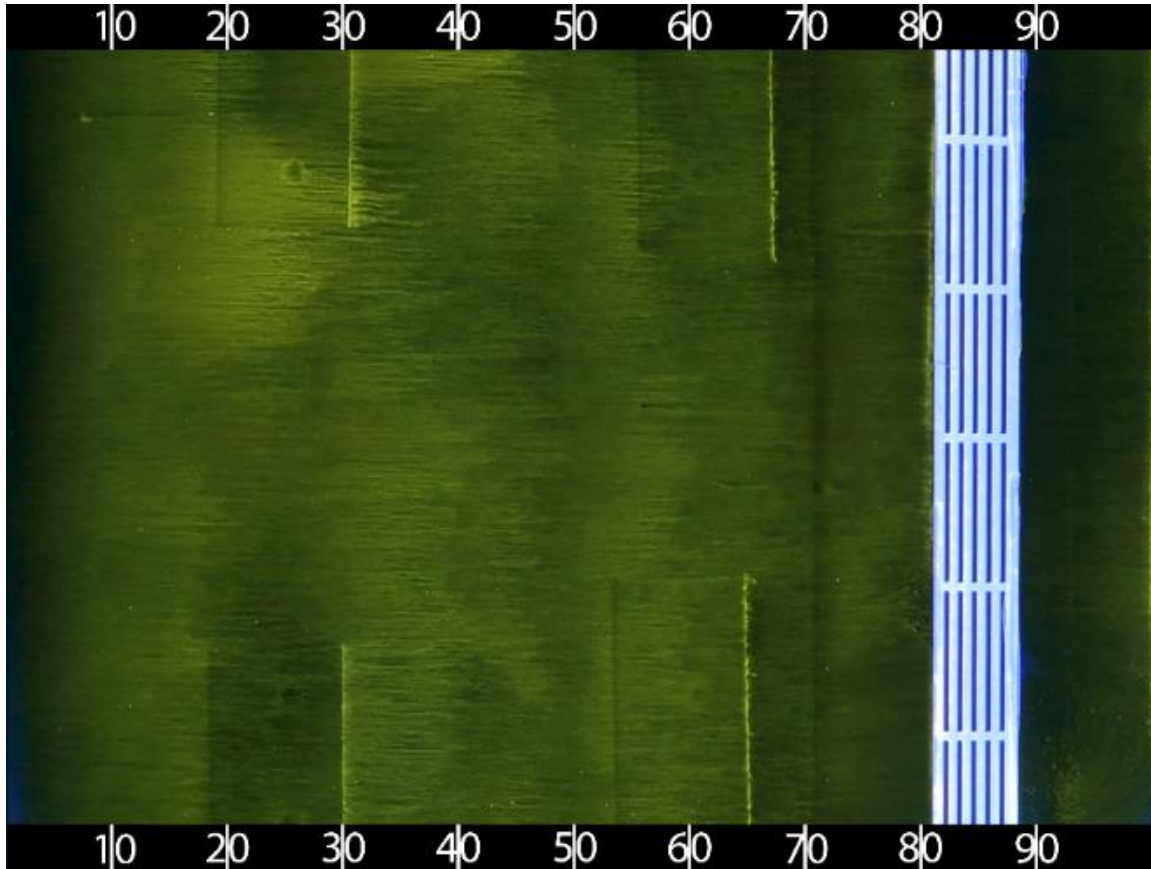


Figure 44: Surface-oil flow visualization of airfoil upper surface at  $\alpha = 0$  deg.

## 5 Experimental Cross-Flow Fan Testing and Development

The cross-flow fan (CFF) was selected for use in the transonic Griffith/Goldschmied airfoil because of its ability to provide high pressure differential flow in a distorted flowfield, while being energy efficient. A series of transonic experiments were undertaken to quantify the performance and efficiency of the CFF, and scale this for use in the energy balance study.

### 5.1 CFF Experimental Setup

Experimental testing of the cross-flow fan was performed at the University of Illinois in the 5"  $\times$  5" Large Rectangular Supersonic Tunnel (LRST) facility. The tunnel was originally configured with a converging-diverging nozzle designed for Mach 2 flow, driven by a compressed air tank farm pressurized to 150 psi. In order to utilize the tunnel for transonic flow, several modifications were made to the hardware setup. A new converging-only nozzle and a custom test section were machined out of 6061 aluminum. New tunnel side windows were also manufactured to allow for mounting of the cross-flow fan. The test section and stagnation chamber pressure taps were routed to two new 30 psi range high accuracy pressure transducers (Omega PX409-EH) to better

accommodate the transonic flow regime. An automatic gate valve was used to set the speed of the tunnel, controlled by a PID controller in LabVIEW. A schematic of the wind tunnel in its new configuration is shown below in Figure 45.

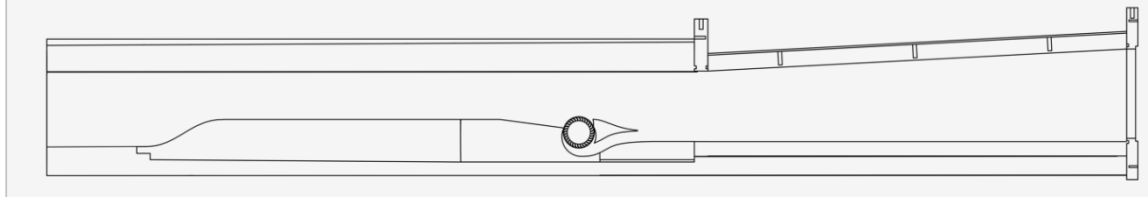


*Figure 45: Supersonic wind tunnel cross section*

An image of the fan selected for this study is shown in Figure 47. The fan was composed of a hard plastic material, and had 32 blades which were reinforced in the middle by a structural ring. The outer diameter of the fan was 3.42". The fan was cut to fit the 5" width of the test section, and aluminum end caps were attached to the ends of the fan to provide structural support. A steel shaft was force fit into each of the end caps to connect the fan to bearings embedded within each of the tunnel walls. The shaft on one side of the fan passed through the tunnel wall and was connected to the fan power drive with a flexible shaft coupling. The first component of the fan power drive was an Interface Force T4 rotary torque transducer which provided direct measurements of shaft torque and rpm, which is shown in Figure 48. The next component was a V-belt pulley system which was used to increase the rpm of the driving motor by a factor of 3.6.

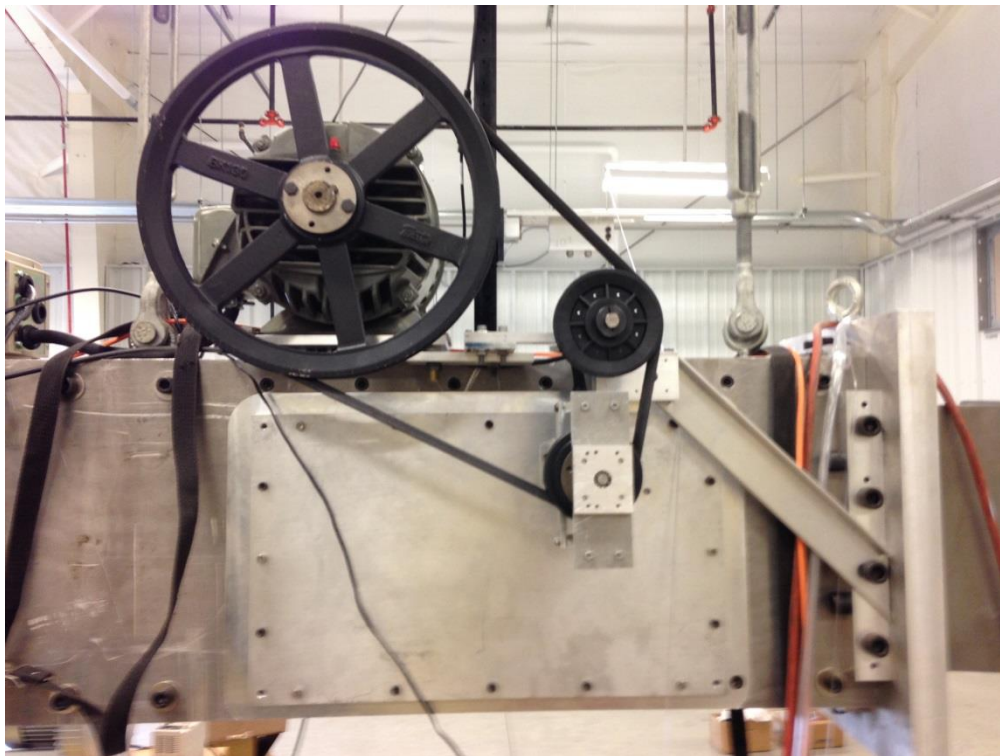


*Figure 46: Cross Flow Fan Drive Mechanism*



The motor which drove the system was a 3 HP 208 V 3-phase AC motor, and was mounted to the top of the wind tunnel, as shown in Figure 46. The speed of the motor was controlled by a standard 230V variable frequency drive. The maximum speed of the motor was about 5,000 rpm, leading to a maximum fan speed of about 15,000 rpm. Measures were taken to ensure that the driver, driven, and idler pulleys were all aptly supported to minimize vibrations and loss of power through the belt drive.



*Figure 47: CFF used in this study*

A detailed image of the fan and its housing in the tunnel is shown below in Figure 49. A diffusing ramp of  $7.5^\circ$  was incorporated into the tunnel wall leading up to the fan inlet arc to allow flow to enter the fan radially over the upstream region of the fan. The fan rear-wall housing was also built into the aluminum test section, leaving room under the fan to allow the flow to exit tangent to the blades. An expansion surface was manufactured using stereo-lithographic (SLA) 3D printing methods, functioning as the vortex wall for the fan. The expansion surface also simulated the trailing edge of the transonic Griffith/Goldschmied wing section, forming a duct for the flow exiting the fan.

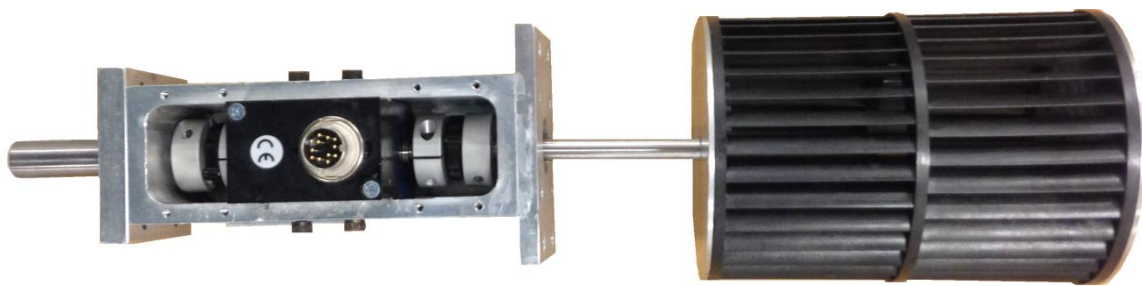


*Figure 48: Inline Torque Transducer*

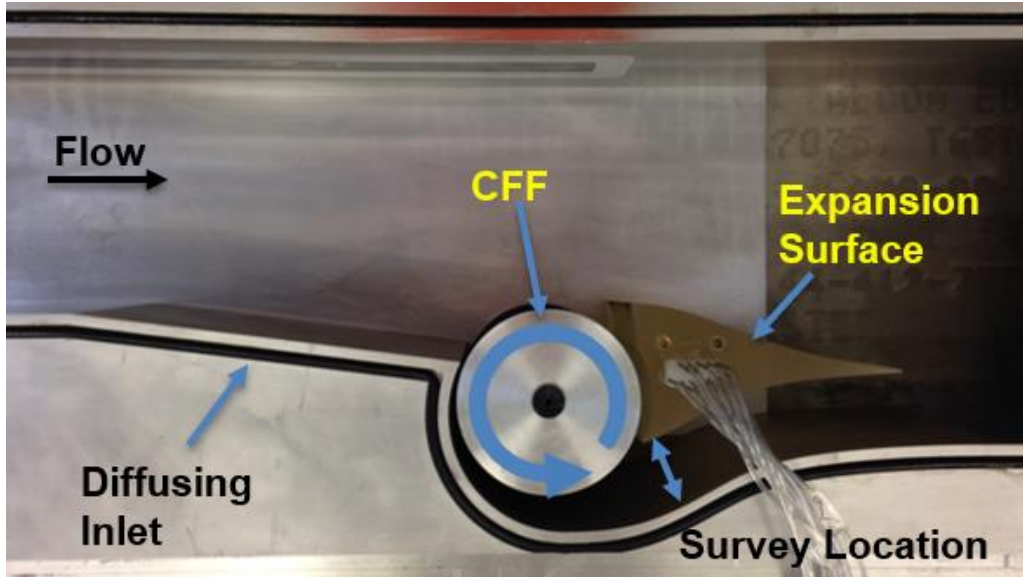


Figure 49: CFF housing and tunnel setup

The expansion surface was also equipped with 13 pressure taps distributed evenly across the upper and lower (inside the duct) surfaces to measure the pressure distributions over the surface for comparison between various fan rpm and free-stream Mach number cases. The pressure taps were routed to a Model 98RK Pressure Systems Net Scanner electronically-scanned pressure system which was connected to the data acquisition computer through an Ethernet connection. A diagram showing the location of these pressure taps is given below in Figure 50. A probe access hole was also located directly downstream of the fan in the exit duct to allow for surveys of total pressure, total temperature, and speed across the duct.

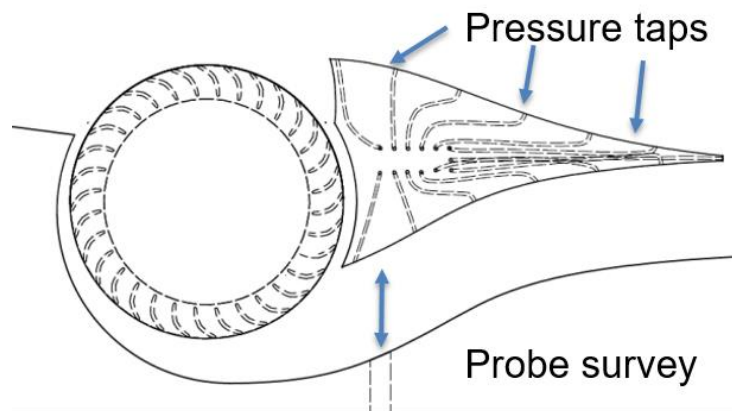


Figure 50: Pressure tap and probe survey location

In order to survey the total pressure, total temperature, and velocity within the inlet and outlet ducts, a Zaber T-LSR300A motorized linear slide was installed on top of the wind

tunnel in alignment with the probe access hole, shown above in Figure 50. For measurement of the total pressure within the duct, a custom made total pressure probe was mounted to the traverse and routed to the Net Scanner pressure system. During acquisition of the duct total temperatures, an Omega TJ36, J-type thermocouple was mounted to the traverse and routed to a National Instruments USB-TC01 Thermocouple measurement device. To take velocity measurements, a hotwire probe was attached to the traverse and used in conjunction with a TSI Incorporated IFA 100 System Intelligent Flow Analyzer. Standard correction methods were used to adjust the measured hotwire voltages due to changes in temperature during testing. The hotwire voltage measurements, as well as the measurements of the tunnel total and static pressure, total temperature, fan rpm and shaft torque were all acquired through a NI 9201 8-channel analog input module and recorded by LabVIEW software.

## 5.2 CFF Test Results

The transonic CFF performance was evaluated in this experiment through the collection of fan rpm and torque measurements, expansion surface pressure distributions, and surveys of the total pressure, total temperature, and speed in the fan exit duct. Data were collected at various free-stream Mach numbers ranging from 0.3 to 0.75, as well as at a variety of fan speeds ranging from 3,000 rpm to 8,000 rpm. These quantities can be used to evaluate fan efficacy in promoting attached flow over the expansion surface, determine the mass flow of the embedded suction/blowing system, as well as to compute various non-dimensional quantities which characterize the performance of the cross-flow fan. These quantities can also be used to scale the results of this experiment up to an actual aircraft scale. The results of this study are discussed below, and the utilization of these results is further presented in the aircraft performance section.

### 5.2.1 Expansion surface pressure measurements

The pressure distributions which were measured across the upper surface of the expansion surface (the side exposed to the free-stream flow) are shown in Figure 51 for several test conditions. Figure 51 (a) depicts the pressure distribution at  $M=0.6$  for the fan-off case as well as a 5,600 rpm case. Several observations can be noted from these distributions. First, the fan-off distribution of pressure across the surface indicates separated flow, while the fan-on case clearly indicates attached flow. This shows that the cross-flow fan is effective in assisting with pressure recovery over the simulated trailing edge in transonic conditions. Second, a distinct increase in pressure between the fan-off and fan-on cases is present, as indicated by the shift of the entire curve towards the positive  $C_p$  direction. Figure 51 (b) depicts the pressure distribution at  $M=0.5$  for rpm values of 0, 5,500, and 7,000. The same pressure recovery characteristics can be seen here as previously. In addition, it can be noted that increasing the fan rpm from 5,500 to 7,000 rpm did not drastically change the pressure distribution. This insensitivity of the pressure increase induced by the fan with increased rpm suggests that there is a saturation

effect of the pressure increase across the surface due to an increasing rotational rate of the fan.

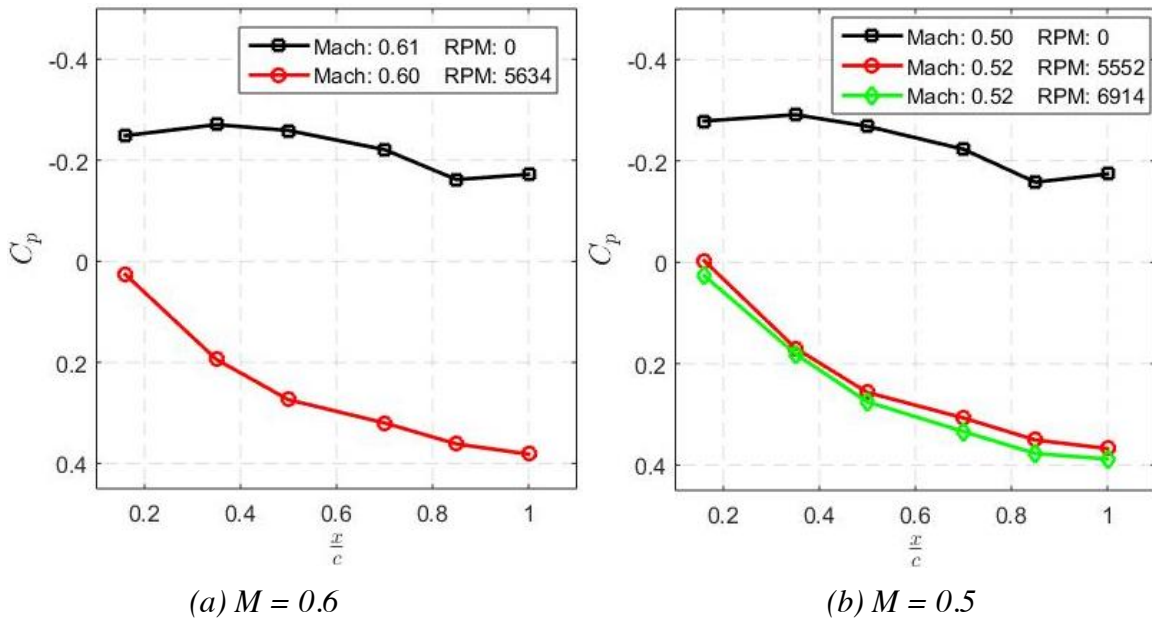


Figure 51: Expansion surface pressure distributions.

### 5.2.2 Duct surveys

Measurements of total pressure across the fan exit duct are shown below in Figure 52. Surveys for Mach numbers of 0.4 (a), 0.5 (b), and 0.6 (c) are shown for a variety of fan speeds. The average value of the total pressure in the duct is also shown as a vertical line on the plots. All averages were calculated using a standard integral averaging method. In both case (a) and (b) the total pressure in the duct can be seen to increase as the fan speed increases, indicating that the fan is performing work on the fluid to raise the total pressure. It can also be noted that the profiles indicate a region of higher total pressure towards the top of the exit duct. This observation holds true for each of the Mach number cases. As the Mach number of the free-stream flow increases, the region of higher total pressure is shifted right towards greater pressure values. Some of the abnormalities in the shapes of these profiles can be attributed to the fact that there is a high level of swirl to be expected in the exit duct, and the total pressure probe would not have been able to correctly capture the pressure. Due to the power supply limits of the motor, the fan rpm for the  $M=0.6$  case could not be increased beyond 5,600, and therefore a comparison between different rpm cases cannot be made.

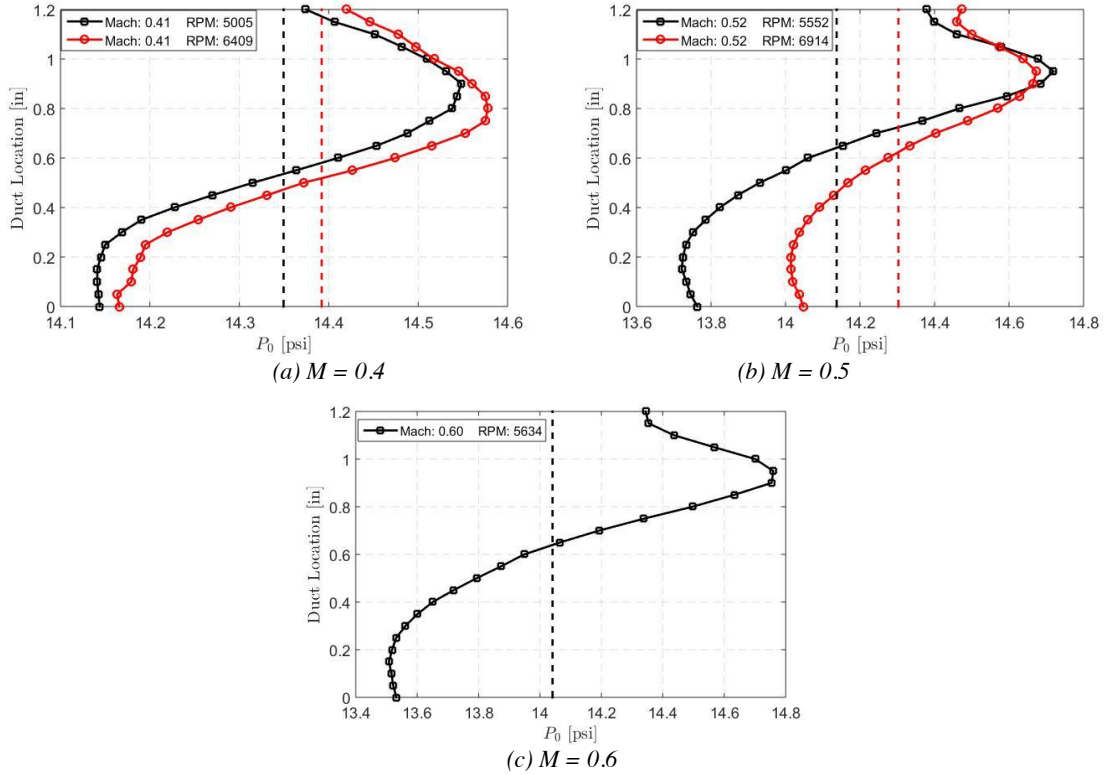


Figure 52: Duct total pressure distributions

The profiles of total temperature across the exit duct are given below in Figure 53. Again, cases are shown for  $M=0.4$  (a),  $M=0.5$  (b) and  $M=0.6$  (c). The total temperature profiles were much more constant across the duct than the total pressure profiles. A total temperature increase occurred in both cases (a) and (b) when the fan speed was increased. The shape of the temperature distribution remained relatively unchanged as the fan speed was increased, as well as when the free-stream Mach number was increased from 0.4 to 0.5. This is in contrast to the pressure distribution which became more skewed as the Mach number was increased. The shape of the temperature distribution is somewhat different for the  $M=0.6$  case, where the temperature was much higher towards the top of the duct than it was in the center.



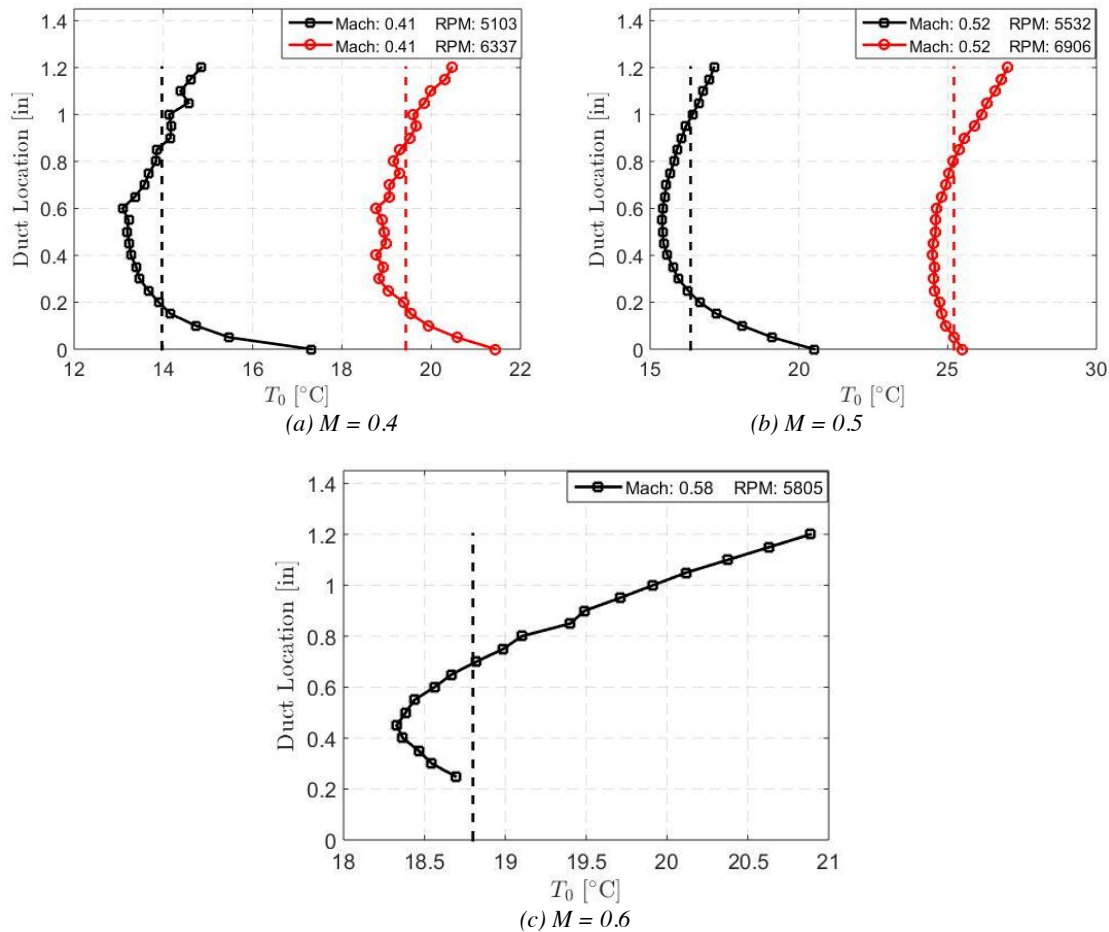


Figure 53: Duct total temperature distributions.

Velocity distributions for the same three Mach number and rpm cases are shown in Figure 54, (a)-(c). The average duct velocity increases with fan rpm as expected in both the  $M=0.4$  and  $M=0.5$  cases. The shape of the velocity profile also remains relatively unchanged as the fan rpm is increased, with a slightly greater increase in velocity towards the floor of the duct. A slight decrease in velocity towards the duct ceiling can also be seen for the  $M=0.5$  case as the fan rpm is increased. The shapes of the velocity profiles in the duct closely resemble the shape of the total pressure profiles, as would be expected. As the free-stream Mach number is increased, the upper half of the velocity profile is extended into regions of higher velocity. For the  $M=0.4$  case, the maximum duct velocity recorded was 220 ft/s. For the  $M=0.5$  case, the maximum velocity increased to 250 ft/s, and for the  $M=0.6$  case, the maximum velocity was 300 ft/s. The lower half of the velocity profile, however, remained relatively constant between the different free-stream Mach number cases.

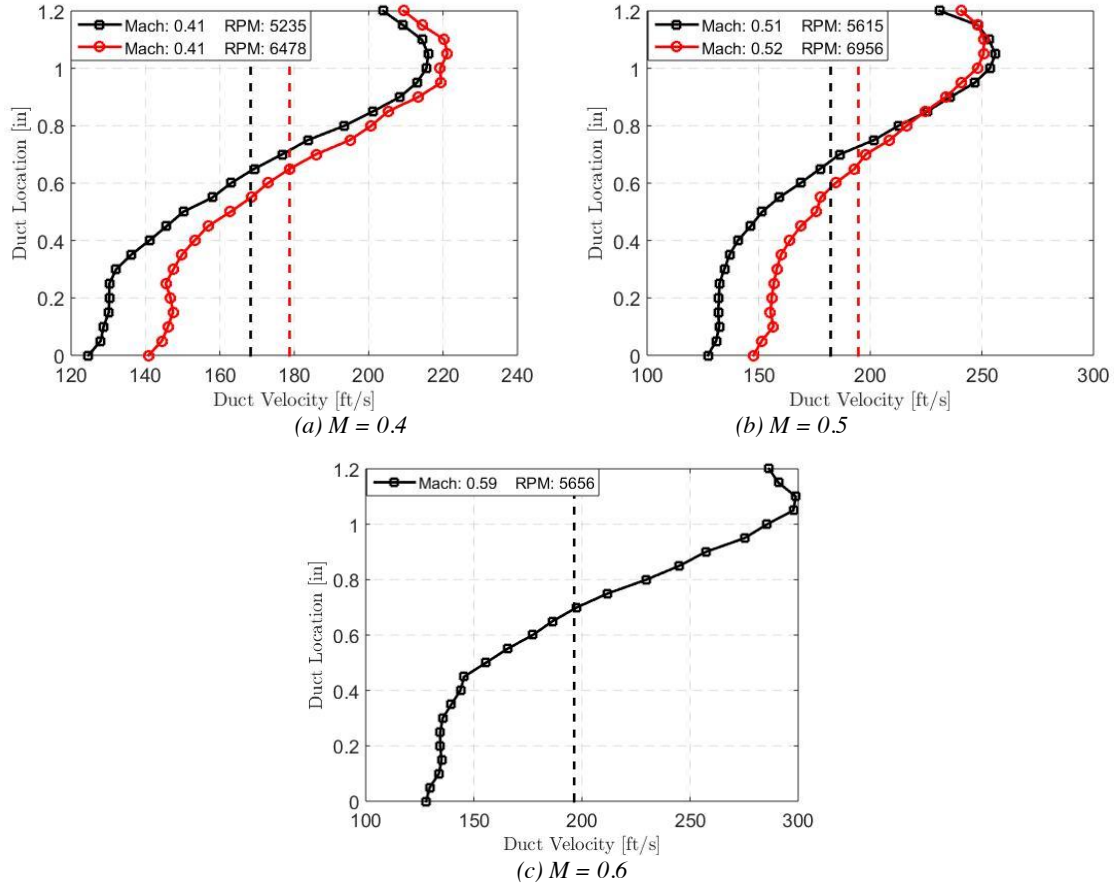


Figure 54: Duct velocity distributions.

The resulting averaged duct properties for each of the run cases mentioned above are presented in Table 2. The sixth column of the table contains the variable  $\frac{V}{V_\infty}$ , which is simply computed as the ratio of duct exit velocity to free-stream velocity. This parameter was used during the airfoil design phase to specify the quantity of suction/blowing required to attain proper airfoil performance. The final airfoil design required this ratio to attain a value of 0.25 across the blowing slot. All of the measured duct velocities surpassed this requirement, attaining velocity ratio values between 0.3 and 0.4 for all cases. It is also interesting to note that this ratio remained relatively constant between the different Mach number cases. The mass flow rate of the duct exit velocity was also computed for each of the test cases using the averaged duct data. Isentropic flow assumptions were used at a constant location in the duct in conjunction with static pressure measurements taken from the taps located inside of the exit duct to compute a duct Mach number and therefore mass flow rate. The results of this calculation are given below in Table 2.

Table 2: Duct Survey Results

Mach	rpm	$P_o$ [lb/ft <sup>2</sup> ]	$T_o$ [deg R]	V [ft/s]	$V/V_\infty$	$\dot{m}$ [slug/s]
0.41	5114.23	2066.33	516.81	168.27	0.38	0.0160
0.41	5993.73	2072.46	526.65	178.75	0.40	0.0157
0.52	5566.38	2035.77	521.13	182.26	0.33	0.0169
0.52	6925.31	2059.63	537.05	194.68	0.35	0.0177
0.59	5698.14	2021.91	525.51	196.41	0.31	0.0177

### 5.2.3 Fan power measurements

The mechanical power consumed by the fan during all operating conditions was calculated from the measured torque and rpm values collected by the torque transducer. A plot of power consumed vs. Mach number and fan rpm is shown in Figure 55. The power consumed by the fan can be seen to increase both as the free-stream Mach number increases and as the fan rpm increases. These data are also represented in Figure 56, where three lines of power vs. Mach numbers for a constant rpm are shown. The fan power increases linearly with Mach number for all three rpm cases, indicating a linear change in torque with changing Mach number at a fixed rpm. It can be noted that the slope of this line also increases as the fan rpm is increased. The 5,800 rpm case is of particular importance to this study, since power data was collected up to a free-stream Mach number of 0.75. The flight Mach number of the aircraft chosen for this study was 0.7, allowing the fan power data collected during the experiment to be scaled up to the full aircraft system. The methods and results of this power scaling are discussed in the following section.

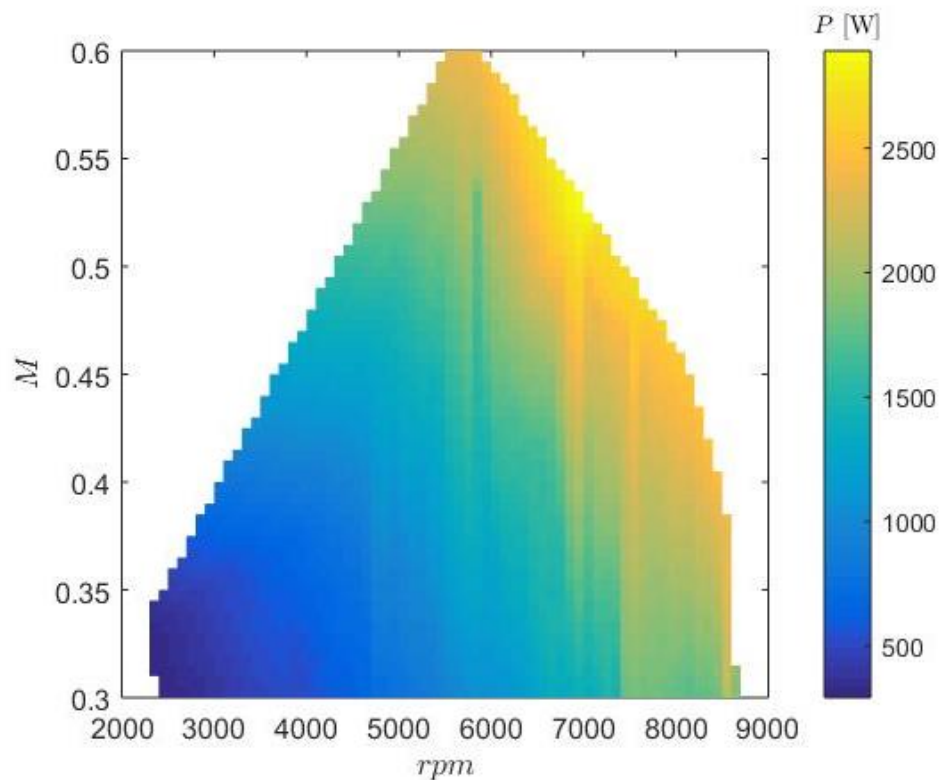


Figure 55: Fan power consumption as a function of  $M$  and rpm.

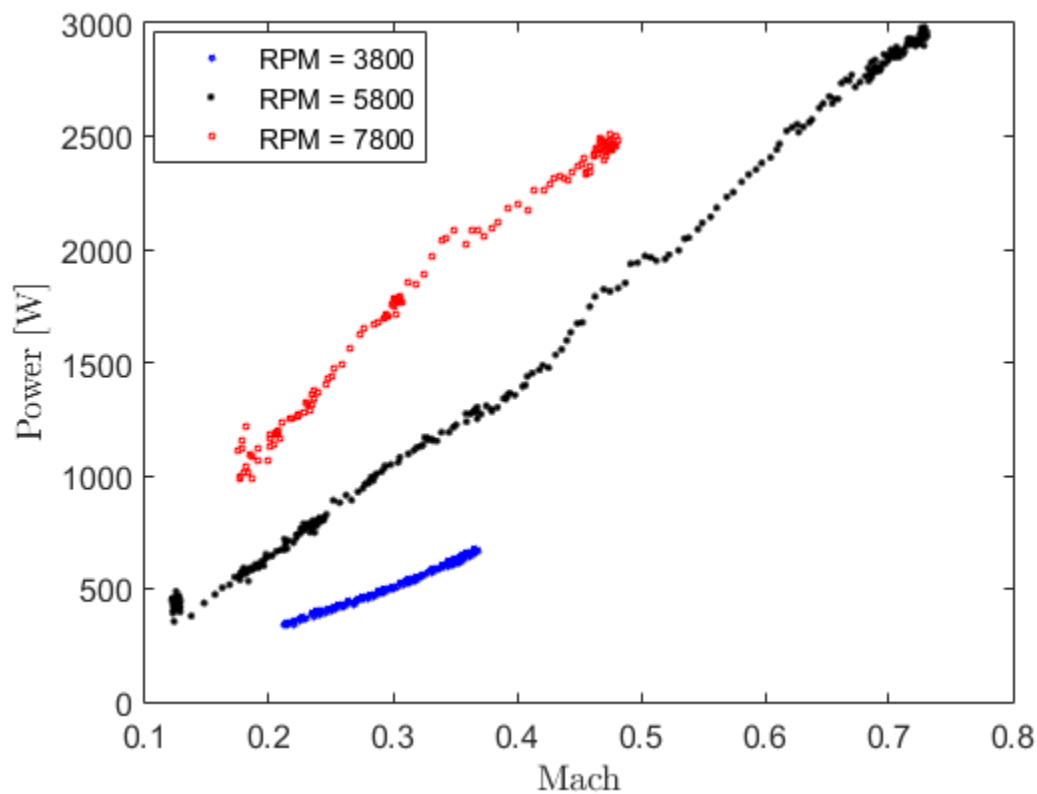


Figure 56: Fan power vs.  $M$  for various rpm.

### 5.2.3.1 Fan power scaling

In order to scale these experimental data to determine the power required to run a cross-flow fan that spanned the length of an actual aircraft wing, it was necessary to use several non-dimensional parameters. The first of these parameters was the flow coefficient,  $\phi$ , defined as:

$$\phi = \frac{V_{\infty}}{\omega D_o}$$

where  $\omega$  is the angular velocity of the fan and  $D_o$  is the diameter of the fan. This coefficient represents the ratio of the free-stream velocity to twice the fan tip speed. Previous work by Dygert and Dang<sup>34</sup> suggests that this parameter can be used to dynamically scale fan data between two different flight conditions. This parameter was calculated for the fan test cases, and results are given in Table 3. The aircraft fan tip speed which would be required to produce the same amount of suction/blowing was then computed by matching flow coefficients between the two cases and solving for  $U_{o,aircraft}$ , the aircraft fan tip speed. This calculation led to the necessity of a reduced tip speed for the aircraft conditions compared to what was produced in the wind tunnel environment. The flow coefficients shown in Table 3 were calculated from test conditions at  $M = 0.6$ , the highest Mach number for which an entire fan data set exists.

Table 3: Fan flow coefficient for test conditions

	Experimental	Aircraft Scale
$\phi_{\text{suction}}$	0.7985	0.7985
$\phi_{\text{blowing}}$	0.7983	0.7983
$U_o$ [ft/s]	85.395	76.8

The second non-dimensional parameter was the power coefficient,  $\lambda$ , defined by Dang as:

$$\lambda = \frac{W_s}{\frac{1}{2}\rho D_o U_o^3 b}$$

where  $W_s$  is the fan shaft work (or power),  $\rho$  is the free-stream density,  $D_o$  is the fan diameter,  $U_o$  is the fan tip speed, and  $b$  is the span of the fan. Data from the wind tunnel tests were used to compute this power coefficient at a Mach number of 0.7.

It was then assumed that when implementing the cross-flow fan on the Sugar Refined aircraft the power coefficient would remain constant across the portion of the span containing the cross-flow fan. For a first estimate of the power required by the CFF wing, a constant tip speed was also assumed. Although this assumption would be difficult to realize on a physical aircraft due to the change in diameter of the cross-flow fan across the wing span. However, a representative constant tip speed could be approximated by breaking the fan up into several sections which each ran at the same tip speed. Therefore, this assumption holds for a first estimate of the power required by the cross-flow fan system. Using the power coefficient calculated from the experimental data in conjunction with the flight conditions and Sugar Refined wing geometry, an



estimate of the total power required to run cross-flow fans in both wings was calculated according to the following integral:

$$P = 2 \int_0^{b/2} \frac{W_s}{b} dy$$

where

$$\frac{W_s}{b} = \frac{1}{2} \rho D_o U_o^3 \lambda$$

and b is the length of the portion of the span covered by the cross-flow fan.

The quantities which were used to compute the power coefficient as well as evaluate the power integral are given below in Table 4. The flight conditions and scaled power values are given in Table 5. These results indicate that the fan system would consume **187 kW** of power when operating on an aircraft cruising at altitude with a speed of  $M = 0.7$ .

These power scaling results have been utilized in conjunction with a simulation of the Sugar Refined aircraft with the transonic Griffith/Goldschmied airfoil and cross-flow fan system incorporated into the wing. The simulation has been used to quantify the fuel savings which could be gained if such a system were incorporated into a transport aircraft.

*Table 4: Pre-scaled test data*

$W_s$ [W]	2880.8
b [in]	5
$\rho$ [slug/ft <sup>3</sup> ]	0.0021364
$D_o$ [in]	3.457
$U_o$ [ft/s]	85.395
$\lambda$	26.61
M	0.7014
RPM	5661.3

*Table 5: Scaled power data*

P [kW]	187.58
b/2 [ft]	42.4
$\rho$ [slug/ft <sup>3</sup> ]	0.0005428
$D_{o,root}$ [in]	11.28
$D_{o,tip}$ [in]	4.94
$U_o$ [ft/s]	76.8
M	0.7

## 6 **Systems and Energy Balance**

As discussed in the previous section, one of the key goals of the Phase I study was to understand and predict the effects of integrating the Griffith/Goldschmied section concept into a baseline aircraft for a typical mission. This allowed for a systems-level analysis of the performance of the concept. The approach taken was via the use of an interdisciplinary aircraft synthesis tool, AVID ACS.<sup>35</sup> AVID ACS was derived from the NASA ACSYNT code developed in the 1960s/70s. The ACSYNT tool is widely used in industry for aircraft conceptual design studies (e.g. Boeing B-ACS<sup>36</sup>). For the Phase I study, ACSYNT was used to perform sensitivity analysis and trade studies against an established baseline aircraft configuration. Therefore, the first task was to set and match the parameters for a baseline aircraft configuration. Once a baseline aircraft configuration was created, sensitivity studies on the aerodynamics, propulsion, and structures/weights of the configuration is carried out to determine the concept's effects for a specific mission.

### 6.1 **Aircraft Baseline Matching**

The Boeing N+4 SUGAR Refined (765-094-TS1)<sup>10</sup> configuration was chosen as the baseline aircraft to perform comparisons against. The N+4 SUGAR Refined (765-094-TS1) configuration is the baseline configuration for the SUGAR Phase II trade studies.<sup>10</sup> Based on the Boeing 737, the N+4 SUGAR Refined is a span-constrained, low wing aircraft equipped with a single aisle and circular cross section fuselage configuration. It has two wing mounted turbofan engines (gFan++ Advanced Turbofan Engine) and was designed to hold 154 passengers in a dual-class configuration. A three-view drawing of the 765-094-TS1 is shown in Figure 57.

The approach of matching the N+4 SUGAR Refined is outlined in detail in the following sections. Briefly, in order, the parameters of the aircraft geometry, mission trajectory, aerodynamics, propulsion and finally weights were matched in ACS to the details provided in the SUGAR Phase I and Phase II Reports.<sup>19,20</sup>

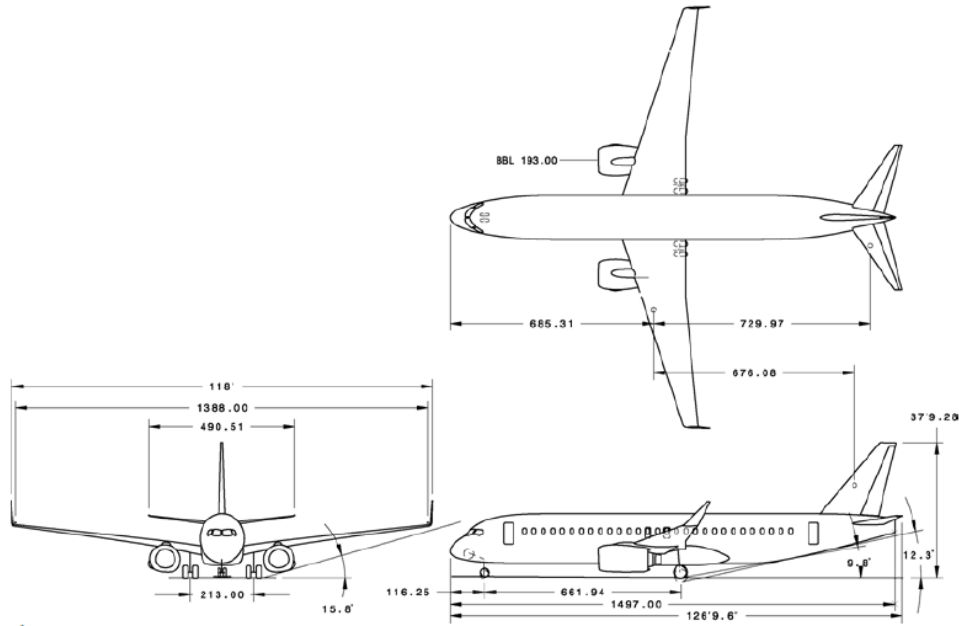


Figure 57: Boeing SUGAR Refined (765-094-TS1) 3-view drawing.<sup>20</sup>

### 6.1.1 Geometry

The first step in the aircraft matching process was to ensure that all the known geometric details were applied in the ACS input file geometry section. This information was also augmented with any known geometric information for a Boeing 737-800. A list of the matched geometric parameters is shown below Table 6 and Table 7 for the wing, horizontal tail, vertical tail, and fuselage.

Table 6: 764-095-TS1 Wing and Empennage Parameters.

Parameter	Wing	H-Tail	V-Tail
Sref (ft <sup>2</sup> )	1285.9	265.9	213.4
Sweep (deg)	15.08	30.0	33.2
Taper Ratio	0.159	0.202	0.271
Root t/c	0.1248	0.1	0.1
Tip t/c	0.1248	0.1	0.1
Dihedral (deg)	6.0	-	-
AR	11.636	6.237	1.94

Table 7: 764-095-TS1 Fuselage Parameters.

Parameter	Wing
Body Length (ft)	124.75
Max Diameter (ft)	13.16
Nose Fineness Ratio	0.159
Afterbody Fineness Ratio	3.5

### 6.1.2 Mission Trajectory

The mission chosen for the baseline configuration is the N+3 mission trajectory described in Bradley and Droney.<sup>19</sup> The mission profile is shown in Figure 58. ACS allows for the aircraft to be designed for a specific mission. The different phases of the N+3 mission were included in the input file for ACS for a design mission range of 3500 nm. A snapshot of the mission designed in ACS is shown in Figure 59. Details such as the taxi out time, taxi/warm-up power setting, takeoff power setting, total internal fuel, and phases of flight allocated as reserve were also fixed and based on known values from Bradley and Droney.<sup>19</sup>

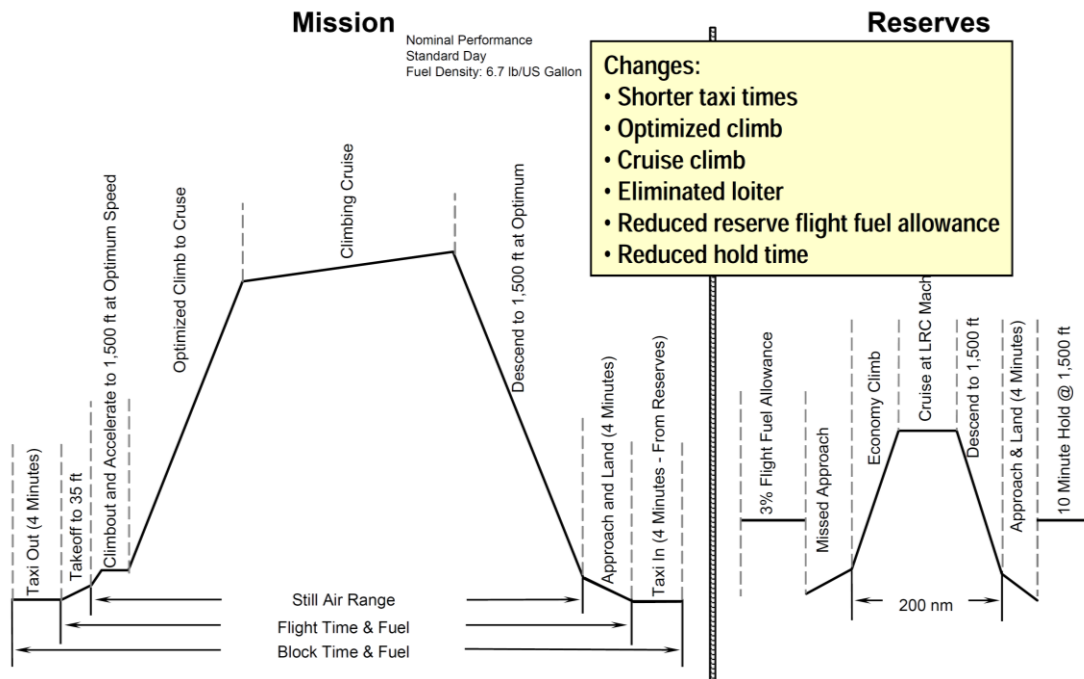


Figure 58: SUGAR N+3 mission trajectory.<sup>19</sup>

PHASE	MACH NO.		ALTITUDE		HORIZONTAL		NO. TURN	VIND "G'S	WKFUEL	M	IP	IX	W	B	A	P
	START	END	START	END	DIST	TIME										
CLIMB	0.00	-1	0	1500	-1.0	0.0	0.0	0.0	2.7000	1	2	-1	0	0	0	0
CLIMB	-1	0.70	1500	36700	-1.0	0.0	0.0	0.0	3.0000	1	2	-1	0	0	0	0
CRUISE	0.70	0.70	-1	36700	3500.0	0.0	0.0	0.0	1.0000	1	4	0	0	0	0	0
CRUISE	0.50	0.50	15000	15000	200.0	0.0	0.0	0.0	1.0000	1	4	0	0	0	0	0
LOITER	0.50	0.50	-1	1500	0.0	10.0	0.0	0.0	1.0000	1	4	0	0	0	0	0

Figure 59: ACS mission profile input.

### 6.1.3 Aerodynamics

In order to model the effect of the propulsive wing section on the aircraft aerodynamics, there was a need to tie in the CFD predictions of the profile drag of the designed transonic natural laminar flow section into the ACS performance routine. Given that the ACS aerodynamic model is based on full aircraft aerodynamic derivatives, a method had

to be derived to reflect changes in the aerodynamic performance of the full SUGAR Refined wing, based on changes in profile drag. Since the airfoil drag polar featured a defined drag bucket and did not have a parabolic variation with lift coefficient, the change in the wing drag due to a change in the airfoil section could not be modeled based on a simple change in Oswald efficiency factor. However, in order to apply a change in the wing aerodynamic performance, based on a change in the airfoil section, the exact geometry of the wing used on the SUGAR Refined must first be known. Since the airfoil, twist and chord distribution of the wing of the SUGAR Refined aircraft is proprietary to Boeing, this information was determined based on a series of semi-empirical methods. Once the wing aerodynamic performance was determined, this was then combined with the fuselage and horizontal tail to obtain the full aircraft aerodynamic force and moment coefficients.

As a first order approximation, an average sectional  $C_d$  for the SUGAR Refined wing was determined for the mean aerodynamic chord using methods derived in Anderson,<sup>37</sup> Nicolai and Carichner,<sup>38</sup> and Phillips.<sup>39</sup> For the case of lift, in cruise, the  $C_L$  of an aircraft is based on the lift of the wing and horizontal tail (assuming no lift contribution from the fuselage),

$$C_{L_{a/c}} = C_{L_W} + \frac{S_{HT}}{S_W} C_{L_{HT}}$$

where the lift coefficient of the wing and tail are related to the geometric angle of attack ( $\alpha_{geo}$ ), zero-lift angle of attack ( $\alpha_{ol}$ ), incidence angles ( $i_W, i_{HT}$ ) and tail downwash angle ( $\varepsilon_d$ ) as shown in the following equations,

$$C_{L_W} = (\alpha_{geo} - \alpha_{olW} + i_W) C_{L_{W\alpha}}$$

$$C_{L_{HT}} = (\alpha_{geo} - \alpha_{olHT} + i_h - \varepsilon_d) C_{L_{HT\alpha}}$$

From the above equations,  $\alpha_{geo}$  is known to be fixed for the entire aircraft. Based on empirical data,  $\varepsilon_d$ ,  $C_{L_{W\alpha}}$  and  $C_{L_{HT\alpha}}$  could be calculated. As a result,  $\alpha_{ol}$ ,  $i_W$ , and  $i_{HT}$  were solved for iteratively in order to converge upon the aircraft aerodynamic performance coefficients documented in the ACS and SUGAR Report.

Similar to the lift calculation, the drag of the aircraft was calculated by,

$$C_{D_{ac}} = C_{D_W} + C_{D_{HT}} + C_{D_{rest}}$$

where  $C_{D_{rest}}$  is given by,

$$C_{D_{rest}} = C_{D_{f,body}} + C_{D_{f,VT}} + C_{D_{interference}} + C_{D_{wave}} + C_{D_{ext}}$$

The wing drag,  $C_{D_W}$  was calculated from the profile drag and induced drag of the wing,

$$C_{D_W} = C_{D_{Wprofile}} + C_{D_{Winduced}} = C_{D_{Wmin}} + k_W C_{L_W}^2 + \frac{C_{L_W}^2}{\pi e_W A R_W}$$

where,  $e_w$  is the span efficiency factor ( $e = \frac{1}{1+\delta}$ ) of the wing and  $k_W$  is the constant of proportionality giving the rate of increase of  $C_d$  with  $C_l^2$ . The term  $k_W$  is unknown and



was iteratively solved to converge upon the  $C_D$  values provided by ACS. The parasite drag buildup data from ACS was used in order to determine the zero-lift drag coefficient of the wing

$$C_{D_{Wmin}} = C_{D_{W0}}$$

The resulting comparison of the airfoil and wing lift and drag coefficients provided by ACS and the first-order approach is shown in Figure 60 for the SUGAR Refined aircraft.

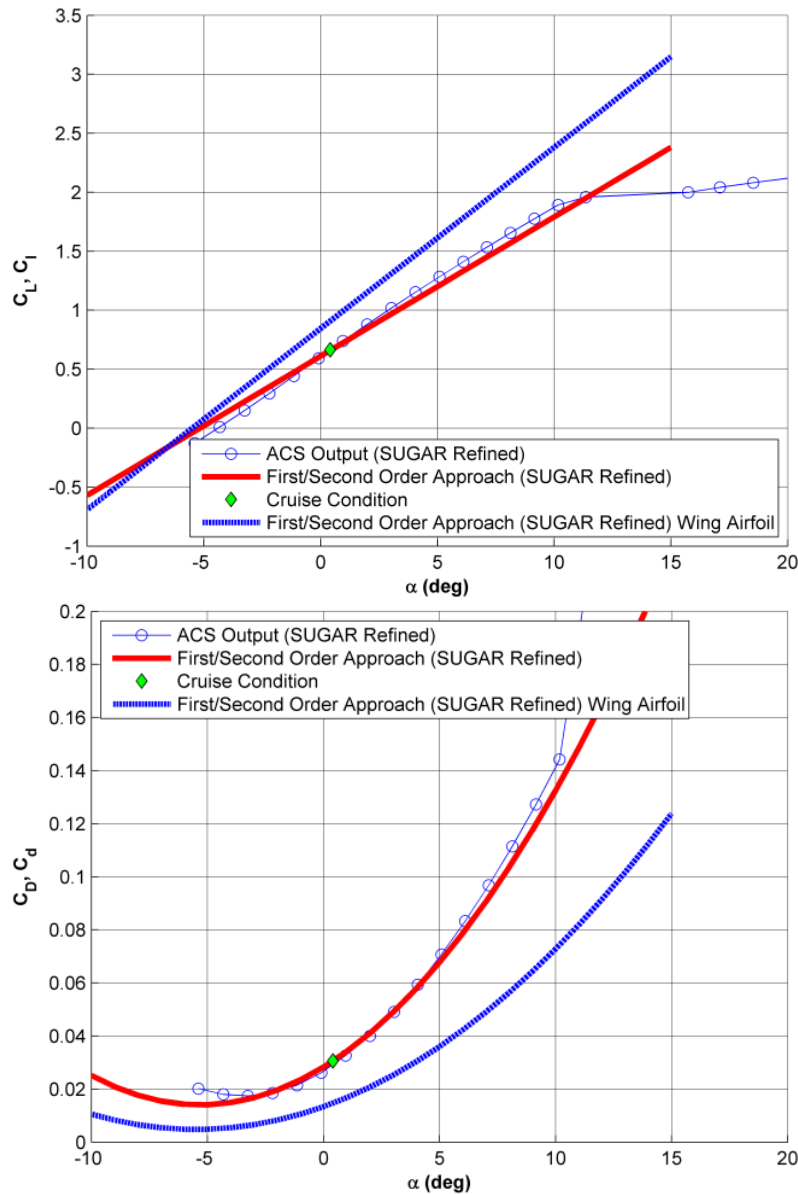


Figure 60: Plot showing matching of the First/Second Order approach with the SUGAR Refined results

### 6.1.4 Propulsion

The gFan++ Advanced Turbofan (JP+2045GT+DF) engine was conceptually designed by General Electric (GE) to be used on the N+4 SUGAR Refined. A conceptual layout of the engine is shown in Figure 61. The gFan++ is designed to be implemented in the 2035/45 timeframe. It is an iterative improvement from the CFM56-7B turbofan engine that is currently being used on the 737-800. Important parameters associated with the iterative designs of the gFan are tabulated in Table 8. Details of each engine iteration design can be found in Bradley and Droney<sup>19,20</sup>.

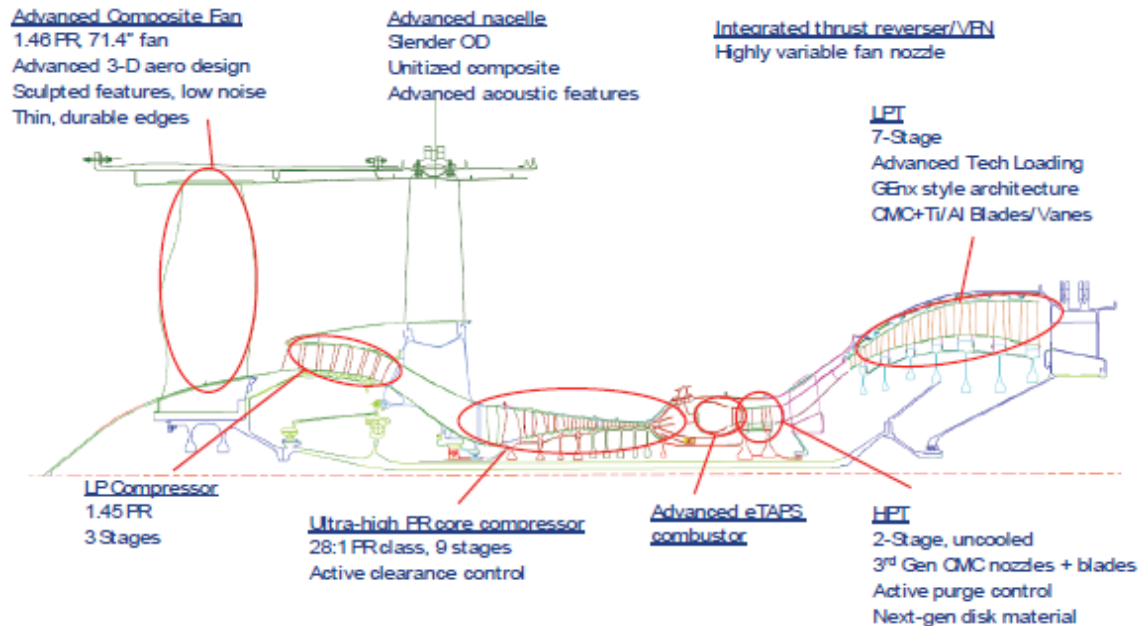


Figure 61: gFan++ advanced turbofan conceptual layout.<sup>20</sup>

Table 8: Comparison of SUGAR Configuration Turbofan Parameters.

Aircraft	Engine	Fan Dia. (in)	Length (in)	Thrust (SLS) (lbf)	SFC (dry) (lbm/lbf/hr)	Comp. OPR	Bypass Ratio
737-800/SUGAR Free	CFM56-7B	61	98.7	27,300	0.380	28.9	5.1
N+3 SUGAR Refined	gFan	70	122	18,900	0.256	66.0	9.2
N+3 SUGAR High	gFan+	77.3	122	18,800	0.211	59.0	13.0
N+4 SUGAR Refined	gFan++	71.4	127	21,943	0.214	59.0	<b>9.9</b>

### 6.1.5 Weights

Once the geometry, mission trajectory, aerodynamics, and propulsion systems were matched to known parameters, ACS was run for a design mission of 3,500 nm and a typical mission of 900 nm (no reserve). The automated result output returns values for

fuel burn and weights of the different components of the aircraft. Further tuning was then performed to variables related to the aircraft propulsion and aerodynamics to ensure that the fuel burn rates and individual component weights match that provided in Bradley and Droney<sup>20</sup>. Component weights were also individually adjusted to ensure that the ratio of empty weight to takeoff gross weight was accurate. The ACS output of the detailed weight breakdown of the designed N+4 SUGAR Refined is shown in Figure 62.

Component	Pounds	Kilograms	Percent
Airframe Structure	40266.	18265.	29.45
Wing	13280.	6024.	9.71
Fuselage	14653.	6646.	10.72
Horizontal Tail ( Low)	1176.	533.	0.86
Vertical Tail	1485.	674.	1.09
Nacelles	4825.	2189.	3.53
Landing Gear	4847.	2198.	3.55
Propulsion	9749.	4422.	7.13
Engines ( 2)	9111.	4133.	6.66
Engine Accessories	1276.	579.	0.93
Bare Installed Engines	6380.	2894.	4.67
Fuel System	638.	289.	0.47
Fixed Equipment	20943.	9500.	15.32
Hyd & Pneumatic	837.	380.	0.61
Electrical	2334.	1059.	1.71
Avionics	1483.	673.	1.08
Instrumentation	966.	438.	0.71
De-ice & Air Cond	1745.	791.	1.28
Aux Power System	980.	445.	0.72
Furnish & Eqpt	9499.	4309.	6.95
Seats and Lavatories	4935.	2238.	3.61
Galley	1550.	703.	1.13
Misc Cockpit	152.	69.	0.11
Cabin Finishing	2088.	947.	1.53
Cabin Emergency Equip	541.	245.	0.40
Cargo Handling	234.	106.	0.17
Flight Controls	3099.	1406.	2.27
Empty Weight	70957.	32186.	51.90
Operating Items	4714.	2138.	3.45
Flight Crew ( 2)	340.	154.	0.25
Crew Baggage and Provisions	275.	125.	0.20
Flight Attendants ( 5)	650.	295.	0.48
Unusable Fuel and Oil	373.	169.	0.27
Passenger Service	3080.	1397.	2.25
Cargo Containers	0.	0.	0.00
Operating Weight Empty	75671.	34324.	55.35
Fuel	30244.	13719.	22.12
Payload	30800.	13971.	22.53
Passengers (154)	26180.	11875.	19.15
Baggage	4620.	2096.	3.38
Cargo	0.	0.	0.00
Calculated Weight	136717.	62015.	100.00

Figure 62: ACS output of detailed weight breakdown for matched N+4 SUGAR Refined

## 6.1.6 Matching Results

The final matched aircraft ACS output and 900 nm mission summaries are shown in Figure 63. To ensure the ACS designed aircraft matched the N+4 SUGAR Refined, key parameters such as TOGW, cruise  $C_L$  and  $C_D$ , and block fuel/seat were compared. These comparisons are tabulated in Table 9. Table 9 shows that the designed aircraft accurately matches the N+4 SUGAR Refined configuration. As a result, it was safe to proceed with this configuration state as the baseline aircraft for sensitivity studies.

SUMMARY --- ACS OUTPUT: BOEING SUGAR Refined TRANSPORT

GENERAL		FUSELAGE		WING		HTAIL	VTAIL
WG	138361.	LENGTH	124.8	AREA	1285.9	265.9	213.4
W/S	107.6	DIAMETER	13.2	WETTED AREA	2591.8	294.0	429.0
T/W	0.50	VOLUME	14426.3	SPAN	122.3	40.7	20.3
N(2) ULT	3.8	WETTED AREA	4672.8	L.E. SWEEP	18.4	34.4	38.7
CREW	2.	FINENESS RATIO	9.5	C/4 SWEEP	15.1	30.0	33.2
PASSENGERS	154.			ASPECT RATIO	11.64	6.24	1.94
				TAPER RATIO	0.16	0.20	0.27
				T/C ROOT	0.12	0.10	0.10
				T/C TIP	0.12	0.10	0.10
				ROOT CHORD	18.1	10.9	16.5
				TIP CHORD	2.9	2.2	4.5
				M.A. CHORD	12.4	7.5	11.6
				LOC. OF L.E.	55.3	107.0	105.7
ENGINE		WEIGHTS					
NUMBER	2.	W	WG				
LENGTH	10.6	STRUCT.	41643. 30.1				
DIAM.	8.3	PROPUL.	9749. 7.0				
WEIGHT	3190.0	FIX. EQ.	20967. 15.2				
TSLs	34588.	FUEL	28028. 20.4				
SFCs	0.18	PAYLOAD	30800. 22.3				
ESF	1.000	OPER IT	7173. 5.2				

MISSION SUMMARY

PHASE	MACH	ALT	FUEL	TIME	DIST	L/D	THRUST	SFC	Q
TAKEOFF	0.00	0.	33.	4.0	1884.5				
CLIMB	0.49	1500.	77.	0.1	0.7	8.97	41214.9	0.310	342.0
CLIMB	0.70	36700.	1995.	4.9	30.8	19.33	12704.5	0.396	157.9
CRUISE	0.70	37559.	4421.	129.8	868.5	19.94	4034.2	0.499	151.6
DESCENT	0.27	0.	0.	41.6	165.2	23.31	0.0	0.000	111.0
LOITER	0.50	0.	0.	0.0	0.0	9.85	8067.2	0.556	370.3
LANDING					2189.9				

Block Time = 2.314 hr  
Block Range = 900.0 nm  
Block Fuel = 6527. lb

Figure 63: ACS output and 900 nm mission summaries

Table 9: Key Parameter Comparison (N+4 SUGAR Refined versus ACS matched).

Parameter	N+4 SUGAR Refined	ACS Matched	% Difference
TOGW	136,412	138,361	<2
Cruise $C_L$	0.675	0.665	<2
Cruise $C_D$	0.02975	0.0292	<2
Block Fuel / Seat (900 nm)	42.53	42.38	<1

## 6.1 Trade Studies / Sensitivity Analysis

The block fuel/seat for a typical 900 nm mission was used in the SUGAR studies as the basis for comparison between different SUGAR configurations. For the current study, this parameter was also used as the basis for sensitivity studies. Three independent variables in ACS were chosen to be varied in the systems analysis trade studies from the aerodynamics, propulsion, and structure/weights subsystems of the aircraft.

For the aerodynamics, the intended effect of implementing the Griffith/Goldschmied section was to reduce the zero-lift drag coefficient ( $C_{D0}$ ) of the aircraft. This reduction will therefore have a direct effect of reducing the block fuel/seat of the aircraft for the 900 nm mission. This effect was introduced in the ACS input file via a multiplicative factor on the  $C_{D0}$  of the aircraft, and a performance simulation of the modified aircraft was performed.

The implementation of the Griffith/Goldschmied section also required the use of boundary-layer suction to obtain the pressure recovery required. The proposed means of implementing this boundary-layer suction was via the use of crossflow fans. Similar to the other pneumatic, hydraulic, and electrical devices requiring power on the N+4 SUGAR Refined, the power required to run the crossflow fans is intended to be extracted from the integrated drive generators (IDG) of gFan++ engines. Current IDG's for Boeing 737-800 engines have a capacity of 90 kVA (per engine).<sup>40</sup> A plot of modeled power usage over a typical mission for the Boeing 737 is shown in Figure 64 from Williams et al.<sup>40</sup>

As can be deduced, the use of crossflow fans will require larger capacity or additional IDG's. As the SUGAR Reports mention, the SUGAR Refined would use the advanced generation 787 No-Bleed Electrical System Architecture. Based on the cross-flow fan experiments discussed in Section 5.2.1.1 and the required power for the SUGAR Refined, the total aircraft power required for the SUGAR Refined is 830.8 kVA (Hydraulics: 56.3 kVA, Electric: 540 kVA, Cross-flow Fan: 234.5 kVA after losses). These final power measures were implemented into the ACS tool in order to reflect the power extraction required by the aircraft configuration.



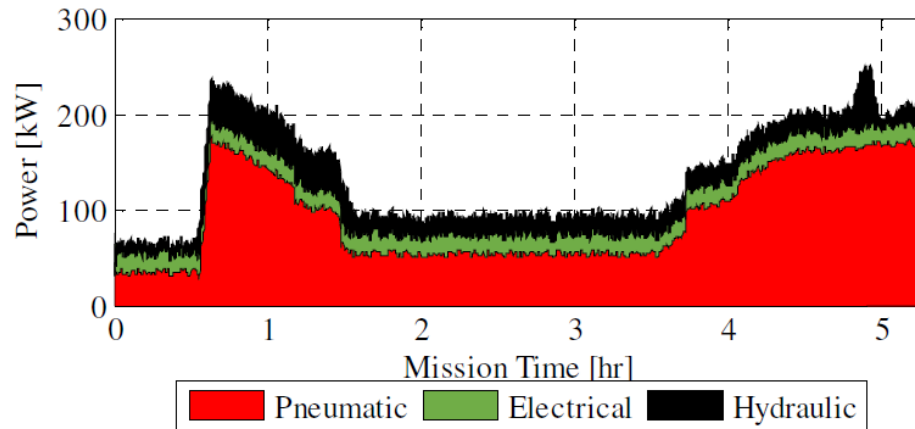


Figure 64: Instantaneous pneumatic, electrical, and hydraulic power over a mission profile for a sample Boeing 737 model.<sup>40</sup>

The final parameter variation was related to the weight of the wing due to the addition of crossflow fans into the system together with any associated structure for ducting. The addition of an extra IDG for running the crossflow fan system was also modeled through a change in the aircraft weight. Since the implementation for Griffith/Goldschmied section together with the cross-flow fans may allow for replacement of the aircraft high-lift system, the multielement flap and actuation mechanisms may be removed to produce reductions in wing weight. However, for a baseline analysis removal of the high lift system was not assumed in order to better understand the parametric sensitivity of the aircraft fuel burn on variations in all three parameters.

Using the three parameters mentioned (zero-lift drag coefficient, power extraction (kW), wing weight), carpet plots were created to observe the sensitivities associated with each variable for a typical 900 nm mission. The carpet plot is shown below in Figure 65.

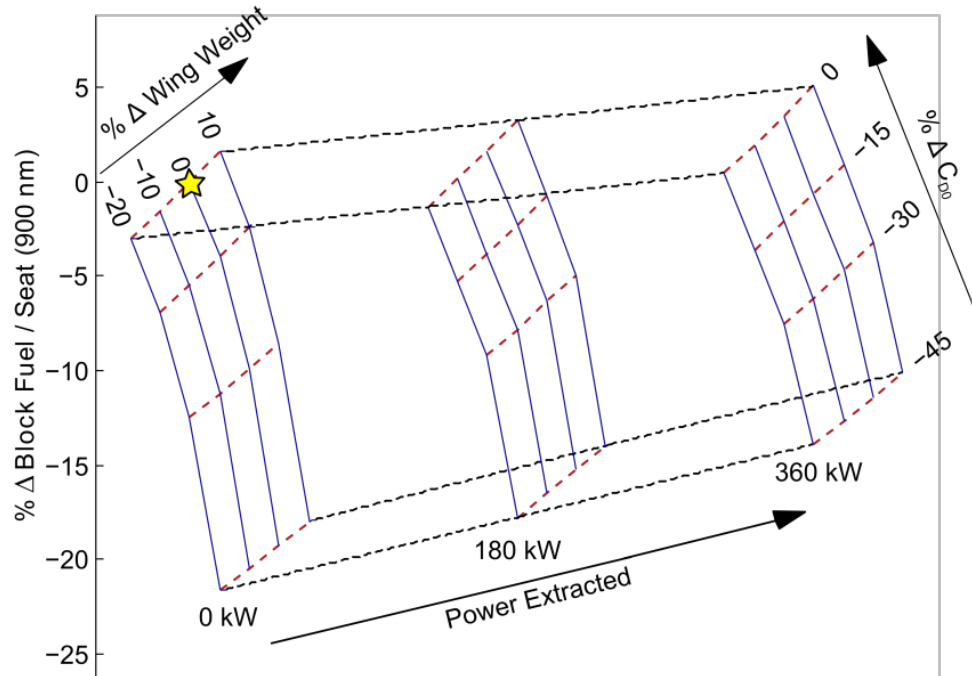


Figure 65: Carpet plot for the N+4 SUGAR Refined showing the effects of varying zero-lift drag coefficient, power extraction (kW), and wing weight on the block fuel / seat for a typical 900 nm mission.

Figure 65 shows three carpet plots (shown with blue and red lines) for three different levels of power extraction, 0 kW, 45 kW, and 90 kW. The red dashed lines represent % reduction in the zero-lift drag coefficient ( $\Delta C_{D0}$ ) from the baseline configuration. The blue lines represent the % change in the wing weight from the baseline weight.

What can be observed from the carpet plots is that the block fuel/seat is highly sensitive to both the zero-lift drag coefficient and the wing weight. It is the least sensitive to variations in power extraction. The power extraction values were chosen based on the current limits of power extraction from IDG's of the 737-800.<sup>40</sup> As more information regarding the power requirements from the crossflow fan wind tunnel tests were obtained, a clearer picture of the power requirements was modeled in a final systems and energy balance, discussed in Section 6.3. Similarly, the zero-lift drag coefficient was updated based on results from CFD and wind tunnel tests to determine its overall effect on the fuel burn.

## 6.2 Wing Structural Modeling

Given the sensitivity of the fuel burn to the wing weight, it was imperative to accurately model the effects of implementing the Griffith/Goldschmied concept on the structure and weight of the wing. The baseline wing configuration and Griffith/Goldschmied wing configuration (together with crossflow fans and associated ducting) were modeled. Modeling was carried out using a commercially available CAD package, SolidWorks, and the weight and structural properties of the wing were matched to data available in

Bradley and Droney.<sup>19,20</sup> A low order estimate of the wing weight effects due to the concept implementation was predicted. Figure 66 shows the buildup of the CAD model for the N+4 SUGAR Refined configuration containing the skin, spars, ribs, and stringers.

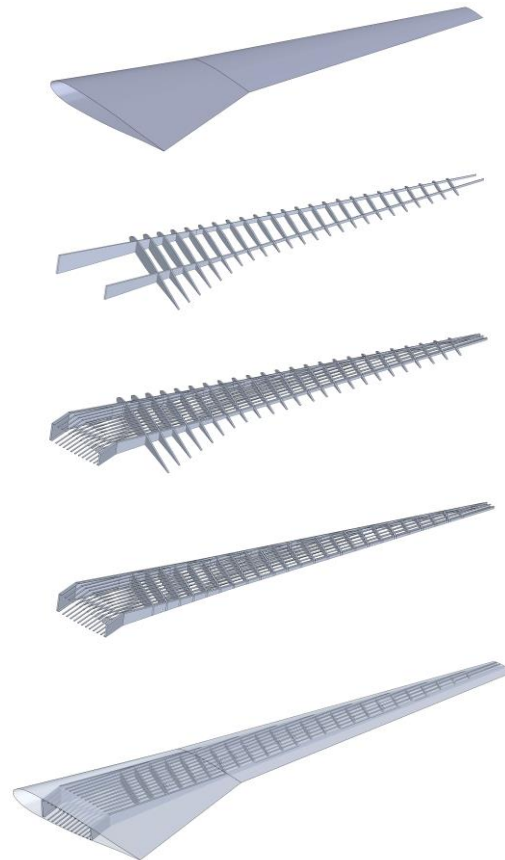


*Figure 66: CAD Model of N+4 SUGAR Refined wing structural model.*

### 6.3 Energy Balance Summary

From the implementation of the aerodynamics, propulsion and weights modeling, with the lower bound weights and a take-off gross weight of 131,722 lb, the block fuel / seat for a 900 nm mission was obtained from ACS to be 37.28 lb. **This represented a 11.8% reduction in fuel consumption from the baseline Boeing SUGAR Refined aircraft.** Even with a more conservative estimate for weights, where an additional 10% increase in wing weight was added, the result was a **11.4 % reduction in fuel consumption from the baseline case.**

## 7 Phase I Summary

Results from the Phase I investigation were very encouraging. An ultra-low drag transonic airfoil section was designed, using a suction-based pressure recovery system which enabled extended runs of laminar flow, pressure thrust, and wake filling. A

subsonic experiment of the airfoil design was conducted, which provided an excellent degree of validation of the suction system modeling and transition prediction of the OVERFLOW simulations. Experiments performed on the cross-flow fan displayed that such a system can be used for the desired suction-based pressure recovery on the airfoil in a transonic flow. A systems-level analysis also displayed that the decrease in drag produced by the airfoil section far outweighs the electrical power required to drive the suction system, leading to a net reduction in block fuel of approximately 12%, compared to the baseline fuel consumption of the Boeing SUGAR Refined aircraft configuration.

## 8 **References**

<sup>1</sup> Felder, J. L., Tong, M. T., Chu, J., “Sensitivity of Mission Energy Consumption to Turboelectric Distributed Propulsion Design Assumptions on the N3-X Hybrid Wing Body Aircraft,” AIAA 2012-3701, paper presented at the 48<sup>th</sup> AIAA/ASME/SAE/ASEE Joint Propulsion Conference and Exhibit, 30 July – 01 August, 2012, Atlanta, Georgia.

<sup>2</sup> Felder, J. L., Brown, G. V., Kim, H. D., paper ISABE-2011-1340, 2011.

<sup>3</sup> Huerta, M.P., “FAA Aerospace Forecast, Fiscal Years 2012-2032,” U.S. Department of Transportation, Federal Aviation Administration.

<sup>4</sup> MIT Airline Data Project, 2011 data, <http://web.mit.edu/airlinedata/www/default.html>.

<sup>5</sup> <http://aviationweek.com/awin/boundary-layer-ingestion-key-mitnasa-d8-hopes>

<sup>6</sup> Drela, M., *Simultaneous Optimization of the Airframe, Powerplant, and Operation of Transport Aircraft*, Department of Aeronautics and Astronautics, Massachusetts Institute of Technology, Cambridge, MA, 2010

<sup>7</sup> [http://www.nasa.gov/content/hybrid-wing-body-goes-hybrid/#.U96an2M0B\\_5](http://www.nasa.gov/content/hybrid-wing-body-goes-hybrid/#.U96an2M0B_5)

<sup>8</sup> [http://www.nasa.gov/content/the-double-bubble-d8-0/#.U96a5mM0B\\_6](http://www.nasa.gov/content/the-double-bubble-d8-0/#.U96a5mM0B_6)

<sup>9</sup> McMasters, J.H., Paisley, D.J., Hubert, R.J., Kroo, I., Bofah, K.K., Sullivan, J.P., Drela, M., “Advanced Configurations for Very Large Subsonic Transport Airplanes,” NASA-CR-198351, 1996.

<sup>10</sup> Yaros, S.F., Sexstone, M.G., Huebner, L.D., Lamar, J.E., McKinley, R.E., Torres, A.O., Burley, C.L., Scott, R.C., Small, W.J., “Synergistic Airframe-Propulsion Interactions and Integrations,” NASA-TM-1998-207644, 1998.

<sup>11</sup> Abu-Ghannam, B.J. and Shaw, R., “Natural Transition of Boundary Layers – The Effects of Turbulence, Pressure Gradient, and Flow History,” *Journal of Mechanical Engineering Science*, Vol. 22, No. 5, pp. 213-228, 1980.

<sup>12</sup> Richards, E. J., Walker W. S. and Greening J. R., “Tests of a Griffith Aerofoil in the 13 ft × 9 ft Wind Tunnel Part 1, Part 2, Part 3, Part 4, Lift, Drag, Pitching Moments and Velocity Distributions,” ARC/R&M-2148 ARC-7464 ARC-7561 ARC-8054 ARC-8055, 1944

<sup>13</sup> Goldschmied, F.R., “Fuselage Self-Propulsion by Static-Pressure Thrust: Wind-Tunnel Verification,” AIAA Paper 87-2935, 1987.

<sup>14</sup> Goldschmied, F.R., “Airfoil Static-Pressure Thrust: Flight Test Verification,” AIAA Paper 90-3286, 1990.

<sup>15</sup> Goldschmied, F.R., “Thick-Wing Spanloader All-Freighter: Design Concept for Tomorrow’s Air Cargo,” AIAA Paper 90-3198, 1990.

<sup>16</sup> Hancock, J.P., “Test of a High Efficiency Transverse Fan,” AIAA Paper 80-1243, 1980.

<sup>17</sup> Kummer, J. D., Dang, T. Q., “High-Lift Propulsive Airfoil with Integrated Cross-Flow Fan,”  
AIAA Journal of Aircraft, vol. 43, no. 4, August 2006.

<sup>18</sup> <http://www.propulsivewing.com> (under FLIGHT TESTS, you will see 2 different flying models)

<sup>19</sup> Bradley, M., and Droney, C., “Subsonic Ultra Green Aircraft Research: Phase I Final Report,” NASA/CR–2011-216847, April 2011.

<sup>20</sup> Bradley, M., and Droney, C., “Subsonic Ultra Green Aircraft Research: Phase II: N+4 Advanced Concept Development,” NASA/CR-2012-217556, May 2012.

<sup>21</sup> Jespersen, D., Pulliam T., Buning, P., “Recent Enhancement of OVERFLOW,” AIAA Paper 97-0644, 1997.

<sup>22</sup> Langel, C., M., Chow, R., Van Dam, C. P., Rumsey, M, A., Maniaci, D, C., Erhmann, R., S., and White, E. B., “A Computational Approach to Simulating the Effects of Realistic Surface Roughness on Boundary Layer Transition, AIAA Paper # 2014-0234, Presented at the 52<sup>nd</sup> Aerospace Sciences Meeting, National Harbor, Maryland, Jan. 13<sup>th</sup>, 2014.

<sup>23</sup> Langtry, R., and Menter, F., “Transition Modeling for General CFD Applications in Aeronautics,” AIAA Paper 2005-522, 2005.

<sup>24</sup> <http://openmdao.org/>



- <sup>25</sup> Painchaud-Ouellet, P., Tribes, C., Trépanier, J., and Pelletier, D., “Airfoil Shape Optimization Using a Nonuniform Rational B-Splines Parameterization Under Thickness Constraint, *AIAA Journal*, Vol. 44, No. 10, October 2006, pp. 2170 – 2178.
- <sup>26</sup> Lane, K., and Marshall, D., “A Surface Parameterization Method for Airfoil Optimization and High Lift 2D Geometries Utilizing the CST Methodology,” AIAA Paper # 2009-1461, presented at the 47th AIAA Aerospace Sciences Meeting Including The New Horizons Forum and Aerospace Exposition, 5 - 8 January 2009, Orlando, Florida.
- <sup>27</sup> Venkataraman, P., “A new procedure for Airfoil Definition,” AIAA Paper # 95-1875-CP.
- <sup>28</sup> H. Sobieczky, “Parametric Airfoils and Wings,” in: Notes on Numerical Fluid Mechanics, pp.71-88, Vieweg, 1998.
- <sup>29</sup> Masters, D., Taylor, N., Rendall, T., Allen, C., and Poole, D., “Review of Aerofoil Parameterisation Methods for Aerodynamic Shape Optimization,” AIAA Paper # 2015-0761, presented at the 53rd AIAA Aerospace Sciences Meeting, 5-9 January 2015, Kissimmee, Florida.
- <sup>30</sup> Glauret, M., Walker, W., Raymer, W., and Gregory, N., “Wind...Tunnel Tests on a Thick Suction Aerofoil with a Single Slot,” ARC R & M No. 2646, Oct. 1948.
- <sup>31</sup> <http://web.mit.edu/drela/Public/web/xfoil/>
- <sup>32</sup> Liebeck, R., H., “On the design of subsonic airfoils for high lift,” Douglas Paper 6463, McDonnell Douglas Corp., July 1976.
- <sup>33</sup> <http://www.profoil.org/>
- <sup>34</sup> Dygert, R.K. and Dang, T.Q., “Experimental Investigation of Embedded Cross-Flow Fan for Airfoil Propulsion/Circulation Control,” AIAA Paper 2007-368, 2007.
- <sup>35</sup> AVID, “ACS™ User’s Guide, Version 4.5.3,” March 2015.
- <sup>36</sup> Cassidy, P. F., Gatzke, T. D., Vaporean, C. N., “Integrating Synthesis and Simulation for Conceptual Design,” AIAA Paper 2008-1443, Jan 2008.
- <sup>37</sup> Anderson, J.D., *Fundamentals of Aerodynamics*, Fourth Edition, Maryland: McGraw Hill, 2005
- <sup>38</sup> Nicolai, L.M. and Carichner, G.E., *Fundamentals of Aircraft and Airship Design: Volume I - Aircraft Design*, Reston, VA: American Institute of Aeronautics and Astronautics, Inc., 2010.

<sup>39</sup> Phillips, W.F., *Mechanics of Flight*, Hoboken, New Jersey: John Wiley & Sons Inc., 2004.

<sup>40</sup> Williams, M., Sridharan, S., Banerjee, S., Mak, C. et al., "PowerFlow: A Toolbox for Modeling and Simulation of Aircraft Systems," SAE Technical Paper 2015-01-2417, 2015, doi:10.4271/2015-01-2417.

REPORT DOCUMENTATION PAGE			Form OMB No. 0704-0188	Approved
Public reporting burden for this collection of information is estimated to average 1 hour per response, including the time for reviewing instructions, searching existing data sources, gathering and maintaining the data needed, and completing and reviewing the collection of information. Send comments regarding this burden estimate or any other aspect of this collection of information, including suggestions for reducing this burden, to Washington Headquarters Services, Directorate for Information Operations and Reports, 1215 Jefferson Davis Highway, Suite 1204, Arlington, VA 22202-4302, and to the Office of Management and Budget, Paperwork Reduction Project (0704-0188), Washington, DC 20503.				
1. AGENCY USE ONLY (Leave Blank)	2. REPORT DATE June 30th, 2016	3. REPORT TYPE AND DATES COVERED Phase I LEARN Final Report		
4. TITLE AND SUBTITLE  LEARN Phase I Final Report: Design, Analysis and Evaluation of a Novel Propulsive Wing Concept		5. FUNDING NUMBERS  NNX15AE39A		
6. AUTHOR(S)  Brian R. Kramer, Phillip J. Ansell, Gavin Ananda, Aaron Perry, Michael F. Kerho				
7. PERFORMING ORGANIZATION NAME(S) AND ADDRESS(ES)  Rolling Hills Research Corporation 420 N. Nash Street El Segundo, CA 90245-2822		8. PERFORMING ORGANIZATION REPORT NUMBER  TR16-007		
9. SPONSORING/MONITORING AGENCY NAME(S) AND ADDRESS(ES)  NASA Dryden flight Research Center COTR: Hyun Dae Kim PO Box 273 Edwards, CA 93523-0273		10. SPONSORING/MENTORING AGENCY REPORT NUMBER		
11. SUPPLEMENTARY NOTES				
12a. DISTRIBUTION/AVAILABILITY STATEMENT  FAR 52.227-20 Rights in Data -- SBIR Program		12b. DISTRIBUTION CODE		
13. ABSTRACT (Maximum 200 words)  This report documents research performed under the Phase I LEARN project for the development of a novel propulsive wing concept using a transonic Griffith/Goldschmied section.				
14. SUBJECT TERMS  Optimization, flow control, systems energy balance, experimental testing, crossflow fan, suction system			15. NUMBER OF PAGES  79	
			16. PRICE CODE	
17. SECURITY CLASSIFICATION OF REPORT Unclassified	18. SECURITY CLASSIFICATION OF THIS PAGE Unclassified	19. SECURITY CLASSIFICATION OF ABSTRACT Unclassified	20. LIMITATION OF ABSTRACT Unlimited	